Geochemistry Geophysics Geosystems G3
AN ELECTRONIC JOURNAL OF THE EARTH SCIENCES
Published by AGU and the Geochemical Society

Article
Volume 7, Number 11
10 November 2006
Q11007, doi:10.1029/2006GC001248
ISSN: 1525-2027

A catalogue of deep mantle plumes: New results from finite-frequency tomography

R. Montelli
Department of Geosciences, Princeton University, Guyot Hall, Princeton, New Jersey 08544, USA

Now at ExxonMobil Upstream Research Company, P.O. Box 2189, GW03-940A, Houston, Texas 77252-2189, USA (montelli@princeton.edu)

G. Nolet and F. A. Dahlen
Department of Geosciences, Princeton University, Guyot Hall, Princeton, New Jersey 08544, USA

G. Masters
Institute of Geophysics and Planetary Physics, University of California San Diego, MS 0225, 9500 Gilman Drive, La Jolla, California 92093-0225, USA

[1] New finite-frequency tomographic images of *S*-wave velocity confirm the existence of deep mantle plumes below a large number of known hot spots. We compare *S*-anomaly images with an updated *P*-anomaly model. Deep mantle plumes are present beneath Ascension, Azores, Canary, Cape Verde, Cook Island, Crozet, Easter, Kerguelen, Hawaii, Samoa, and Tahiti. Afar, Atlantic Ridge, Bouvet(Shona), Cocos/Keeling, Louisville, and Reunion are shown to originate at least below the upper mantle if not much deeper. Plumes that reach only to midmantle are present beneath Bowie, Hainan, Eastern Australia, and Juan Fernandez; these plumes may have tails too thin to observe in the lowermost mantle, but the images are also consistent with an interpretation as "dying plumes" that have exhausted their source region. In the tomographic images, only the Eifel and Seychelles plumes are unambiguously confined to the upper mantle. Starting plumes are visible in the lowermost mantle beneath South of Java, East of Solomon, and in the Coral Sea. All imaged plumes are wide and fail to show plumeheads, suggesting a very weakly temperature-dependent viscosity for lower mantle minerals, and/or compositional variations. The *S*-wave velocity images show several minor differences with respect to the earlier *P*-wave results, including plume conduits that extend down to the core-mantle boundary beneath Cape Verde, Cook Island, and Kerguelen. A more substantial disagreement between *P*-wave and *S*-wave images reopens the question on the depth extent of the Iceland plume. We suggest that a pulsating behavior of the plume may explain the shape of the conduit beneath Iceland.

Components: 15,360 words, 44 figures, 1 table.

Keywords: Frechet derivatives; global seismology; mantle plumes; P waves; S waves; tomography.

Index Terms: 7208 Seismology: Mantle (1212, 1213, 8124); 7203 Seismology: Body waves; 7270 Seismology: Tomography (6982, 8180).

Received 16 January 2006; **Revised** 22 May 2006; **Accepted** 25 August 2006; **Published** 10 November 2006.

Montelli, R., G. Nolet, F. A. Dahlen, and G. Masters (2006), A catalogue of deep mantle plumes: New results from finite-frequency tomography, *Geochem. Geophys. Geosyst.*, *7*, Q11007, doi:10.1029/2006GC001248.

1. Introduction

[2] The presence of linear volcanic chains, significant topographic swells, large igneous provinces and a distinct isotopic signature of oceanic island basalts have long suggested the existence of deep plumes in the mantle [*Morgan*, 1971]. Plumes are considered to be narrow thermal upwellings relatively fixed with respect to one another, although their positions are affected by large-scale circulation, the so-called "mantle wind" [*Christensen*, 1998; *Steinberger and O'Connell*, 1998]. Plumes are ubiquitous in numerical simulations of mantle convection [*Bunge et al.*, 1997; *Zhong et al.*, 2000; *Cserepes and Yuen*, 2000; *Farnetani*, 1997; *Farnetani and Samuel*, 2005] and have been directly observed in laboratory experiments [*Davaille*, 1999; *Davaille et al.*, 2003; *Jellinek and Manga*, 2002]; however, only recently have they begun to appear in seismic tomographic images of the lower mantle [*Bijwaard and Spakman*, 1999; *Goes et al.*, 1999; *Rhodes and Davies*, 2001; *Zhao*, 2001; *Montelli et al.*, 2004a, 2004b].

[3] *Montelli et al.* [2004a] used finite-frequency *P*-wave tomography [*Dahlen et al.*, 2000] to interpret arrival time data with two different dominant periods (1 and 20 s) and an adaptive, irregular model parameterization [*Montelli et al.*, 2004b]. The images from this model, hereafter referred to as *PRI-P04*, showed columnar low-velocity anomalies with diameters of several hundred kilometers that were interpreted as lower mantle plumes. In this paper, we apply the same tomographic technique to invert long period *S*, differential *SS-S* and *ScS-S* arrival times, with a dominant period of 20 s. We also compare the *S*-wave images with an updated version of model *PRI-P04* that incorporates improved crustal corrections and reduced standard errors for *P* delays reported by the International Seismological Centre (ISC). Details of the differences between *PRI-P04* and the new model *PRI-P05* are given in Appendix A. Because the precision of short-period *S*-wave arrival times reported by the ISC is considered to be much lower than that of *P*-waves, we refrained from using ISC *S*-wave traveltimes. The *S*-wave data thus lack the difference in extent of sensitivity that comes with different frequency content, and that greatly helped to constrain plume widths in the *P*-wave models.

[4] Finite-frequency tomography corrects to first order for the effects of diffraction, by taking into account the sensitivity of the travel time to structure away from the ray-theoretical path. The cross diameter of the Fresnel zone of significant off-path sensitivity is of the order of $\sqrt{\lambda L}$ for a wave of wavelength λ and ray length L. For data with the same dominant period, *S*-wave sensitivity regions are about 30% narrower than those for *P*-wave kernels, and their amplitudes are a factor of three larger, as shown in Figure 1. The narrower Fresnel zones and the higher sensitivity of *S* waves to temperature compensate partly for the absence of short-period data.

2. *S*-Wave Inversion and Resolution Tests

[5] We use the traveltimes of 69,195 *S*-waves, and the differential travel times of 27,043 *SS-S* and 13,856 *ScS-S* arrivals, with a dominant period of 20 s. Epicentral distances range between 23° and 99° for *S*-waves, 47° and 99° for *SS-S*, and 44° and 77° for *ScS-S* measurements, respectively. The traveltimes were measured by cross correlation with a synthetic pulse constructed by convolving the impulse response of the instrument at Albuquerque (ANMO) with a t* attenuation operator [*Bolton and Masters*, 2001]; the attenuation time t* is kept constant at 4 s for *S* waves. Predicted absolute and differential times were computed using the spherically symmetric velocity model *iasp91* [*Kennett and Engdahl*, 1991].

[6] Interactive software is used to handle triplications of *SS* and discriminate between *SKSac* and *ScS*, to ensure measurement of the correct *ScS* arrival time. We assigned standard deviations for each phase in three accuracy classes: 0.75–1.20 s, 1–1.71 s and 0.85–1.50 s for *S*, *SS-S* and *ScS-S*, respectively [*Montelli et al.*, 2004b]; about 1,500 outliers with deviations larger than $\pm 3\sigma$ after a first inversion were rejected for subsequent inversions.

[7] The matrix for the finite-frequency inversion is computed using dynamic ray tracing [*Dahlen et al.*, 2000]. The resulting "banana-doughnut" kernels depend on the frequency spectrum of the time signal. For consistency with the measurement procedure for the cross-correlated delay times, we use the ANMO station impulse response to compute the power spectra of the (non-attenuated) S pulse. We invert for both the fractional perturbation in the shear velocity $\delta v_S/v_S$ and the perturbation in the origin times and locations of the 7,033 earthquake hypocenters. We use the same linearly interpolated Delaunay mesh of tetrahedra to parameterize the model as *Montelli et al.* [2004a]. The grid contains

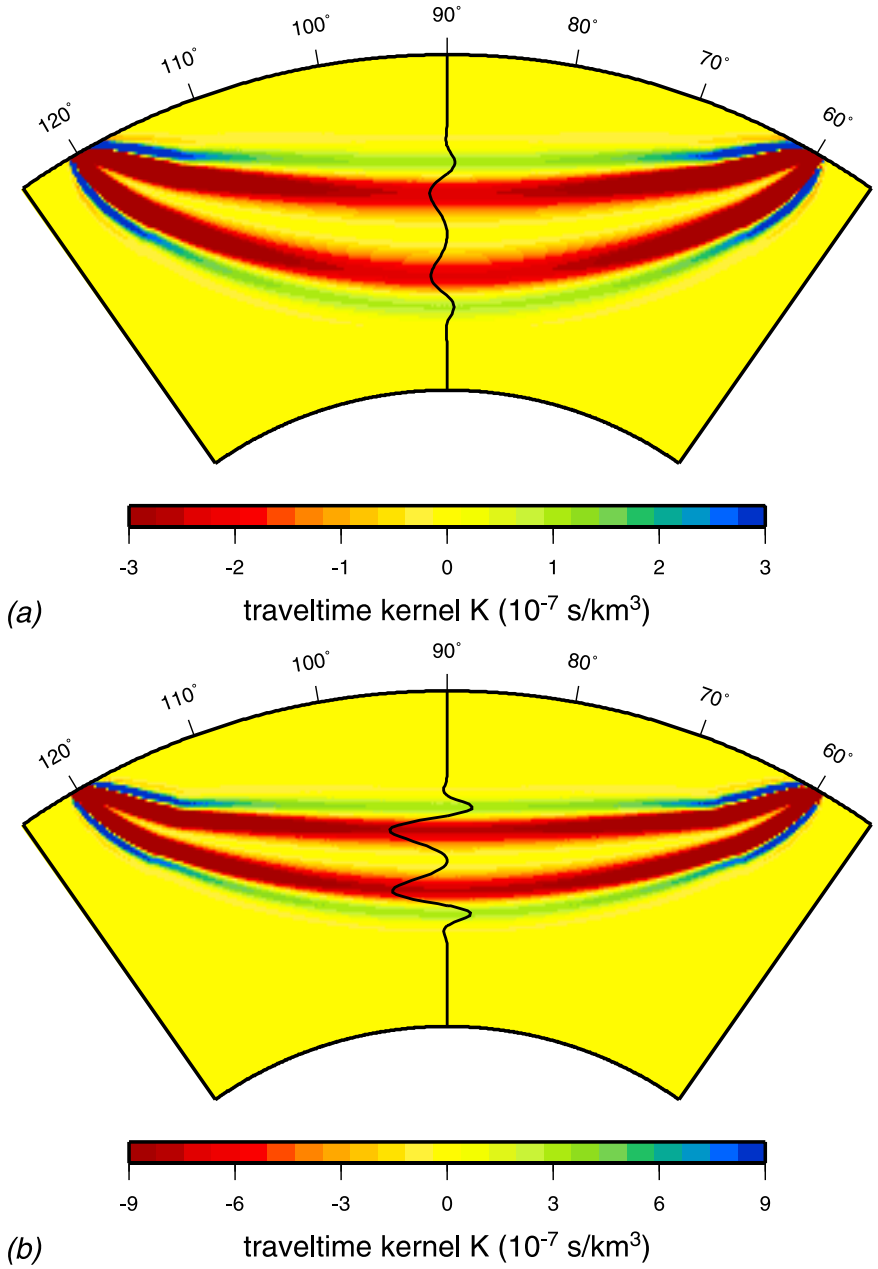

Figure 1. Cross sections of the Fréchet kernel for finite-frequency travel times of (a) a *P* wave and (b) an *S* wave at 60° epicentral distance with 20 s dominant period. Note the change of the color scale for the *S*-wave kernel. Solid lines show the variation of the sensitivity kernel with depth on a line through the turning point.

19,279 nodes whose distance increases with depth; 63% of these nodes are located in the upper mantle, 33.4% in the lower mantle, 3.3% in the core. The remaining 0.3% forms the convex hull, the surface that wraps the Delaunay mesh. Grid nodes within the core and the convex hull are necessary for the consistency of the Delaunay mesh. Figure 2 shows the average distance between two vertices for each tetrahedron forming the grid as a function of depth. Node distances range between 300–400 km in the upper mantle, 400–600 km in the midmantle, and 600–800 km in the lowermost mantle.

[8] Figure 3 shows the column density for the *S*, *SS*-*S* and *ScS*-*S* matrices, respectively, as a function of depth. We define the density for a given node of the grid as the sum of absolute values of the elements of the column that corresponds to that node. Because of the complex shape of the *SS* sensitivity kernels near the surface bounce points, the *SS*-*S* data provide a significant contribution to

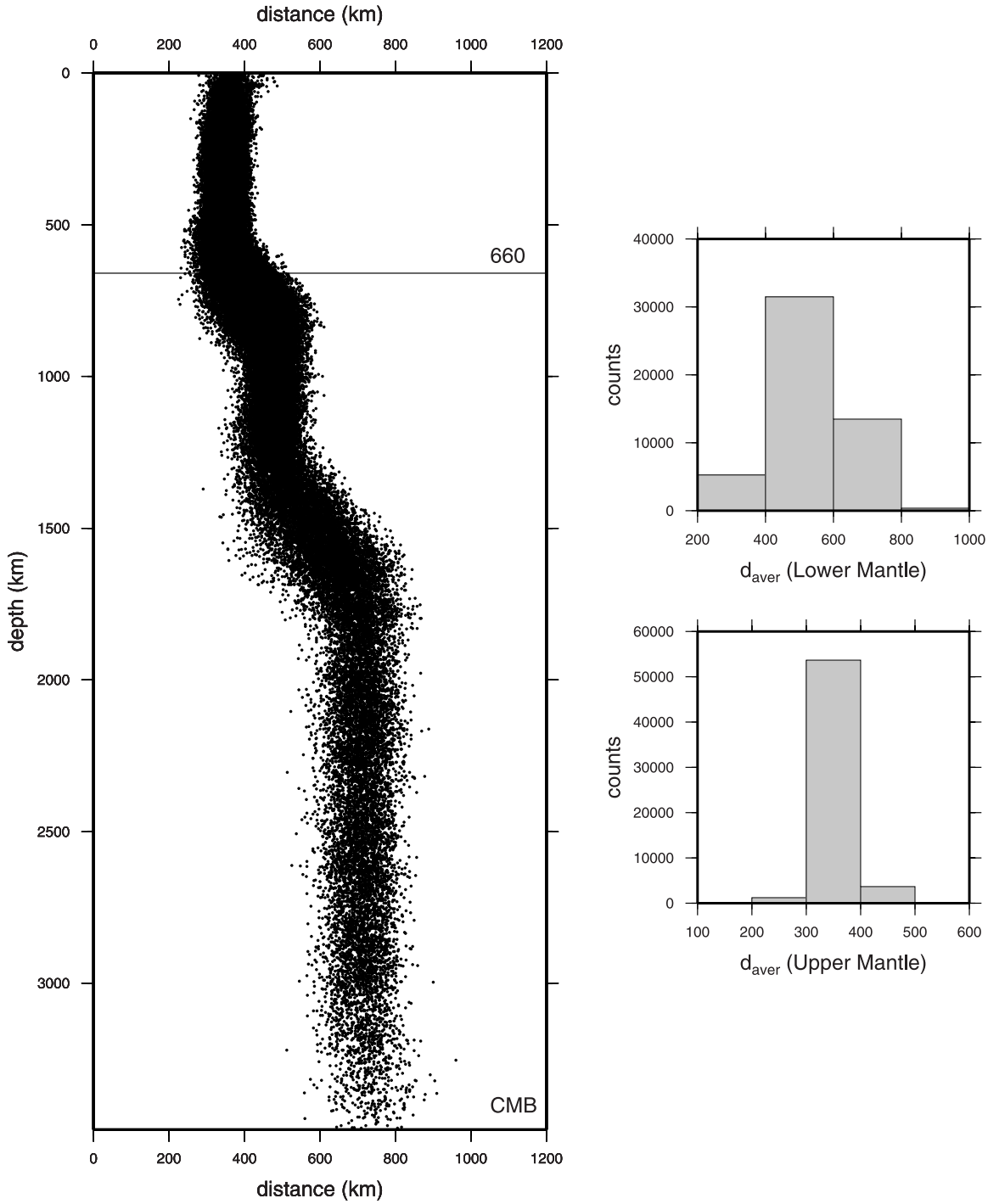

Figure 2. Average distance between vertex pairs of the tetrahedra forming the grid, as a function of depth of the midpoint. Histograms show average distance in the upper mantle (300–400 km) and in the lower mantle (400–600 km between 660 and 1500 km depth and 600–800 km below 1500 km depth).

constrain the upper mantle, as shown in Figure 3. Though relatively small in number, the *ScS-S* data provide additional constraints in the lowermost mantle.

[9] Resolution tests are useful to see how well the data coverage would image a hypothetical anomaly. To this end we replace the observed data with "synthetic" data generated for a known anomaly, designed to test for effects due to lack of resolution. Lack of resolution affects plume images in different ways, most importantly: (1) deep plume images may lack enough contrast to be visible at depth, and

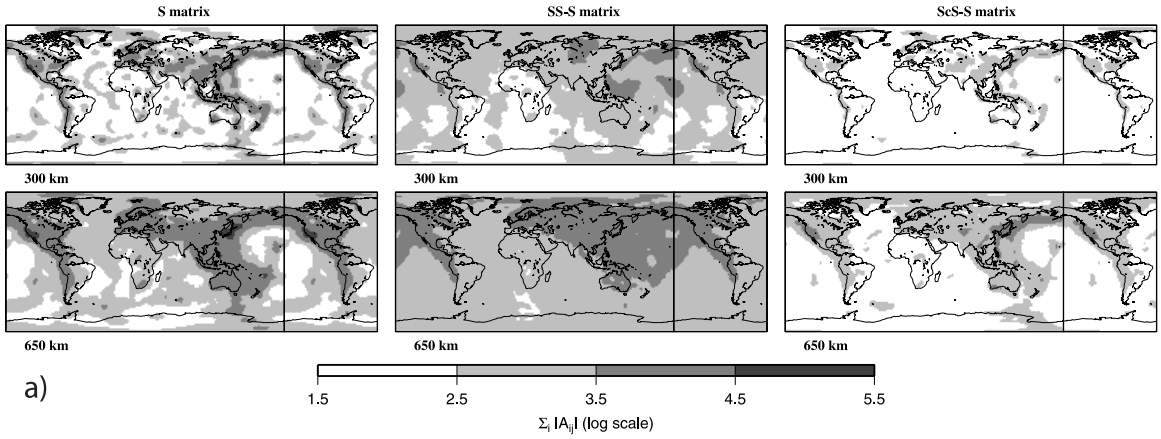

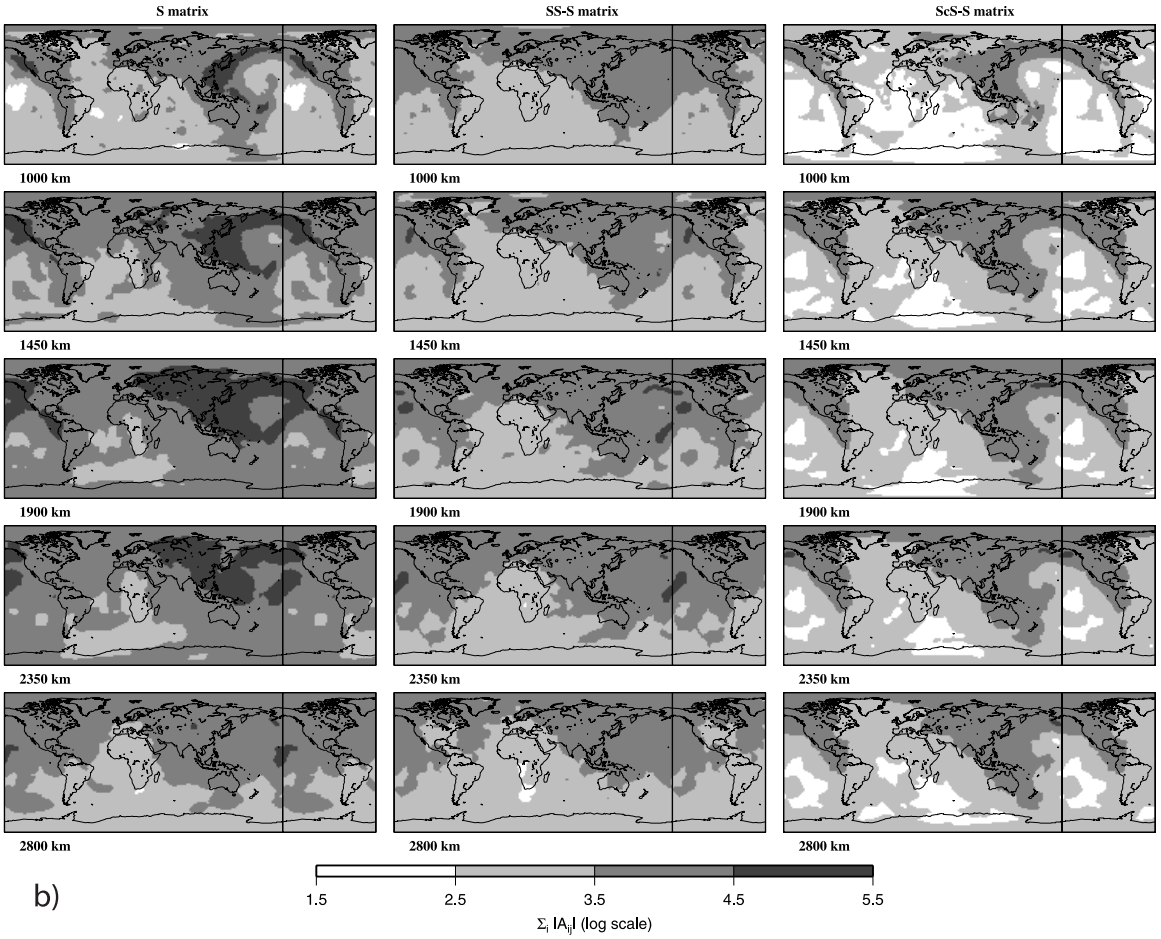

Figure 3. (a) Sections at 300 and 650 km depth of the density of the (left) *S*, (middle) *SS-S*, and (right) *ScS-S* matrix, respectively; expressed as the sum of the absolute values of the elements of each column of the matrix. Note that the maps have been "wrapped around" to aid in the visualization of patterns in the vicinity of the Greenwich meridian. (b) Map of the density matrices at five different depths (1000, 1450, 1900, 2350, and 2800 km) in the lower mantle.

(2) images of shallow anomalies may be stretched into the lower mantle ("vertical leakage"). For the *S* model presented in this paper, we generated a large number of synthetic data sets using finite-frequency sensitivity kernels for Earth models with cylindrical Gaussian anomalies $\delta v_S/v_S = (\delta v_S/v_S)_{max} \exp(-r^2/w^2)$. Separate tests were performed for plume radii w of 100, 200, 300

and 400 km, centered at a large number of observed plume locations, and vertical leakage was investigated for the synthetic plumes extending to different depth levels: 300, 650, 1900 and 2800 km. These synthetic plumes are sampled on a much finer grid than the grid used for the inversion, so that the tests also captures effects that are due to inadequacies of the parameterization. After adding random (Gaussian) noise with the same assigned standard deviations as in the actual data, these synthetic data were inverted using the same model parameterization and same regularization as in the actual inversion, and the images were inspected for agreement with the input image used to generate them. To adopt an objective standard, we designate a lower mantle plume as "resolved" if the recovered synthetic image has a contrast $|\delta v_S/v_S| > 0.5\%$. This somewhat arbitrary, but conservative, threshold corresponds to a temperature contrast of the order of 100 K in the lower mantle [*Karato*, 1993].

[10] We refrain from drawing any conclusion on the depth extent and/or geometry of anomalies in the upper mantle because the very shallow ray coverage is predominantly vertical and may influence the geometry of the imaged uppermost anomalies considerably. We have not yet incorporated surface waves in the finite-frequency inversion, which would allow us to improve resolution in the uppermost mantle. Synthetic tests for plumes extending down to 300 km depth show that there is no leakage of the reconstructed plumes into the lower mantle. We therefore display our images starting at a depth of 300 km.

[11] By using a range of synthetic plume radii, we are also able to determine the minimum radius that a plume must have to be resolved in the tomographic image. The results of these tests are summarized in Table 1. Following the coding used by *Montelli et al.* [2004a], depths are preceded by a $\geq$ sign if we conclude that the absence of a plume at greater depth may be due to a lack of resolution; or a $\leq$ sign if the image of the plume down to a certain depth might be generated by leakage to this depth; or a $\simeq$ if we have sufficient resolution (we do not use an equal sign to emphasize that the depths in Table 1 are only estimates). Even in the case of well-resolved plumes, the depths are uncertain to several hundred km.

[12] A number of individual images of sensitivity tests for *PRI-S05* are shown in section 4, where we discuss each plume separately. We did not redo resolution calculations for *P*. Since we lowered the estimated error in the ISC *P*-wave delays from 0.9 to 0.7 s (see Appendix A), the resolution calculated for *PRI-P04* by *Montelli et al.* [2004a] is a somewhat conservative estimate for the new model, which is acceptable for the purpose of the discussions in this paper.

3. *S*-Model Compared to Other Tomographic Models

[13] In this section we present global comparisons of the *S*-model (*PRI-S05*) with *PRI-P05* and several recent shear-wave velocity models: (1) *SAW24B16* [*Mégnin and Romanowicz*, 2000], (2) *S362D1* [*Gu et al.*, 2001] (both in Figures 4 and 5), (3) *S20RTS* [*Ritsema and van Heijst*, 2000] (Figures 4 and 6), (4) *S&G*, an early version of the model by *Simmons et al.* [2006] (Figures 4 and 6), and (5) *SB4L18* [*Masters et al.*, 2000] (Figures 4 and 7).

[14] With the exception of *S&G*, models were taken from the Reference Earth Model (REM) Web page at http://mahi.ucsd.edu/Gabi/rem.html. Models *SAW24B16*, *SB4L18*, *S362D1* and *S20RTS* were derived from surface-wave, free-oscillation and body wave data, and are expected to provide good resolution in the upper mantle. The long period shear-wave data included in the *SB4L18* model are a subset of the data we used to obtain *PRI-S05*. Model *S&G* has been obtained by inverting body wave travel times only and is the most recent in a sequence of such models produced by Grand and his group [*Grand et al.*, 1997; *Grand*, 2002]. This model uses almost twice the number of data used in earlier studies, and includes upgoing phases such as *sS*, *sScS*, etc. Figure 7 also shows the *P* velocity model *PRI-P05*, an update of the *P*-wave model published by *Montelli et al.* [2004a] (see Appendix A). All models plotted were regridded at 2° intervals.

[15] An eyeball comparison between these models shows good agreement for long wavelength structures. In all models the lowermost mantle is characterized by the two very large low-velocity regions or "superplumes" beneath Africa and the Pacific Ocean. Just above the core-mantle boundary, the African superplume extends from south Africa along the eastern Atlantic Ocean and extends to Kerguelen in the Indian Ocean in all models except *PRI-P05*. *SAW24B16* does not show an upward continuity for the Kerguelen extension like the other models do (including *PRI-P05*), and in *S20RTS* this extension is very weak. The African

Table 1. Summary of the Results for the 35 Hot Spots Present in Both *PRI-P05* and *PRI-S05*[a]

Label	Name[b]	Latitude and Longitude		Plate[c]	P-Wave Anomaly		S-Wave Anomaly	
					Depth,[d] km	Radius,[e] km	Depth,[d] km	Radius,[e] km
AF	**Afar** *(pd)*	**7°N**	**39°E**	**af**	**≥1450**	**200**	**≥1900**	**200**
AR	**Atlantic Ridge** ***(pd)***	**22°N**	**45°W**	**na**	**≃1900**	**200**	**≥1900**	**200**
AS	**Ascension** ***(d)***	**8°S**	**14°W**	**sa**	**≃2800**	**100**	**≃2800**	**100**
AZ	**Azores** ***(d)***	**38°N**	**26°W**	**eu**	**≃2800**	**300**	**≃2800**	**100**
BV	Bouvet (Shona) *(pd)*	54°S	3°E	af	≤1450	400	≥1900	300
BW	**Bowie** *(mm)*	**53°N**	**136°W**	**pa**	**≤650**	**100**	**≃1450**	**300**
CN	**Canary** *(d)*	**28°N**	**18°W**	**af**	**≃2800**	**400**	**≃2800**	**100**
CV	**CapeVerde** ***(d)***	**15°N**	**24°W**	**af**	**≥1900**	**300**	**≃2800**	**300**
CR	Caroline	3°N	167°E	pa	≥1000	300	—	—
CH	Chatam[f]	44°S	177°W	an	≃1450	—	—	—
CK	Cocos/Keeling *(pd)*	17°S	95°E	au	≤1000	200	≥1450	300
CI	**Cook Island** ***(d)***	**22°S**	**158°W**	**pa**	**≥1450**	**200**	**≃2800**	**300**
CS	**Coral Sea** ***(st)***	**15°S**	**155°E**	**au**	**upward to 2350**	**300**	**upward to 2350**	**300**
CZ	**Crozet** ***(d)***	**46°S**	**50°E**	**an**	**≃2350**	**400**	**≃2800**	**300**
ES	**Easter** *(d)*	**27°S**	**108°W**	**nz**	**≃2800**	**400**	**≃2800**	**200**
EA	Eastern Australia *(mm)*	41°S	146°E	au	≃650	100	≃1450	200
SL	**East of Solomon** ***(st)***	**5°S**	**165°E**	**pa**	**upward to 1000**		**upward to 1450**	**300**
EF	**Eifel** *(um)*	**50°N**	**4°E**	**eu**	**≃300**	**100**	**≤650**	**200**
ET	**Etna** *(um)*	**38°N**	**15°E**	**eu**	**≤—**	**200**	**≃650**	**200**
ER	Erebus[f]	78°S	167°E	an	1000		1000	
GL	Galapagos *(d)*	0°	92°W	nz	≤2350	300	≃2800	200
HN	**Hainan** *(mm)*	**20°N**	**110°E**	**eu**	**≃1900**	**200**	**≃1900**	**200**
HW	**Hawaii** *(pd)*	**19°N**	**155°W**	**pa**	**≥2800**	**300**	**≥1900**	**300**
IC	Iceland *(d)*	64°N	17°W	na	≤1900	100	≃2350	200
IO	**Indian Ocean**	**35°S**	**100°E**	**au**	**≥1900**	**400**	**≥1900**	**400**
JF	**Juan de Fuca/Cobb** ***(mm)***	**46°N**	**130°W**	**pa**	**≤1000**	**100**	**≃1000**	**200**
JZ	Juan Fernandez *(mm)*	34°S	81°W	nz	≥2350	300	≃1000	200
KG	**Kerguelen** ***(d)***	**50°S**	**69°E**	**an**	**≃2800**	**400**	**≃2800**	**200**
LV	Lake Victoria[f]	3°S	38°E	af	1000		1000	
LS	**Louisville** ***(pd)***	**54°S**	**141°W**	**pa**	**≥1450**	**300**	**≥1000**	**300**
RN	**Reunion** ***(pd)***	**21°S**	**56°E**	**af**	**≥1900**	**200**	**≥1450**	**200**
SM	**Samoa** *(d)*	**15°S**	**168°W**	**pa**	**≃2800**	**200**	**≃2800**	**300**
SJ	**South of Java** ***(st)***	**12°S**	**112°E**	**au**	**upward to 1450**	**300**	**upward to 1450**	**300**
SY	**Seychelles** ***(um)***	**5°S**	**56°E**	**af**	**≃1000**		**≃650**	**200**
TH	**Tahiti** ***(d)***	**18°S**	**148°W**	**pa**	**≃2800**	**300**	**≃2800**	**300**

[a] Depth limits and minimum radius (in the lower mantle unless the plume is confined to the upper mantle) have been determined from the resolution analysis. In bold are the plumes whose depth extent is in the same range for both the *P* and *S* anomalies.
[b] Name notes (in parentheses): d, deep plume; pd, potentially deep plume; mm, mid-mantle plume; um, upper mantle plume; st, starting plume.
[c] Plate notes: af, African plate; an, Antarctic plate; au, Autralian plate; eu, Eurasian plate; nz, Nazca plate; pa, Pacific plate; sa, South American plate.
[d] See text for explanation, including meaning of symbols ≥, ≤, and ≃.
[e] Minimum radius of the plume constrained from the resolution tests.
[f] Plumes for which resolution tests were not performed.

superplume rises to about 1500 km depth in all models, and even to 900 km depth in *SAW24B16*.

[16] The Pacific superplume is also present in all models. Though the models disagree on the detailed shape of this important feature near the core mantle boundary, most show it divided up into three main anomalies within a more general, low-velocity region. At 2800 km depth, the eye distinguishes broad maxima located beneath the Solomon Islands/Coral Sea, Samoa/Tahiti and Easter Island (Figures 5–7). Several models suggest the spawning of more discrete, plume-like upwellings, from the top of this superplume and *S20RTS*, *S&G* and the

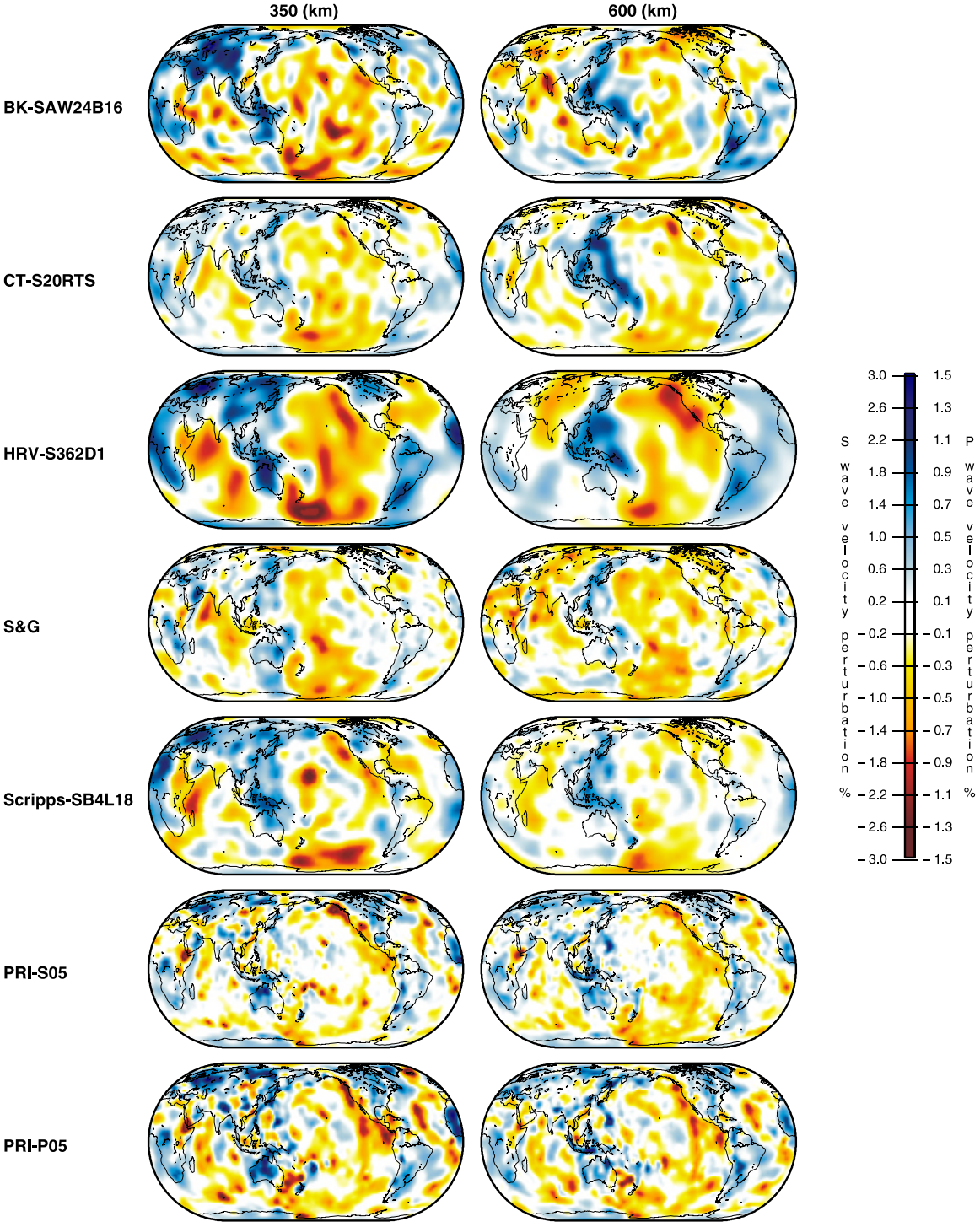

Figure 4. Cross sections at 350 km (left column) and 600 km (right column) depth of the shear velocity models (from top to bottom): Berkeley, *BK-SAW24B16*; Caltech, *CT-S20RTS*; Harvard, *HRV-S362D1*; Austin, *S&G*; Scripps, *SB4L18*; and Princeton, *PRI-S05*. In the bottom row we show our *P*-wave velocity model to allow direct comparison with our *S*-wave velocity model.

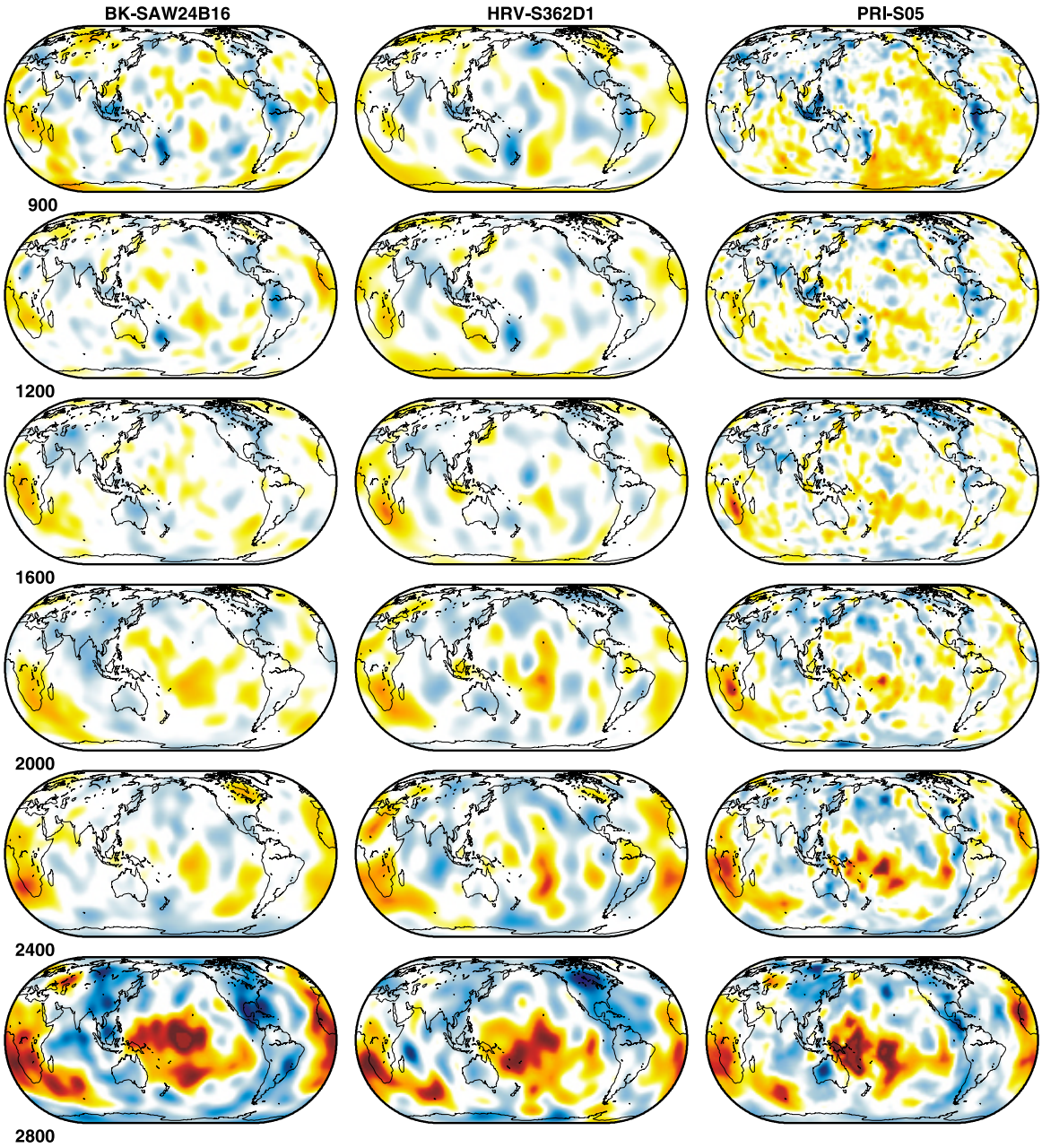

Figure 5. Cross sections at different depths (900, 1200, 1600, 2000, 2400, and 2800 km) in the lower mantle of the *S*-wave velocity models: Berkeley, *BK-SAW24B16*; Harvard, *HRV-S362D1*; and Princeton, *PRI-S05*. Color scale is the same as in Figure 4.

Princeton models roughly agree on their location in the lowermost 1000 km of the mantle, but clearly the discrepancy between the models increases as the plumes narrow.

[17] The differences that exist for shorter length scales are most evident when comparing *PRI-S05* with *PRI-P05* and *S&G*, the three models that allow for shorter wavelength structures. Only *PRI-S05* and *PRI-P05* show plume-like features in the upper mantle that are not only clearly delineated but also connected to low velocities in the lowermost mantle. A number of plumes that show continuity with depth in *PRI-S05* are also continuous in *S20RTS* and *S&G* and, to a lesser extent, *PRI-P05* and *S362D1* (e.g., Canary/Cape Verde, East of Solomon, Kerguelen, Tahiti). In the other models, low-velocity anomalies are often part of broader slow regions, especially in the Pacific in the upper mantle, and lack a sharp signature in the midmantle.

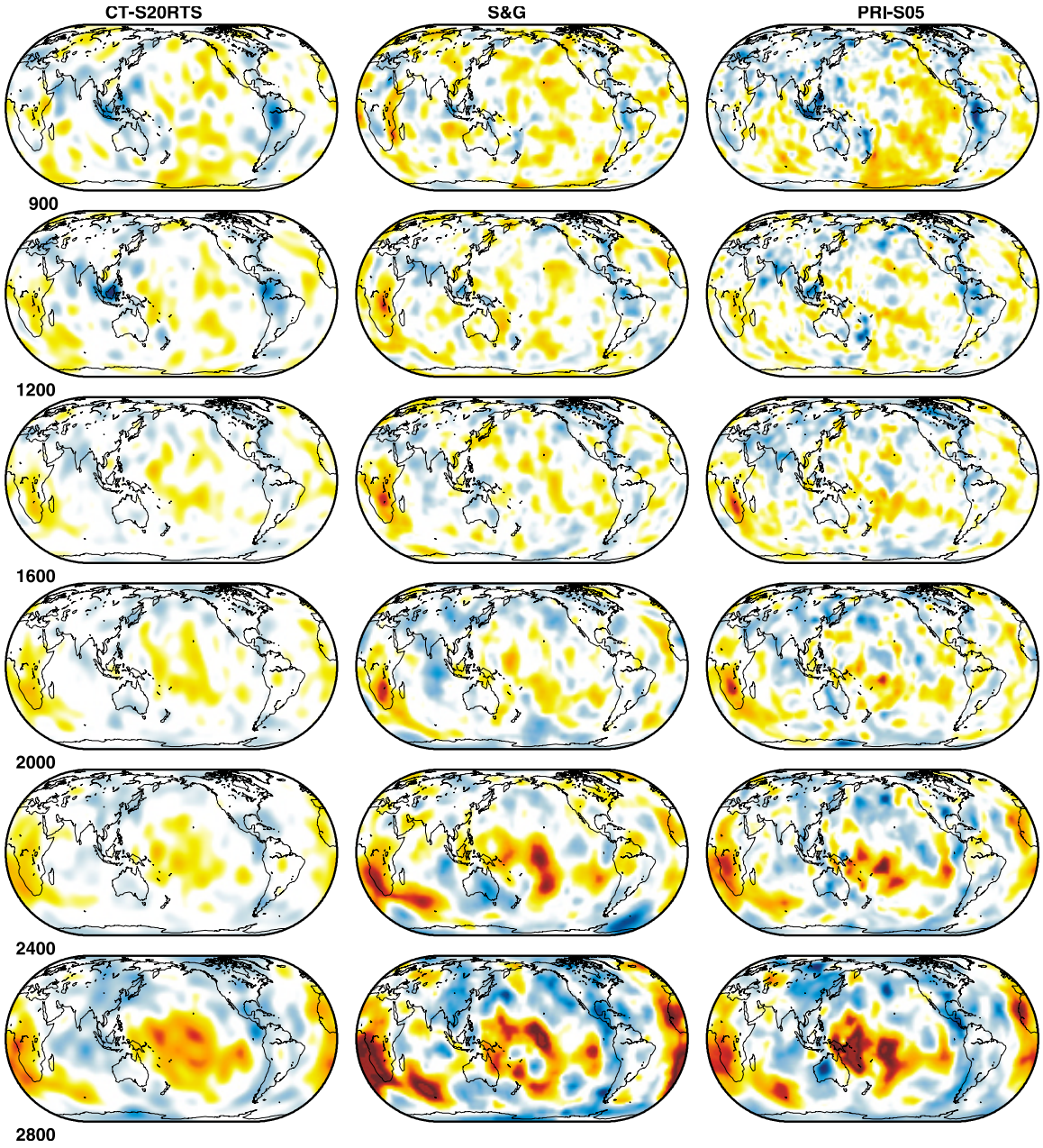

Figure 6. Cross sections at different depths (900, 1200, 1600, 2000, 2400, and 2800 km) in the lower mantle of the *S*-wave velocity models: Caltech, *CT-S20RTS*; Austin, *S&G*; and Princeton, *PRI-S05*. Color scale is the same as in Figures 4 and 5.

[18] Although this paper is mostly concerned with plume images, we note that all models agree equally well on the location of large-scale fast anomalies. For example, the circum-Pacific ring of fast material is visible in all models at 2800 km depth, though subdued in *PRI-P05* due to the exclusion of core-grazing phases in the data for that model. Below 670 km all models show the Farallon anomaly, even though this is a narrow feature that allows for differences in the image details, and they agree on the presence of a fast anomaly beneath southern Eurasia, identified as a remnant of the Tethys slab by *van der Voo et al.* [1999]. A high-velocity region is also present beneath the Tonga subduction region. In all models a clear change in the character of the fast regions is noticeable at about 2000 km depth, as seen by *van der Hilst and Kárason* [1999]. At the base of the mantle, very-long wavelength fast velocity anomalies surrounding the Pacific are common to all

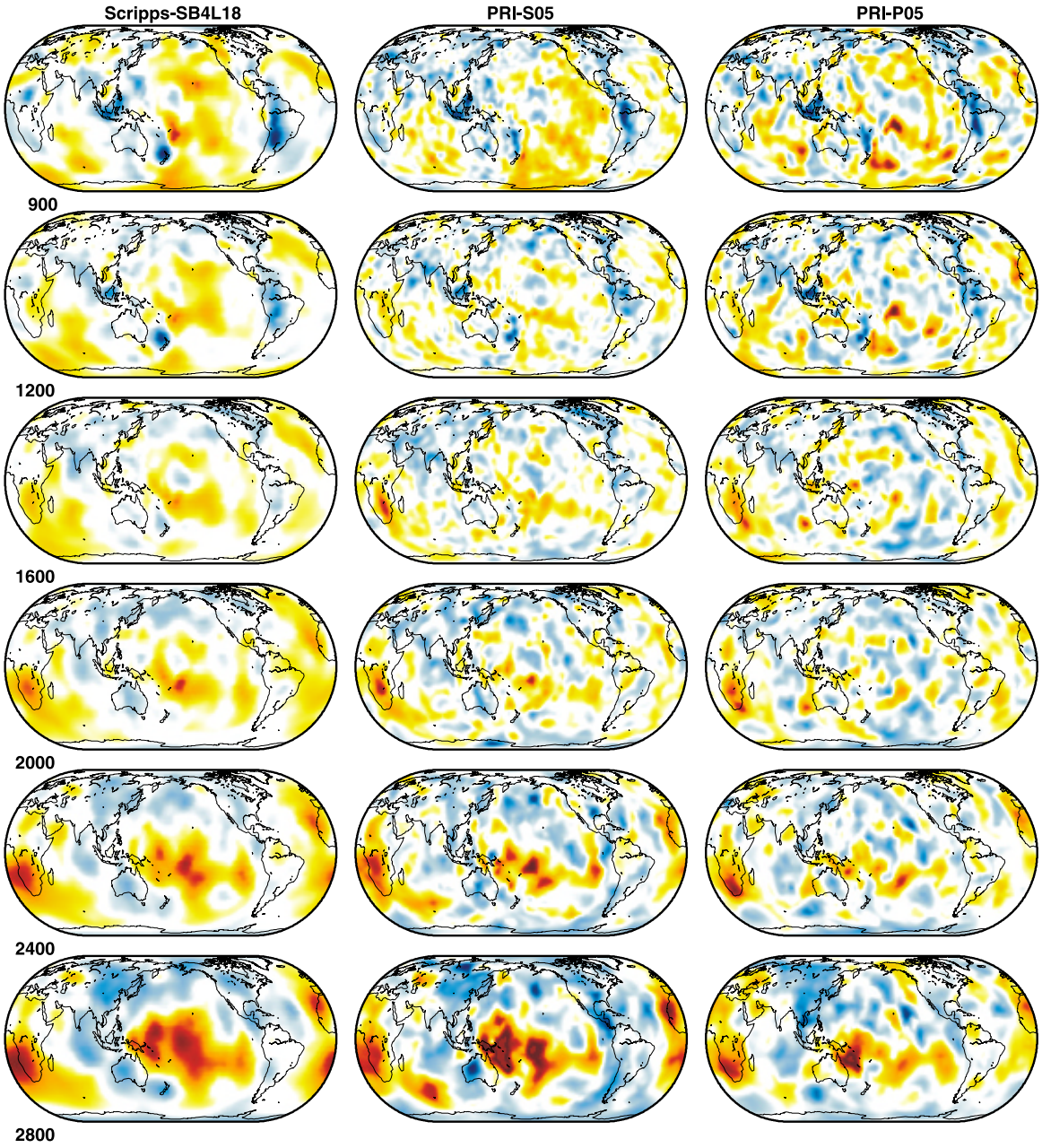

Figure 7. Cross sections at different depths (900, 1200, 1600, 2000, 2400, and 2800 km) in the lower mantle of the *S*-wave velocity models: Scripps, *SB4L18*; Princeton, *PRI-S05*, and Princeton, *PRI-P05*. Color scale is the same as in Figures 4–6.

models and are characterized by significantly higher velocity changes.

[19] In Figure 8 we provide a more quantitative analysis: Figure 8a shows the root-mean-square (rms) value of the anomalies of each *S*-wave model as a function of depth, and Figure 8b the correlation between each model and *PRI-S05*. Note that all models that include surface waves and/or free-oscillations have average amplitudes smaller than the purely body-wave models. This may indicate that wavefront healing affects the longer wavelengths. The root mean square (rms) amplitudes in *PRI-S05* are the largest over most of the depth range; they agree with those of *S&G* between 1200 and 2600 km. The figure suggests that we may divide the Earth up into two depth regions: below a depth of 1700 km the correlation exceeds 0.5 and models are in broad agreement with each other. At shallower levels the correlation coefficients not only sink below 0.5 (though *S20RTS* and *S&G*

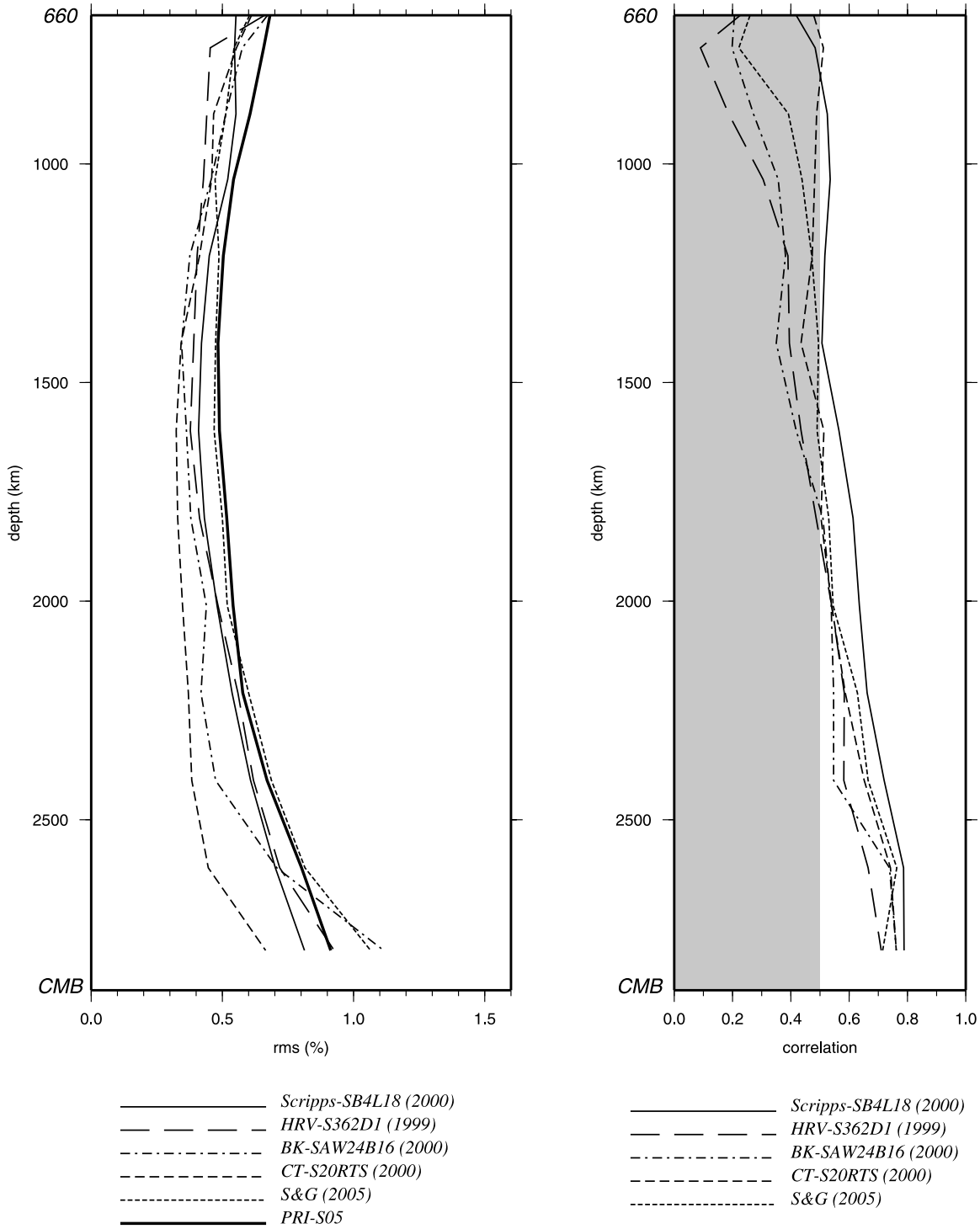

Figure 8. (left) Root-mean-square velocity perturbation $\delta v_S/v_S\%$ versus depth for the different *S*-wave velocity models. (right) Correlation coefficient between the *PRI-S* model and each of the shear-wave velocity model mapped in Figures 4–7.

remain close), but also disperse, an indication that models not only disagree with *PRI-S05* but also among each other. Part of this may be due to the different data sets (*S&G* and *PRI-S05* do not include surface-wave information); part of this also reflects the difficulty of imaging the dominantly small-scale heterogeneity at shallower depth. The correlation between *PRI-S05* and *SAW24B16* or

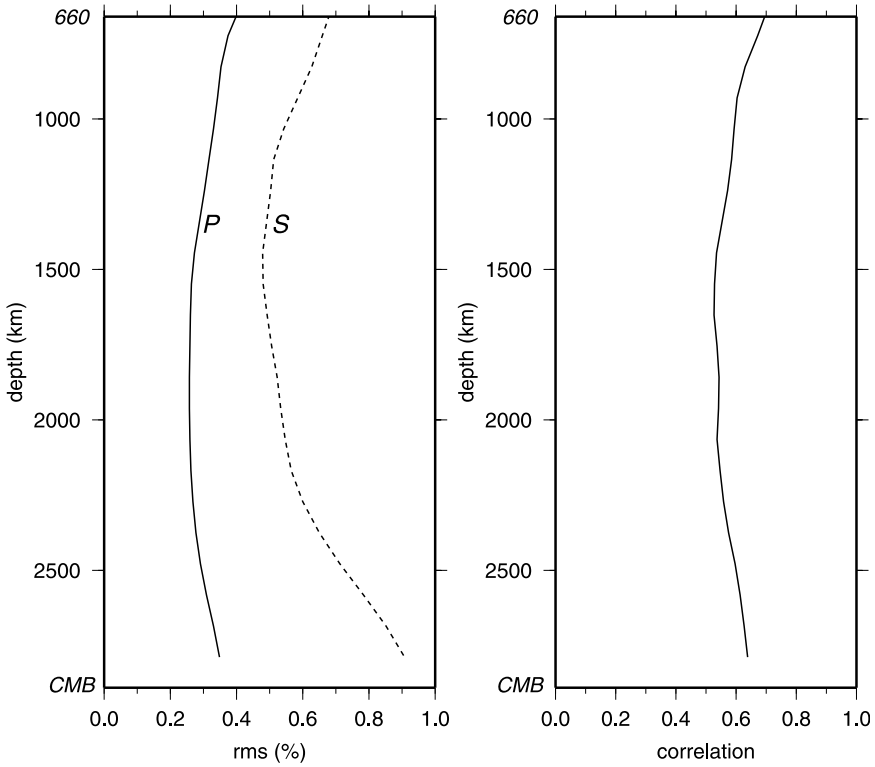

Figure 9. (left) Root-mean-square velocity perturbation $\delta v_S/v_S$% versus depth for model *PRI-S05* (dashed line) and $\delta v_P/v_P$% for model *PRI-P05* (solid line). (right) Correlation coefficient between model *PRI-S05* and *PRI-P05* versus depth.

S362D1 degrades to almost 0.2 near the 670 km discontinuity. A more extensive analysis of the correlation of the different models as a function of scale is presented in Appendix B, where we decompose the velocity maps of Figures 4–7 into spherical harmonics.

[20] Figure 9a compares the root-mean-square (rms) value of *PRI-S05* and *PRI-P05* as a function of depth. Amplitudes are significantly larger at the base of the mantle in the *S*-model, but in view of the absence of core-grazing *P* waves the low amplitude of *PRI-P05* near the core-mantle boundary is probably not significant. The correlation coefficient (Figure 9b) between the two models is around 0.6 at all depths.

[21] We conclude this section by observing that the most striking aspect of *PRI-P05* and *PRI-S05*, when compared to models inverted using classical ray theory, is the continuity of small-scale low-velocity anomalies with depth. Most of these anomalies are located nearby known hot spots, suggesting that these anomalies are lower mantle plumes feeding the hot spots. Note that neither the configuration of nodes (which are irregularly spaced), nor the choice of data (which exclude lower mantle body waves that travel close to vertical) are favoring vertical continuity of anomalies. The finite-frequency interpretation involves volume kernels with no preference for strong linear features. The regularization imposed in the inversion is isotropic and does not favor any particular direction. The vertical continuity of the anomalies must thus be a strong characteristic of the data, made visible by the correct interpretation using finite-frequency kernels, as this is the only feature that distinguishes *PRI-P05* and *PRI-S05* from each of the other models.

[22] To investigate the linearity of the deepest of such anomalies in both the *P*-wave and *S*-wave models, we compute the vertical average of the *S*-velocity anomaly $\delta v_S/v_S$ over the lowermost 1000 km of the mantle (1800 to 2800 km depth) and compare these with $\delta v_P/v_P$ in Figure 10. Such vertical averaging helps to emphasize structures that are vertically continuous over all or much of the lowermost mantle. Both images are dominated by the presence of the two superplumes. The anomaly beneath Africa is a broader upwelling beneath Europe, the Atlantic Ocean, the African continent, extending into the Indian Ocean. The *S*-wave Pacific "superplume" is a

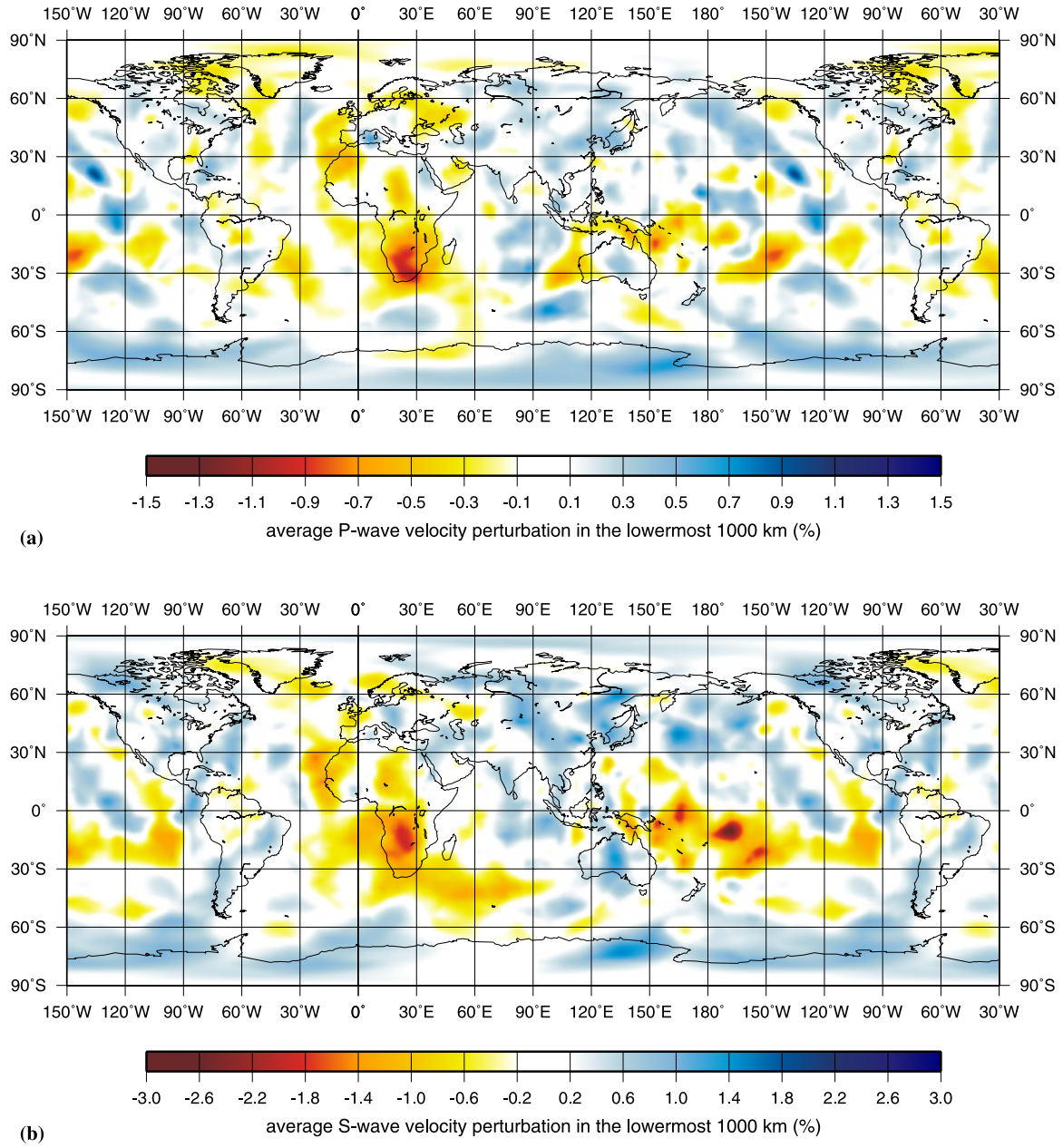

Figure 10. Vertical average over the lowermost 1000 km of the mantle of the relative velocity perturbation (a) $\delta v_P/v_P$ and (b) $\delta v_S/v_S$. The averaging emphasizes predominantly vertical features that are continuous with depth. Maps have been wrapped around to have complete views of both the Atlantic and the Pacific Oceans.

broad anomaly similar in character to that beneath Africa, but it is possible to distinguish individual plumes rising from the "superplume" beneath the Coral Sea (15°S, 155°E), east of the Solomon Islands (5°S, 165°E), Samoa (15°S, 168°W), Tahiti (18°S, 148°W) and near Easter Island (110°W, 25°S).

[23] With only one important exception, Iceland, *PRI-S05* confirms the depth extent of plumes inferred from *PRI-P05*. In some cases (e.g., Kerguelen), *PRI-S05* shows a lowermost mantle anomaly for deep plumes that is not well resolved at this depth by the *P*-wave tomography. Plumes whose depth extent is confirmed by the *S*-wave inversion are listed in boldface text in Table 1.

4. A Plume Catalogue

[24] In this section we discuss the plume images in model *PRI-S05* in detail, with reference to the updated *P*-wave model *PRI-P05*. We limit the

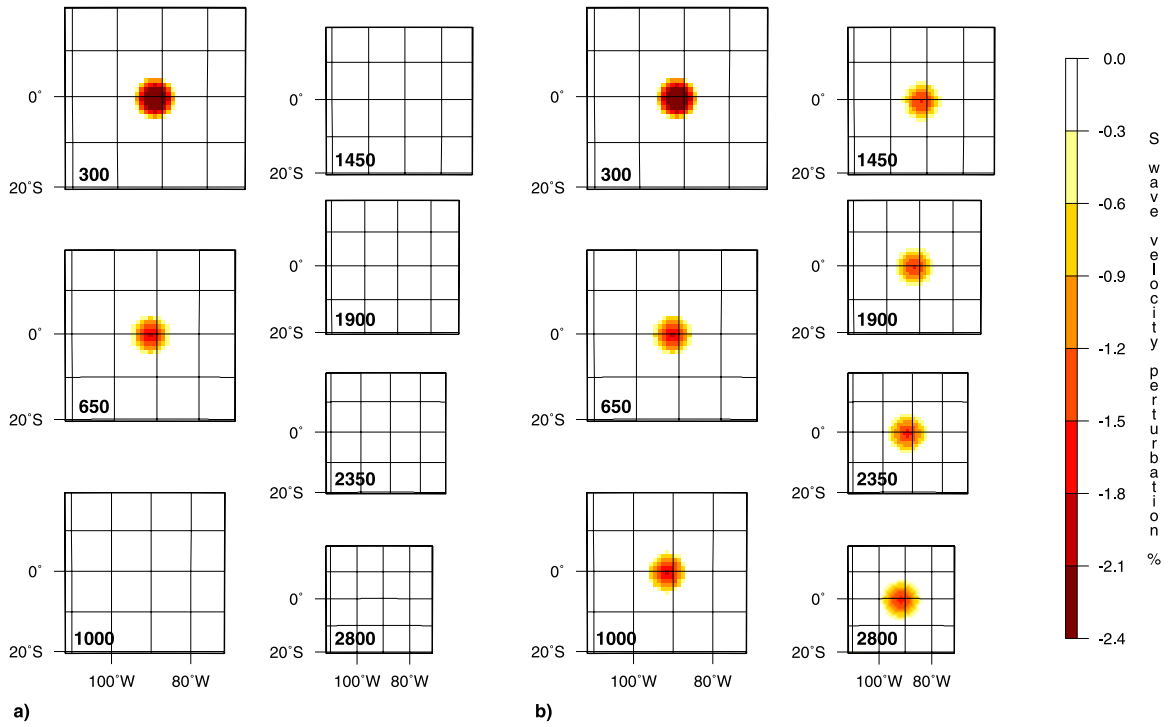

Figure 11. Example of synthetic plumes used in the resolution tests: (a) shows a plume of 400 km radius confined to the upper mantle and (b) represents a synthetic plume of 400 km radius reaching the core-mantle boundary at 2800 km depth. This example is centered on the equator at 92°W (Galapagos). In the resolution tests the plumes are centered at the geological locations listed in Table 1.

discussion to those aspects that are important for investigators who use these images to help interpret results from other disciplines. The list of references cited is therefore in no way intended to be complete; only where relevant for an evaluation of the reliability of the images do we cite papers outside of the realm of seismic tomography. Local tomographic studies are only cited when we felt compelled to discuss the upper mantle images, though most of the discussion is focused on the lower mantle where the finite-frequency method of interpretation improves significantly on ray theory.

[25] To avoid clutter, we show figures for only the most relevant of the sensitivity tests, though we often discuss resolution in words, and summarize the resolution studies for the deep plumes in Table 1. Figure 11 is the reference figure for all resolution figures. It shows the synthetic plume used as input in the tests. The six horizontal cross sections on the left show a synthetic plume extending down to the 660 km discontinuity, used to check if an upper mantle image "leaks" into the lower mantle. The right six images show a synthetic plume extending down to the core-mantle boundary, used to check for loss of resolving power with depth, and possible "smearing" in the horizontal direction. The test plume radius, 400 km, is close to observed plume sizes; other tests with narrower plumes are summarized in Table 1, where we list the minimum plume radius that would be resolvable at the 0.5% level in the image. We used maximum velocity perturbations of −1.65% below 1,000 km depth, −2% between 650 and 1,000 km depth, and −3.6% above 650 km depth which roughly correspond to a maximum temperature anomaly $\Delta T = 300$ K at the center of the plume, if we adopt the dv_S/dT given by *Karato* [1993].

[26] Well-resolved deep-mantle plumes are present beneath Ascension, Azores, Canary, Cape Verde, Cook Island, Crozet, Easter, Kerguelen, Hawaii, Samoa and Tahiti. Resolution is still lacking in the lowermost mantle beneath several hot spots: Afar, Atlantic Ridge, Bouvet(Shona), Cocos/Keeling, Louisville and Reunion. These plumes were not well resolved in the *P*-velocity model either, but we are of the opinion that there is sufficient evidence to conclude that they extend for at least some distance into the lower mantle. Midmantle plumes are present beneath Bowie, Hainan, Eastern Australia and Juan Fernandez. Unless these plumes are actually deep plumes with very thin tails originating from the D″ region, they seem not to originate

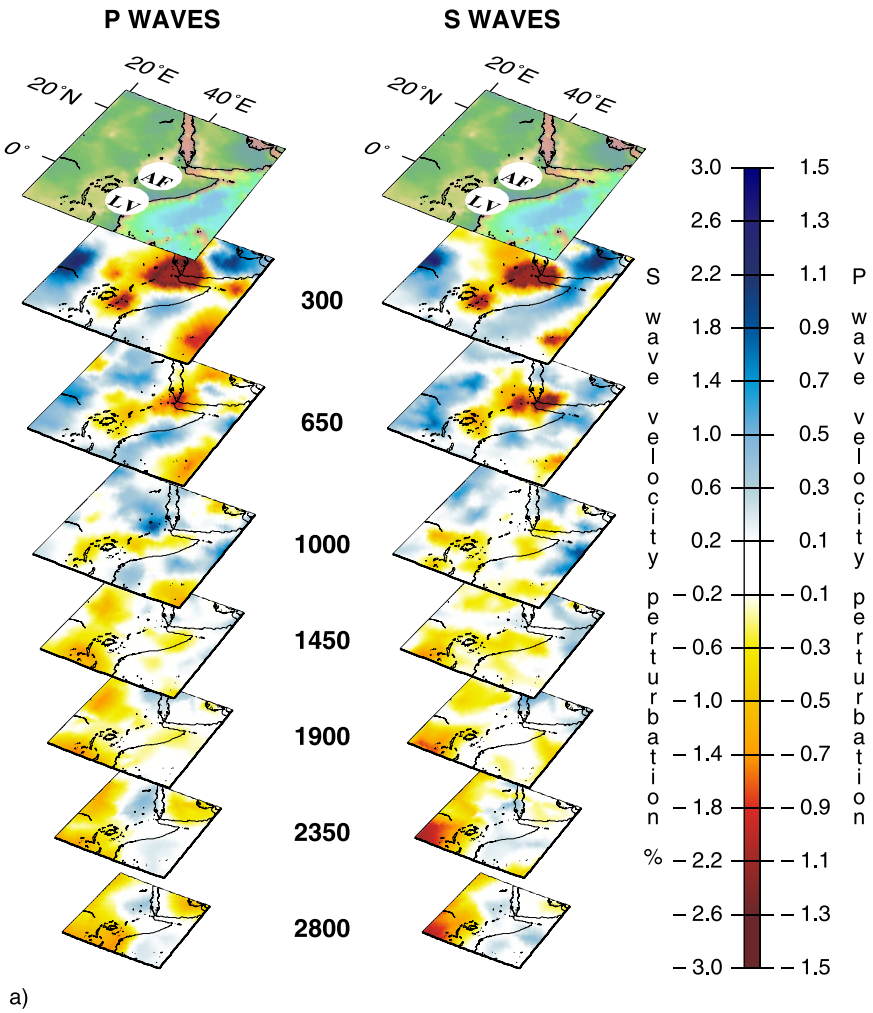

Figure 12. (a) Three-dimensional view of the plumes beneath the horn of Africa: AF (Afar) and LV (Lake Victoria) in both (left) *P*-wave and (right) *S*-wave tomographic models. Cross sections are 40° by 40° centered around the studied plume. Vertical scale has been exaggerated to avoid overlapping of the sections. (b) Same cross sections of the *S*-wave velocity model of Figure 12a (right) on a horizontal plane. AF (Afar) and LV (Lake Victoria). (c) Reconstructed synthetic plume confined in the upper mantle (Figure 11a). (d) Reconstructed synthetic plumes extending down to 2800 km depth (Figure 11b) for a resolution test beneath Afar and Lake Victoria. The reconstructed synthetic plume present in the lower right corners of Figures 12c and 12d is the plume beneath Seychelles.

from a known thermal boundary layer. Eifel and Seychelles cap plumes strictly confined to the upper mantle. Finally, developing plumes are confirmed to be present beneath South of Java, East of Solomon and in the Coral Sea.

[27] We discuss the imaged plumes below, in alphabetical order except where group of plumes are present.

4.1. Afar and Lake Victoria (Figure 12; Three Parts)

[28] Because of the presence of extensive hot spot tectonism, the East African Rift, and the Ethiopian uplift, the eastern part of Africa is an area particularly well studied [e.g., *Knox et al.*, 1998; *Jolivet and Faccenna*, 2000; *Nyblade et al.*, 2000a, 2000b; *Debayle et al.*, 2001; *Daradich et al.*, 2003]. Most recently, regional PASSCAL experiments have been used to better define the tectonic evolution of this region and the origin of the Afar hot spot [*Benoit et al.*, 2003, 2006; *Weeraratne et al.*, 2003; *Bastow et al.*, 2005]. *P*-velocity images from *Benoit et al.* [2006] show a low-velocity anomaly with a width between 100–400 km located beneath the Afar Depression. It dips southwest with depth and reaches 500 km (the limit of their model) beneath the Western Ethiopia Plateau. *Benoit et*

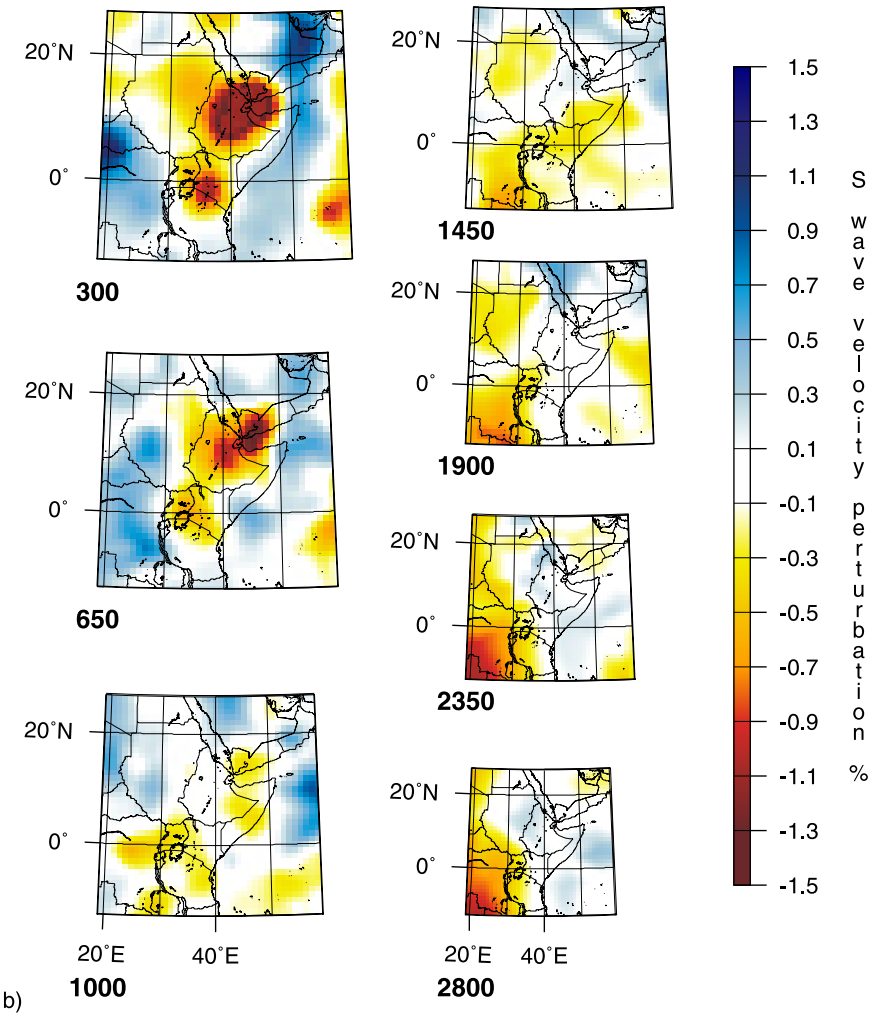

Figure 12. (continued)

al. [2006] suggest that this anomaly is an extension of the African superplume, in agreement with several global tomographic studies [*Grand et al.*, 1997; *Ritsema et al.*, 1999; *Ritsema and van Heijst*, 2000; *Grand*, 2002; *Zhao*, 2004].

[29] In both *PRI-P05* and *PRI-S05*, it is possible to isolate two large amplitude low-velocity anomalies beneath the Horn of Africa, one located beneath the Afar triple junction (42°E, 12°N) and the other located beneath the Tanzanian craton (32°E, 3°S). In *PRI-P05*, the two anomalies are isolated, but the *S* image is more ambivalent, showing a weak connection below 650 km. The anomaly beneath Tanzania dips westward and merges with the African superplume located beneath South Africa at the base of the mantle (Figure 13). Whereas it is clear that the lower mantle image of Afar is not an effect of leakage (Figure 12c), the weakening of the resolved synthetic image in the lower mantle (Figure 12d) directly beneath Afar suggests that Afar could actually reach the base of the mantle and that dipping of the anomaly southwest toward the African superplume in Figure 12a may indicate a connection between the two. The low-velocity regions beneath the Horn of Africa in the upper mantle agree with the anomalies mapped by *Debayle et al.* [2001] in a surface-wave study of the region. In Figure 13 we plot a cross section along the same great circle as the one shown by Figure 1B of *Ritsema et al.* [1999]. The connection of the anomaly beneath Lake Victoria with the African superplume is very similar in the two models.

4.2. Ascension/St. Helena (Figure 14)

[30] *PRI-P05* and *PRI-S05* agree down to about 650 km, where they both seem to indicate a merging of two separate upper-mantle plumes. The continuous lower-mantle plume that is visible in *PRI-P05* bending eastward and connecting down

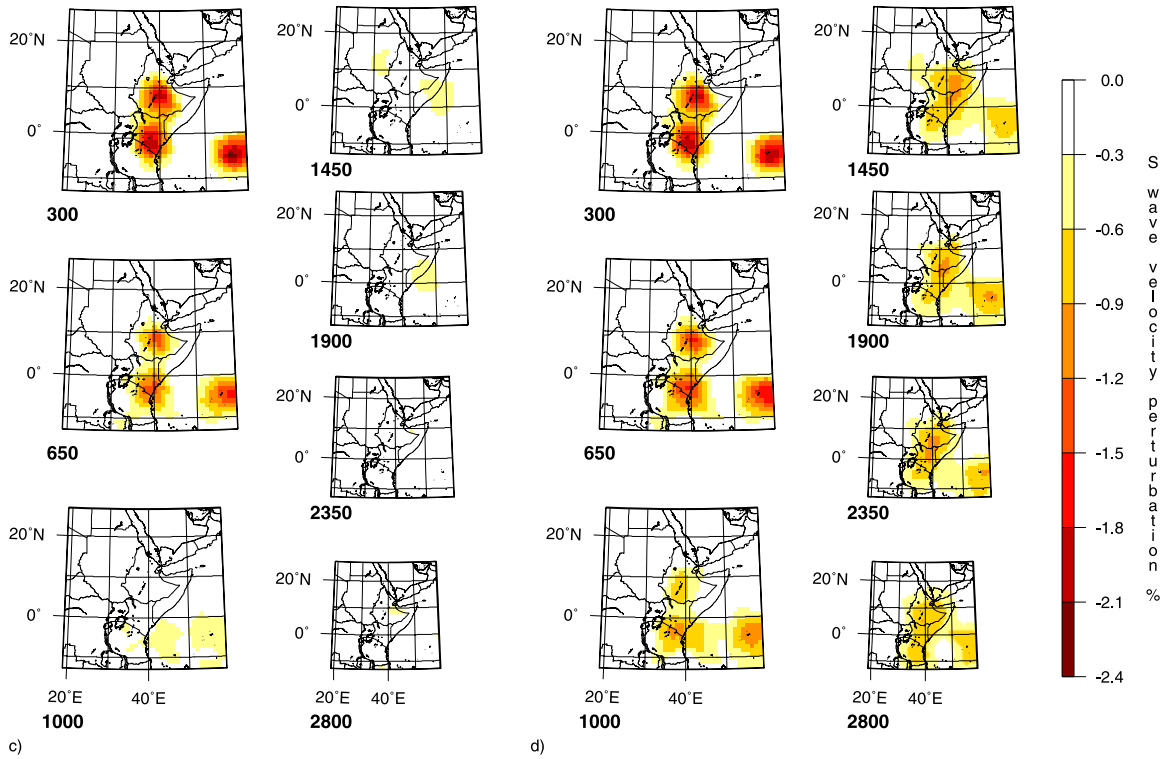

Figure 12. (continued)

to the African Superplume, but not well resolved, is not confirmed in *PRI-S05*. St Helena's low $^3He/^4He$ ratio also argues against a deep origin, or for extensive mixing with asthenospheric material (the $^3He/^4He$ ratios cited in this paper are from *Courtillot et al.* [2003]).

4.3. Atlantic Ridge (Figure 15)

[31] *PRI-P05* shows two plumes at 15°N and 25°N of which the southernmost extends to 1900 km depth. Though more blurred, both are visible in the upper mantle in *PRI-S05*. An axial hot spot was proposed at 22°N by *Sleep* [2002]. The disagreement between *P* and *S* can be explained by lack of resolution (not shown).

4.4. Azores/Canary/Cape Verde (Figure 16; Three Parts)

[32] These three adjacent plumes are robust deep features, appearing as isolated anomalies down to about 1000 km depth, where they merge and bend eastward with depth, reaching the base of the mantle off the coast of Africa beneath Canary at about 20–25°N (Figure 16), connecting to the superplume anomaly. Resolution is poor beneath Cape Verde in the upper mantle, explaining the lack of a strong signature of this plume near the surface. The resolution test shows well-resolved, independent features down to 1000 km but not deeper, so that we cannot rule out that the merging of the three plumes at the base of the mantle is a resolution artifact. We note that *O'Neill et al.* [2005] also propose a common source region at about 20°N for the three plumes on the basis of a geodynamic reconstruction in a fixed hot spot reference frame. The role of the Azores in this trio is not completely clear. In *PRI-P05* it merges with the other two, whereas in *PRI-S05* it seems almost to follow the predicted image for a vertical plume. Of these three hot spots, only Canary has a low $^3He/^4He$ ratio that would favor a shallow origin. Osmium isotopes suggest that Azores has a deep origin [*Schefer et al.*, 2002]. Although isotope data show intra-island variations, they all indicate involvement of the lower mantle in the source of the Cape Verde basalts [*Doucelance et al.*, 2003]. This is supported by the *PRI-P05*/*S05* images which contradict regional studies [*Silveira and Stutzmann*, 2002; *Silveira et al.*, 2006; *Pilidou et al.*, 2005] that suggest only a shallow signature for Azores, restricted to 200 km depth.

4.5. Bouvet/Shona (Figure 17)

[33] The image is centered on the Bouvet hot spot (54°S, 3°E), but also contains the location of the nearby Shona hot spot at 51°S, 6°W. Though *PRI-S05* and *PRI-P05* agree on the existence of

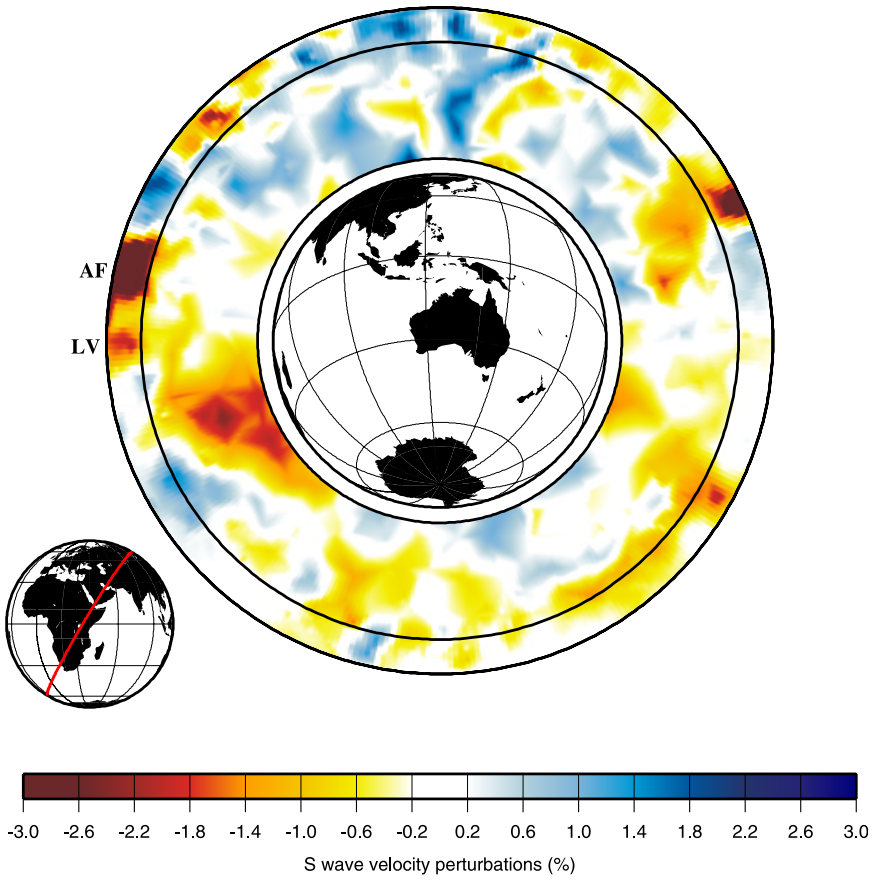

Figure 13. Cross section of the *PRI-S05* model through Africa and Lake Victoria (pole location 125.00°W, 30.64°S) Two-letter hot spot identifiers are listed in Table 1.

an upper-mantle low velocity beneath the Bouvet island hot spot, the lack of agreement in the lower mantle, and the poor resolution (there are no seismic stations) do not warrant a conclusive interpretation of the plume depth.

4.6. Bowie/Juan de Fuca/Cobb/Yellowstone (Figure 18; Three Parts)

[34] Bowie and Juan de Fuca/Cobb form a shallow, broad low velocity anomaly. In the uppermost 300 km of the upper mantle, Bowie becomes part of a widespread low-velocity anomaly that follows the coastline of North America. We conjecture that this anomaly is a leftover of the original spreading ridge of the Farallon plate, which may have been fed by Bowie, Juan de Fuca/Cobb and Guadalupe simultaneously. At about 650 km depth isolated anomalies appear, one of which is located beneath Bowie and extends down to 1000 km depth (no vertical leakage is observed in resolution tests). The location of this plume coincides with observations by *Nataf and VanDecar* [1993] of seismic wave diffraction near the top of the lower mantle.

[35] Geologically, Yellowstone represents a typical hot spot, with a 16 million-year-old, age-progressive linear volcanic chain and a southwest-widening topographic swell [*Saltzer and Humphreys*, 1997; *Humphreys et al.*, 2000; *Waite et al.*, 2006]. It has a high $^{3}He/^{4}He$ ratio. The absence of a deep Yellowstone plume in both *PRI-P05* and *PRI-S05* km is therefore surprising, and we discuss the discrepancy in some detail. The upper-mantle anomaly is much lower in strength than the broad low-velocity zone that extends south of it. At 660 km only *PRI-S05* shows an anomaly and nothing is visible below 1000 km depth. Resolution tests show that though a deep plume of 200 km radius and a velocity contrast of 0.3% should be visible but anything narrower would be invisible using our data set, and we suspect this is the main reason for the difference between global and regional inversions by *Saltzer and Humphreys* [1997], *Humphreys et al.* [2000], *Waite* [2004], and *Waite et al.* [2006]. In these studies Yellowstone caps a narrow plume of about 100 km in radius, confined to the uppermost 350 km depth,

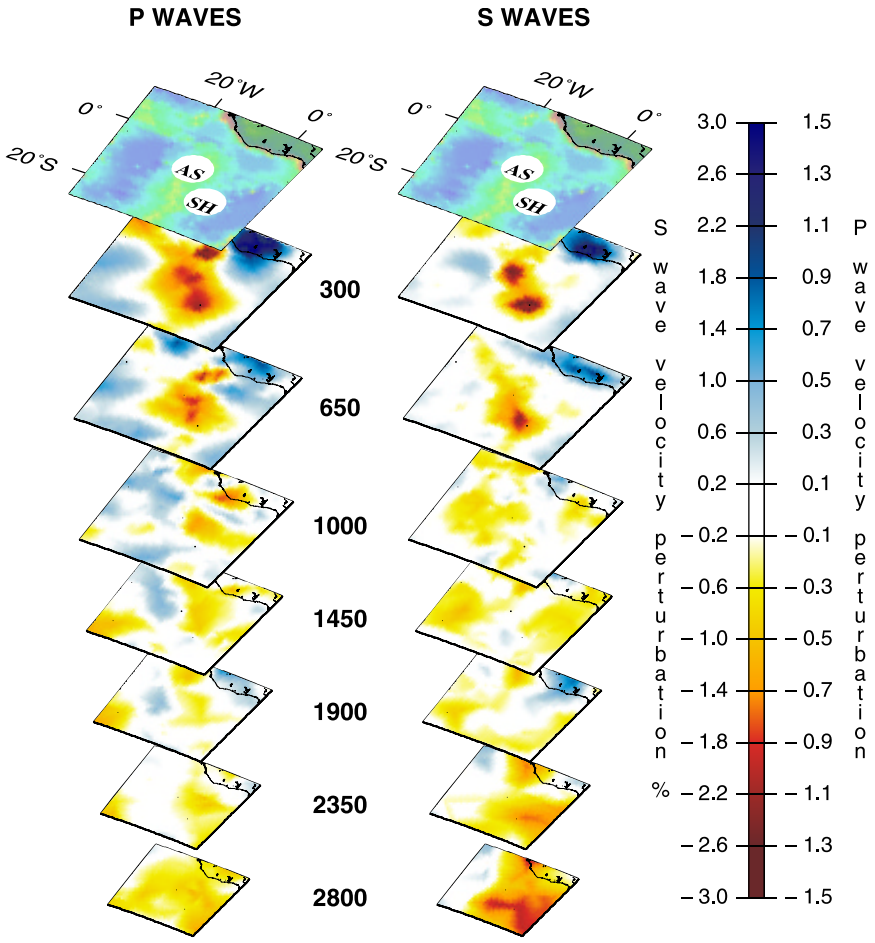

Figure 14. Three-dimensional view of the plumes beneath the Ascension and St. Helena in both the (left) *P*-model and (right) *S*-model. Plotting format as in Figure 12a.

which would be hard to detect in our global tomographic study. *Waite et al.* [2006] show the results of both a P wave and a S wave tomographic study which confirm the presence of a strong low-velocity anomaly from 50 to 200 km depth right beneath the Yellowstone caldera and eastern Snake River Plain. A weaker anomaly extends down to about 400 km, dipping about 30° west-northwest from the vertical. The low velocity body is accompanied by a fast velocity anomaly suggestive of downwelling colder, denser mantle material. They interpret the low velocity body as a plume of upwelling hot material rising from the transition zone which would promote small-scale convection in the upper 200 km of the mantle and would explain the long-lived volcanism. Because of the ambiguity in our models, Yellowstone is not listed in Table 1.

4.7. Chatham (Figure 19)

[36] *PRI-S05* and *PRI-P05* show a strong and wide low-velocity anomaly that extends between 600 km to about 1450 km depth beneath the Chatham Rise, a topographic high that stretches for about 800 km east of South Island at 44°S. It may connect at 600 km depth to the anomaly labeled "Louisville" (Figure 35). While most of the global models show a broad low-velocity anomaly SW of New Zealand near 600 km, it extends to deeper levels only in *S20RTS*, *S&G* and *SB4L18*. The absence of a surface connection agrees with the absence of a known hot spot at the surface. It is tempting to speculate that this anomaly is somehow associated with the Cretaceous flood basalts of the Hikurangi Plateau now found North of Chatham Island, which are suspected to be the remnants of the breakup of Gondwana [*Segev*, 2002]. It represents the only possible observation in our models of a plume head, but is in need of confirmation by more dedicated study.

4.8. Cocos (Keeling)/South of Java (Figure 20)

[37] Both *PRI-P05* and *PRI-S05* show a plume directly beneath Cocos (Keeling) Islands to

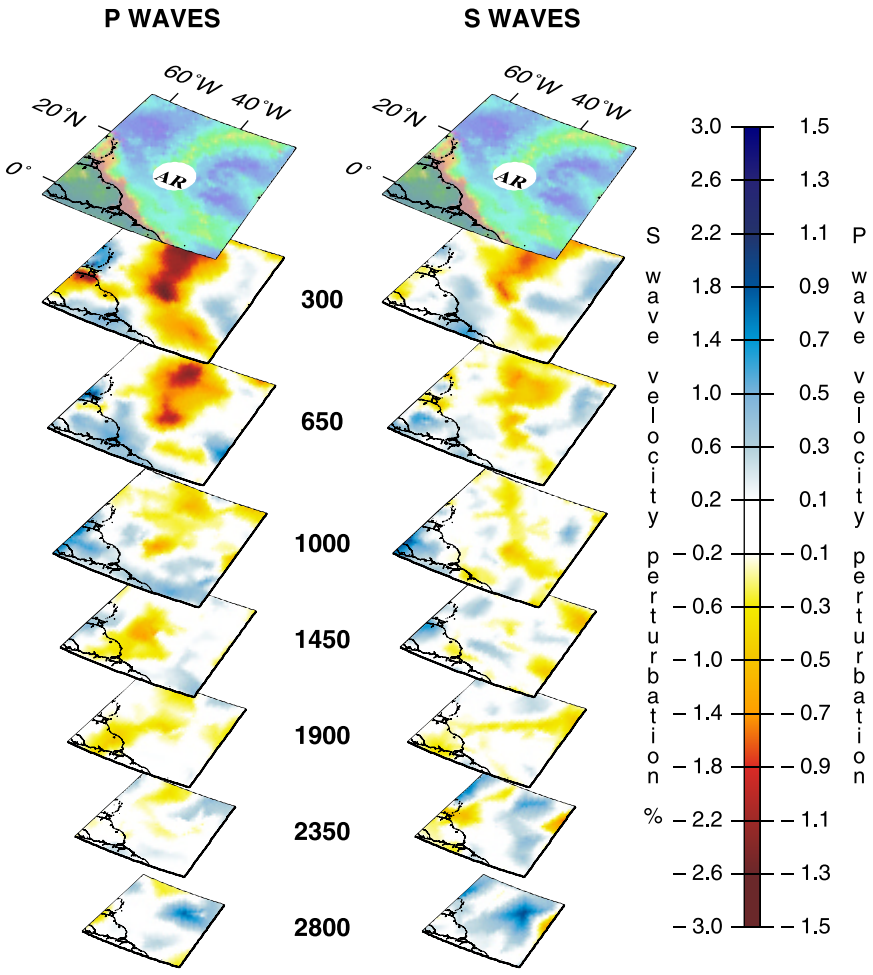

Figure 15. Three-dimensional view of the plumes beneath the Atlantic Ridge in both the (left) *P*-model and (right) *S*-model. Plotting format as in Figure 12a.

1000 km depth. The resolution test (not shown) indicates that the lower-mantle plume is not an effect of leakage, but poor resolution at larger depth precludes any definite interpretation about the depth of the source region. A starting plume rising from the base of the mantle beneath South of Java is visible in *PRI-P05* but not convincingly confirmed by the very weak anomaly in *PRI-S05*.

4.9. Cook Island/Samoa/Tahiti/Macdonald (Figures 21 and 22)

[38] Samoa, Cook Island and Tahiti are closely spaced but separate anomalies seen to be emanating from the central region of the Pacific superplume. This deep origin is in agreement with high observed ^{3}He/^{4}He ratios. *PRI-P05* and *PRI-S05* are in agreement about many of the more detailed features of this system: Samoa and Cook Island are isolated anomalies down to 1450 km. Tahiti is the strongest plume visible in the lower mantle, strong enough to appear as a plume in the ray-theoretical tomographic images by *Zhao* [2004] and even in model *S20RTS*. The differences in amplitude of the anomaly in midmantle (around 1000 km) may be ascribed to lack of resolution. Resolution improves with depth, and the remarkable mismatch in the anomaly near the core-mantle boundary is reminiscent of the anticorrelation between shear and bulk modulus anomalies (*Ishii and Tromp* [2004] and references therein).

4.10. Coral Sea/East of Solomon/Caroline (Figures 23 and 24)

[39] Two small "starting plumes" extend from the westernmost edge of the Pacific superplume. The smallest, beneath the Coral Sea, reaches upward to a depth of 2350 km, whereas a plume east of the Solomon Islands is visible in the northeast corner

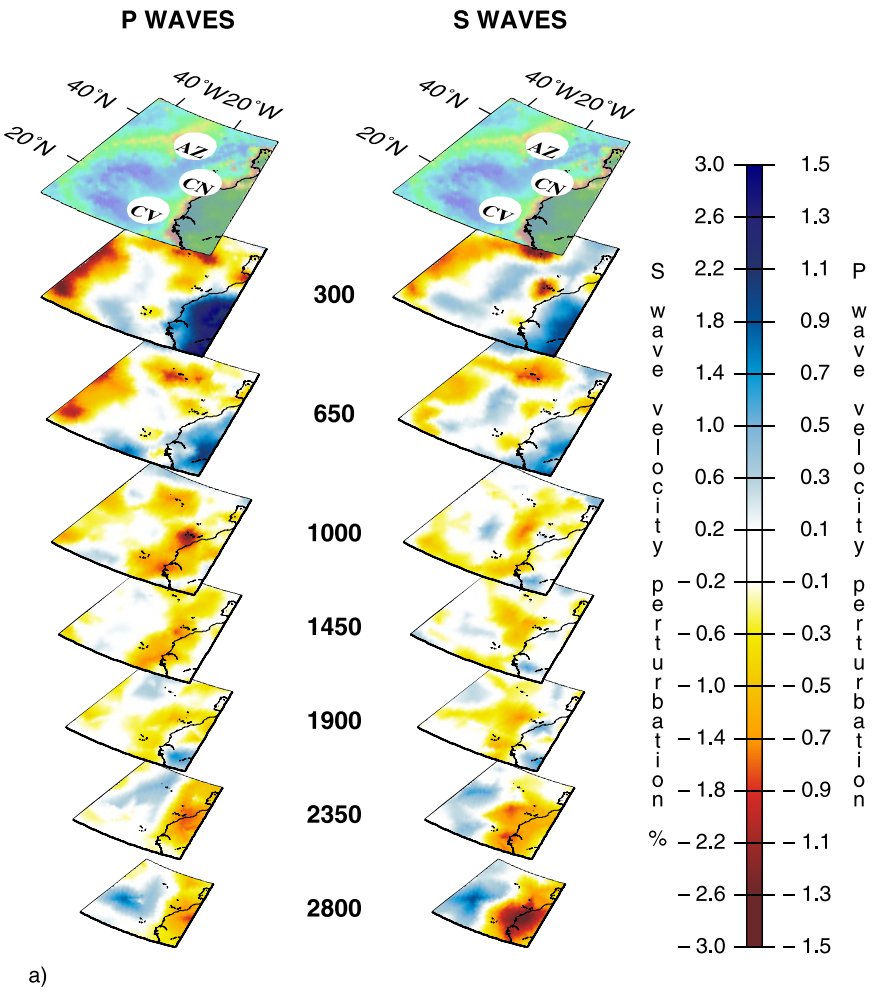

Figure 16. (a) Three-dimensional view of the plumes beneath AZ (Azores), CN (Canary), and CV (Cape Verde) in both (left) *P*-wave and (right) *S*-wave tomographic models. Plot format as in Figure 12a. (b) Same cross sections of the *S*-wave velocity model of Figure 16a (right) on a horizontal plane. (c) Reconstructed synthetic plume confined in the upper mantle (Figure 11a). (d) Reconstructed synthetic plumes extending down to 2800 km depth (Figure 11b) for a resolution test beneath Azores, Canary, and Cape Verde.

of the figure to 1000 km depth (Figure 23). *PRI-P05* and *PRI-S05* are largely in agreement, though only *PRI-P05* suggests a merger with the low-velocity anomaly beneath the Caroline Islands (Figure 24).

4.11. Crozet/Kerguelen (Figure 25)

[40] Figures 7 and 10 strongly suggest that the Kerguelen/Crozet and the Canary/Cape Verde/Azores complex, together with the African superplume, form a large low-velocity region near the core-mantle boundary that may contribute strongly to the spreading of both the Atlantic and Indian oceans. Kerguelen is a deep plume in *PRI-S05*. From the surface, Kerguelen follows the same trajectory in both *PRI-P05* and *PRI-S05* down to 1900 km depth: the plume bends slightly in the northwest direction of the African superplume, but only *PRI-S05* shows a pronounced anomaly in the deepest mantle which is well resolved for a plume of 400 km radius. Plumes seems to merge at about 1450 km in both models but this may be due to lack of sufficient resolution in the midmantle. Resolution is also lacking in *PRI-P05* beneath 1900 km depth.

4.12. Easter/Juan Fernandez (Figure 26)

[41] Despite differences in detail, *PRI-S05* and *PRI-P05* show a very similar behavior for the deep plume beneath Easter Island: it extends clearly to 1000 km, then loses strength, even though it is well resolved, but is again clearly visible north-northeast of the island location near the core-mantle boundary,

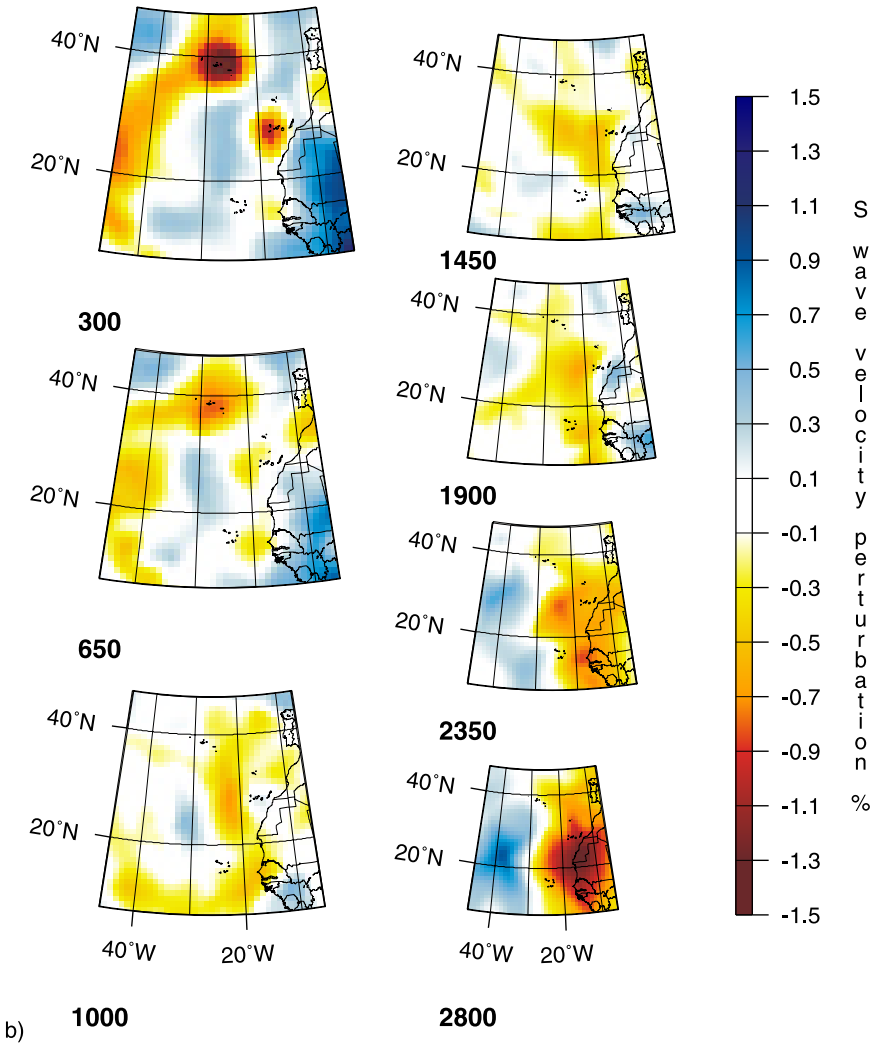

Figure 16. (continued)

especially in *PRI-S05*. A deep origin for Easter is in accordance with the high observed $^{3}He/^{4}He$ ratio. This ratio is also high for basalts found on Juan Fernandez, but whereas *PRI-P05* seems to indicate a separate plume below Juan Fernandez, down to 1000 km, the corresponding anomaly in *PRI-S05* is too weak to allow us to draw a definite conclusion.

4.13. Eastern Australia (Figure 27)

[42] The large region of low seismic velocities, extending in the upper mantle from Eastern Australia to Lord Howe toward the northeast and further southeast to (52S 160E) in *PRI-P05* is only partially confirmed in *PRI-S05*, where anomalies tend to be more localized and smaller in amplitude. Though a lower-mantle extension under Eastern Australia is suggested in *PRI-S05*, this is not confirmed in the *P*-velocity anomalies. Vertical leakage is unable to explain the signature of Eastern Australia in the lower mantle in *PRI-S05*. Resolution is also good in *PRI-P05*, suggesting a real anticorrelation between the *P*-wave and *S*-waves anomalies beneath Eastern Australia.

4.14. Eifel (Figure 28; Three Parts)

[43] Because of the large station density in Europe, Eifel is one of the few plumes for which we dare make inferences in the upper mantle. A plume extending to 650 km would show up at that depth (Figures 28b and 28c), but instead both *PRI-S05* and *PRI-P05* show an image only at shallower depth. Only a trace at 1500 km depth of the lower-mantle plume that was imaged using ISC data only by *Goes et al.* [1999] is visible in *PRI-P05*. Recent regional studies by *Ritter et al.* [2001] and *Pilidou et al.*

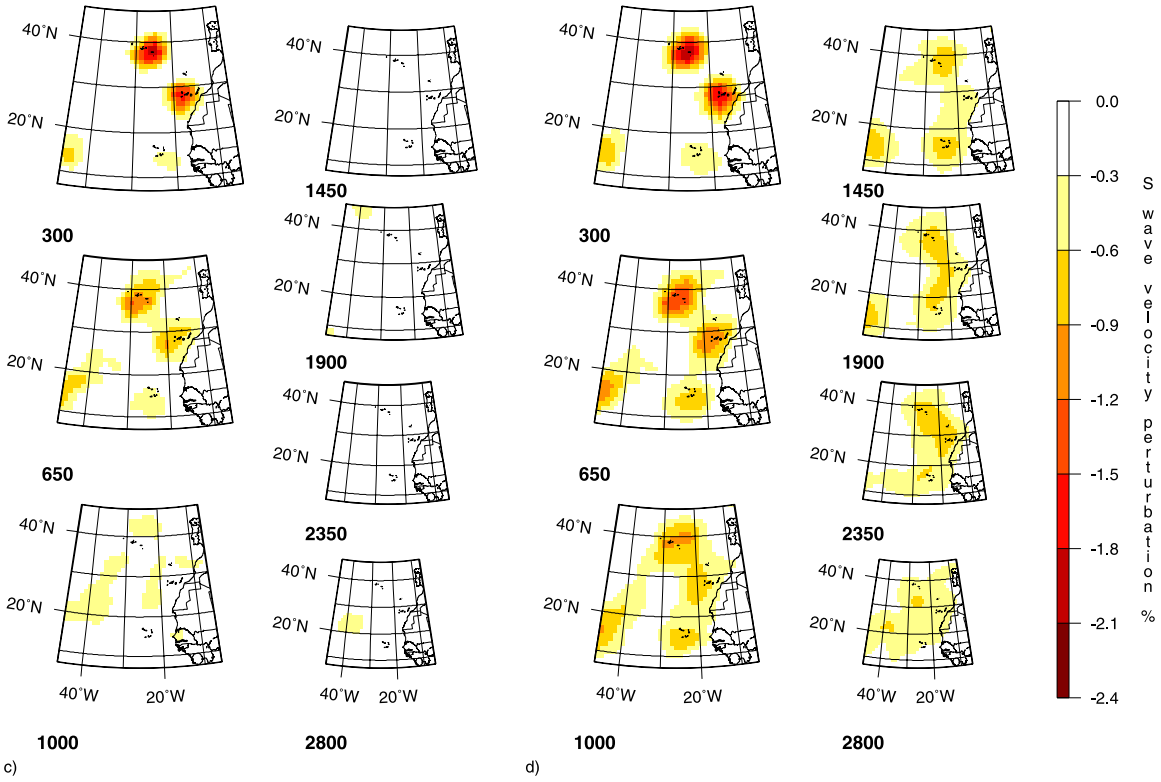

Figure 16. (continued)

[2005] also fail to image a plume below 400 km depth.

4.15. Etna (Figure 28; Three Parts)

[44] Though at first sight Etna may seem to be a typical back-arc volcano, magma from Mount Etna is undergoing a compositional change which reflects a progressive transition from a predominant mantle-plume source to subduction related basalts [*Tanguy et al.*, 1997; *Gvirtzman and Nur*, 1999; *Schiano et al.*, 2001; *Clocchiatti et al.*, 2004]. While a shallow low-velocity anomaly is clearly present in the *PRI-S05* model, it is not visible in the *PRI-P05* model. In the *S*-wave model, the anomaly beneath Etna is confined to the upper mantle, above 650 km depth, and is well resolved. A similar feature has been recently identified beneath Etna by *Marone et al.* [2004] in a surface-wave tomographic study.

4.16. Erebus (Figure 29)

[45] *Storey et al.* [1999] suggest that there are currently two mantle plumes beneath West Antarctica: one beneath the Marie Byrd Land (110°W, 80°S) and the other beneath Mt. Erebus (167°E, 78°S), the large active volcano on Ross Island. However, this model is unable to explain the wide distribution of compositionally similar igneous rocks in northern Victoria Land, New Zealand and Australia, which seem to favor the impingement of a single plume head [*Rocchi et al.*, 2005; *Behrendt et al.*, 1994]. In fact, both *PRI-P05* and *PRI-S05* show a single low-velocity anomaly beneath Erebus down to 1000 km depth. It is a rather circular large amplitude anomaly (−3%), within a broader slow region extending to about 60°S, but not as far as Eastern Australia as shown by *Rocchi et al.* [2005]. *Rocchi et al.* [2005] claim that the broad anomaly from Tasmania to the Ross Sea is related to a linear geodynamic feature more than 4000 km long that matches the belt of Southern Ocean fracture zones, but our tomographic images suggest a rather deep isolated conduit down to about 1000 km depth.

4.17. Galapagos (Figure 30; Three Parts)

[46] Both *PRI-P05* and *PRI-S05* models show a plume extension down to about 1900 km, which agrees with the characterization of the basalts of Galapagos by high $^{3}He/^{4}He$. In both models, the plume is still visible north of Galapagos to 1900 km depth. It does not connect to the Easter plume visible in the southwest corner of the image between

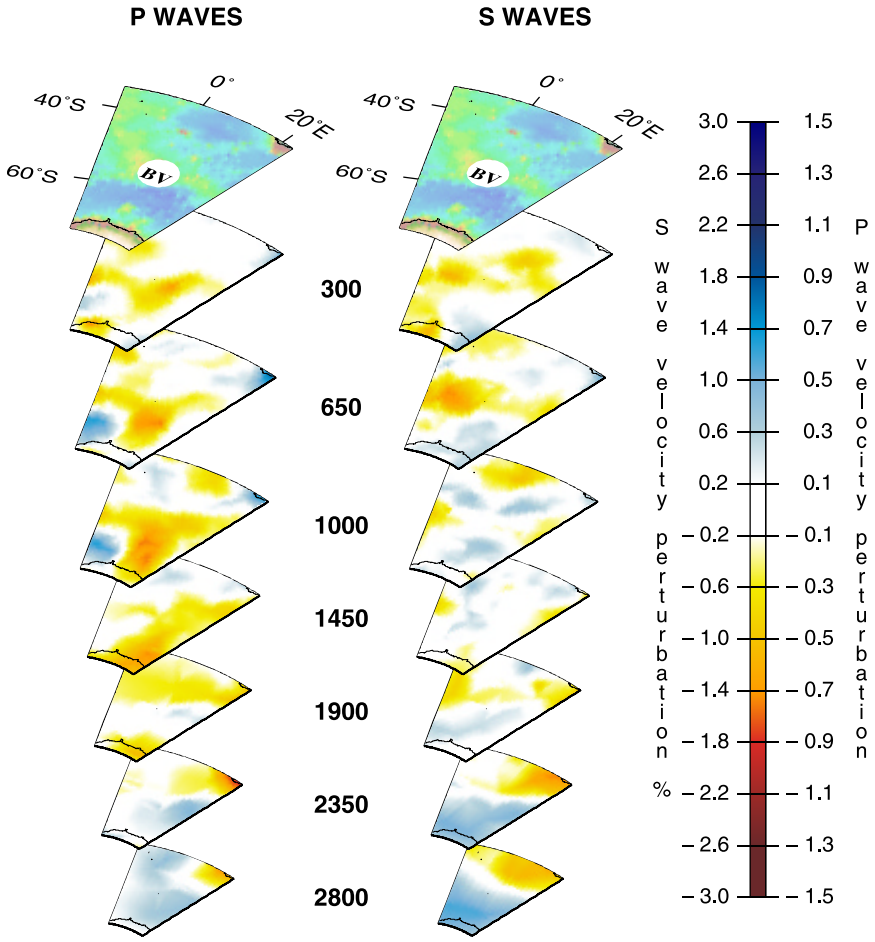

Figure 17. Three-dimensional view of the plumes beneath Bouvet and Shona in both the (left) *P*-model and (right) *S*-model. Plotting format as in Figure 12a.

the core-mantle boundary and 1900 km depth. There is no significant vertical leakage from the upper mantle beneath Galapagos; however, resolution is lacking below 1900 km and we remain uncertain about the exact depth extent of its source region.

4.18. Hainan (Figure 31; Three Parts)

[47] Hainan caps a weak but resolved plume visible down to about 1900 km depth in *PRI-S05*, confirming a deep mantle origin for this plume which reaches to 1450 km depth with a very weak signature at 1900 km in *PRI-P05*. First seen by *Lebedev* [2000], the shallow low-velocity anomaly is located just off the coast of China, but at deeper levels it continues below South East Asia, suggesting perhaps an asthenospheric connection with the past volcanism on the island of Hainan. It is not an effect due to vertical leakage and resolution tests show that any extension below 1900 km would have to be narrower than 200 km in radius to remain invisible.

4.19. Hawaii (Figure 32; Three Parts)

[48] At a depth of 1000 km, the Hawaii image stretches out in the southeast direction, which is not the northeast/southwest direction of smearing predicted by the sensitivity test for a simple cylindrical plume. At 1450 km depth, a strong anomaly develops northwest of Hawaii, despite the fact that the resolution diminishes considerably. Up to this depth *PRI-S05* and *PRI-P05* agree. At deeper levels, *PRI-S05* does not show the splitting of the plume into the two isolated conduits that characterize *PRI-P05*. A single conduit is traceable down to about 1900 km depth where it vanishes in *PRI-S05*, whereas it reaches the core-mantle boundary in *PRI-P05*. In the lower mantle, Hawaii is not the giant plume it appears to be from its surface activity, and Tahiti surpasses it

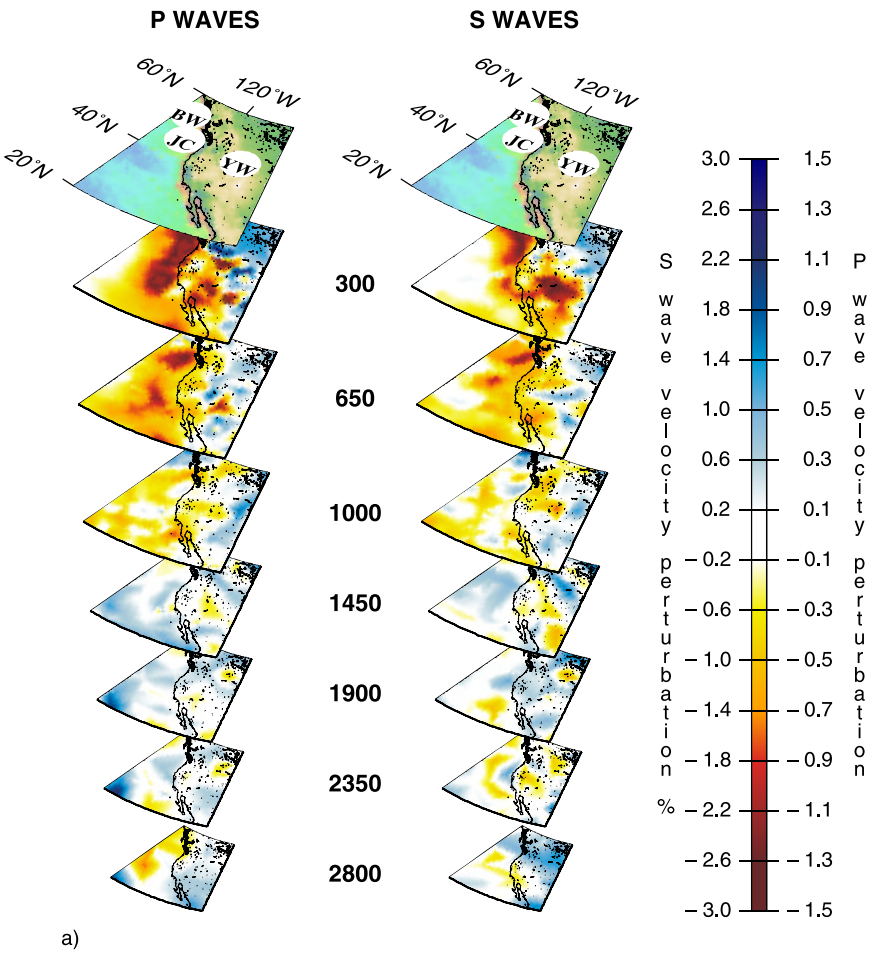

Figure 18. (a) Three-dimensional view of the plumes beneath BW (Bowie), JC (Juan de Fuca), YW (Yellowstone) in both (left) *P*-wave and (right) *S*-wave tomographic models. Plotting format as in Figure 12a. (b) Same cross sections of the *S*-wave velocity model of Figure 18a (right) on a horizontal plane. (c) Reconstructed synthetic plume confined in the upper mantle (Figure 11a). (d) Reconstructed synthetic plumes extending down to 2800 km depth (Figure 11b) for a resolution test beneath Bowie, Juan de Fuca, and Yellowstone.

in strength. Located in the middle of the Pacific, far from regions of high seismicity or dense station networks, Hawaii is poorly sampled by seismic rays that could provide the necessary resolution to image it accurately; we must await the results of ocean-bottom seismographic experiments before drawing any more definite conclusions.

4.20. Iceland (Figure 33; Three Parts)

[49] The depth extent of Iceland plume is controversial, and the issue is at the center of an escalated debate in which the mantle plume hypothesis itself is questioned [*Foulger*, 2003]. The existence of an upper-mantle plume is not disputed: [*Wolfe et al.*, 1997; *Foulger et al.*, 2001; *Allen et al.*, 2002; *Hung et al.*, 2004]; all agree on the presence of a strong, roughly 200 km wide, low-velocity anomaly beneath Iceland that extends down to at least 400 km depth. Though the $^{3}He/^{4}He$ ratio is high, *Foulger et al.* [2001] dispute the existence of a lower-mantle plume and reject earlier *P*-wave tomography by *Bijwaard and Spakman* [1999], *Rhodes and Davies* [2001] and *Zhao* [2004]. *S20RTS* sees an *S* velocity anomaly strictly confined to the upper mantle, unconnected to a strong lowermost mantle anomaly in the same area, originally found by *Helmberger et al.* [1998]. On the other hand, a lower-mantle extension is implied by a thinning of the transition zone [*Shen et al.*, 1996, 1998].

[50] The finite-frequency tomography gives an equally ambiguous message. In both *PRI-S05* and *PRI-P05*, the Iceland plume is absent around 1000 km depth, but in the *S* model it recovers at 1450 km and extends almost all the way to the

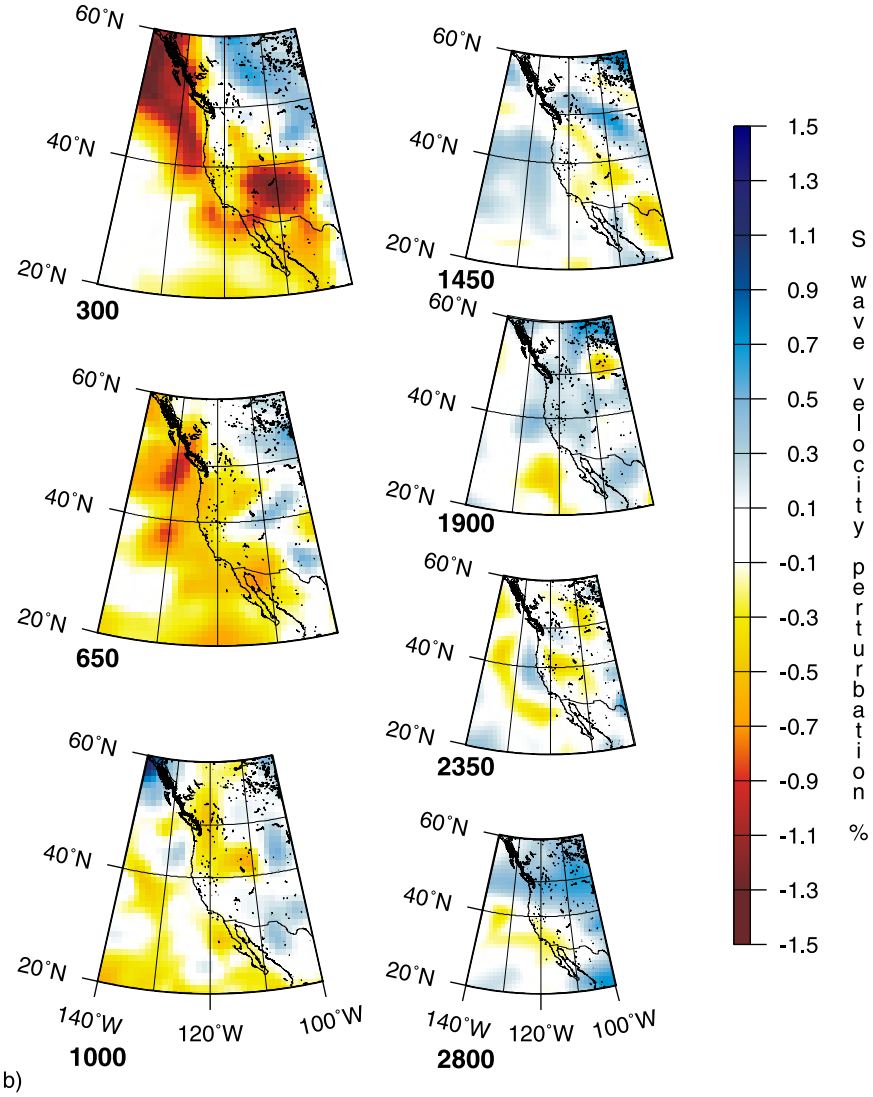

Figure 18. (continued)

core-mantle-boundary (see also Figure 10). *PRI-S05* shows no vertical leakage, and the resolution in the midmantle is as good as that for *PRI-P05* [*Montelli et al.*, 2004a, Figure S15]. We therefore retract the classification in *Montelli et al.* [2004a] of Iceland as a shallow plume, and consider the matter reopened. In fact, the image of *PRI-S05* is reminiscent of the image of the pulsating plume observed in laboratory experiments by *Olson* [1990]. The resolution calculations we performed did not include plumes with strong variations of the strength with depth, but it is clear that such variations render the image more dependent on the precise ray geometry, perhaps explaining the wide diversity of results in the literature. Supporting evidence for a pulsating plume comes from the sedimentary record [*White and Lovell*, 1997], and from argon dating of episodic seamount volcanism across the North Atlantic volcanic province [*O'Connor et al.*, 2000]. Numerical modeling shows that a pulsating plume can generate the prominent V-shaped crustal lineations straddling the Reykjanes ridge, south of Iceland [*Ito*, 2001].

4.21. Indian Ocean (Figure 34)

[51] *PRI-P05* shows a plume anomaly centered at 95°E, 42°S bending eastward and reaching the base of the mantle just off the coast of Australia. *PRI-S05* agrees with this down to 1900 km, though the image is more ambiguous. There are no seismic stations close and the resolution is not particularly good beneath this location in the *PRI-S05* model, explaining the lack of a strong signature of the conduit at depth.

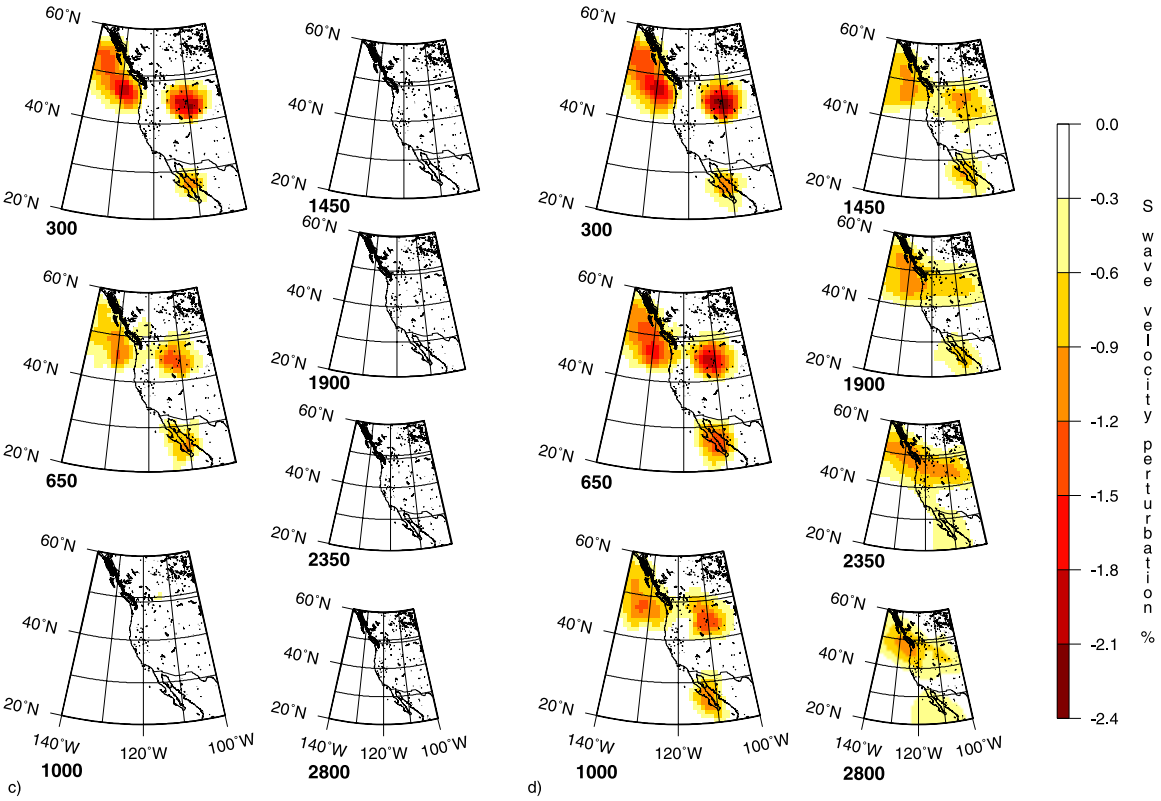

Figure 18. (continued)

4.22. Louisville (Figure 35)

[52] Like Hawaii, the Louisville hot spot is characterized by a well-defined chain of aging volcanoes. *PRI-P05* and *PRI-S05* do not show a plume beneath either of two disputed present-day locations [*Sleep*, 1990] but agree on a plume image located beneath the hot spot track at 55°S and 150°W. In *PRI-S05* a vague, smeared anomaly is traceable all the way down to the core-mantle boundary but it is poorly resolved and not confirmed in *PRI-P05*.

4.23. Reunion/Seychelles (Figure 36)

[53] *PRI-S05* and *PRI-P05* agree on a lower-mantle plume that deflects in the southwest direction, toward the African superplume, below 1000 km depth. Though the resolution for *PRI-P05* is still good at 1000 km, the *S* anomalies are weaker and the deeper extension is not reliably imaged in either model. The lower-mantle extension for Reunion is supported by a thinning of the transition zone [*Li et al.*, 2001] and by a high $^{3}He/^{4}He$ ratio. Both models show a second anomaly located north of Reunion, approximately beneath the Seychelles (5°S, 56°E), and confined to the upper mantle. A plume-like feature beneath Seychelles is of particular interest since Seychelles is a continental fragment rifted off India at the time of the Deccan traps. Though its plume trail is commonly assumed to be associated with the Reunion hot spot [*Todal and Edholm*, 1998], the images give evidence of a separate upwelling.

5. Plume Dynamics in the Mantle: Implications

[54] As the review of the imaged plumes in the previous section clearly shows, the new *S*-wave results and the revised model *PRI-P05* in this paper provide a strong confirmation of the earlier conclusions drawn from *PRI-P04* [*Montelli et al.*, 2004a]. This good agreement allows us to interpret some of the secondary features in the images with more confidence. None of the plume images show the textbook "head-tail" structure generally associated with plumes [*Olson and Singer*, 1985; *Campbell and Griffiths*, 1990]. If the blob imaged below Chatham is a plume head, its shape is a far cry from the mushroom-shaped head with entrainment at the edges predicted by laboratory experiments, and we fail to image a tail beneath it. The

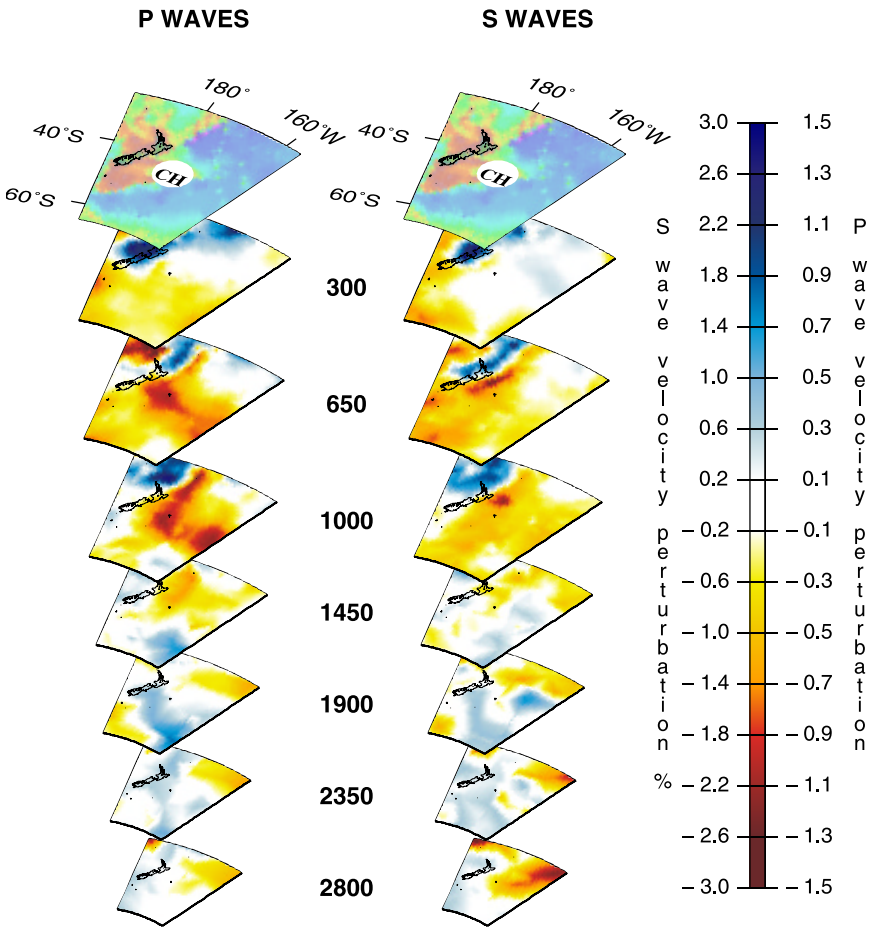

Figure 19. Three-dimensional view of the plumes beneath Chatham in both the (left) *P*-model and (right) *S*-model. Plotting format as in Figure 12a.

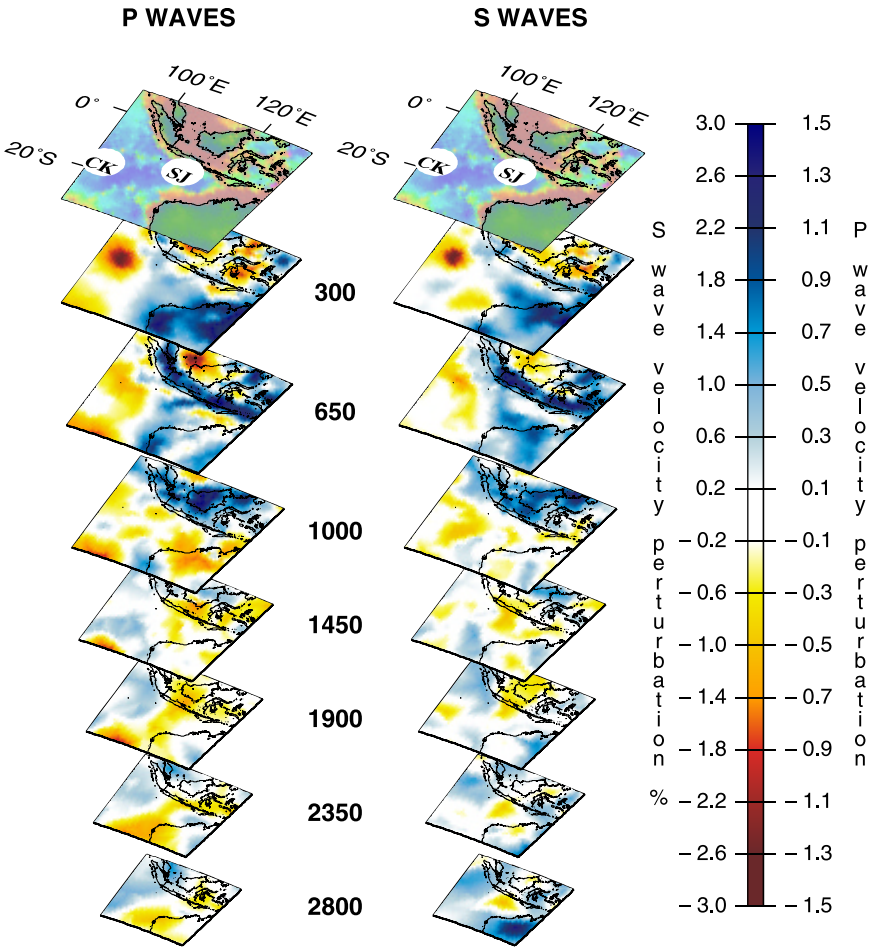

Figure 20. Three-dimensional view of the plumes beneath Cocos/Keeling/South Java in both the (left) *P*-model and (right) *S*-model. Plotting format as in Figure 12a.

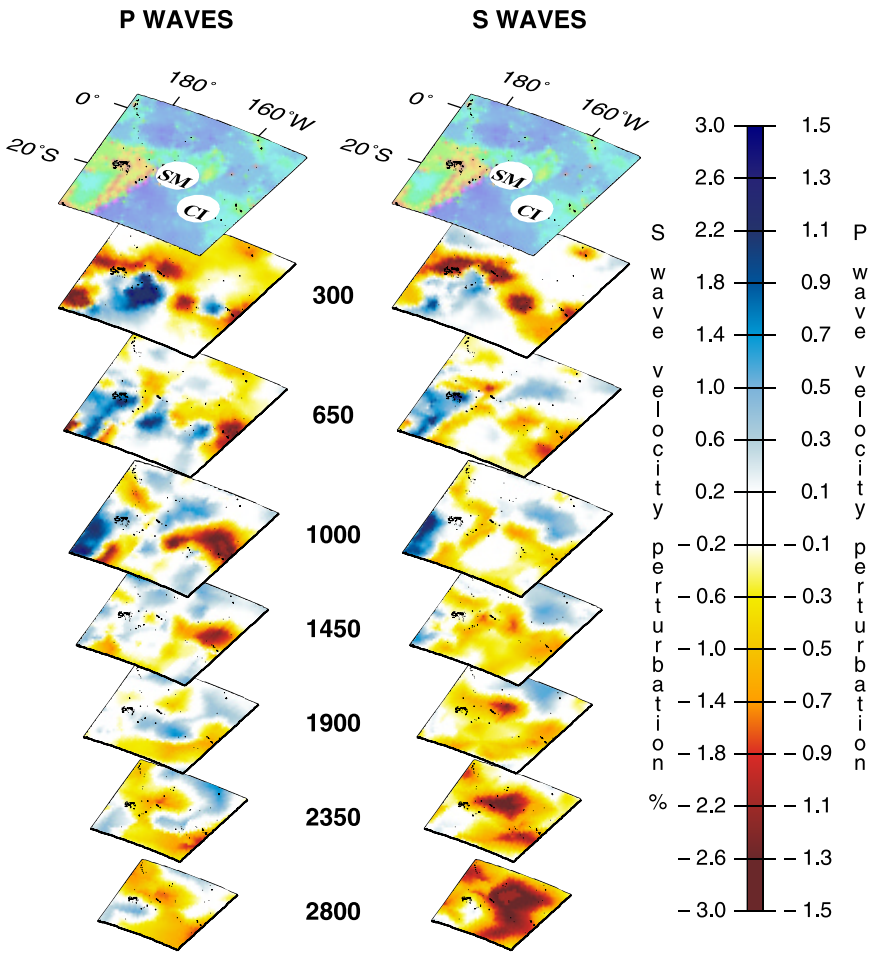

Figure 21. Three-dimensional view of the plumes beneath Samoa and Cook Island in both the (left) *P*-model and (right) *S*-model. Plotting format as in Figure 12a.

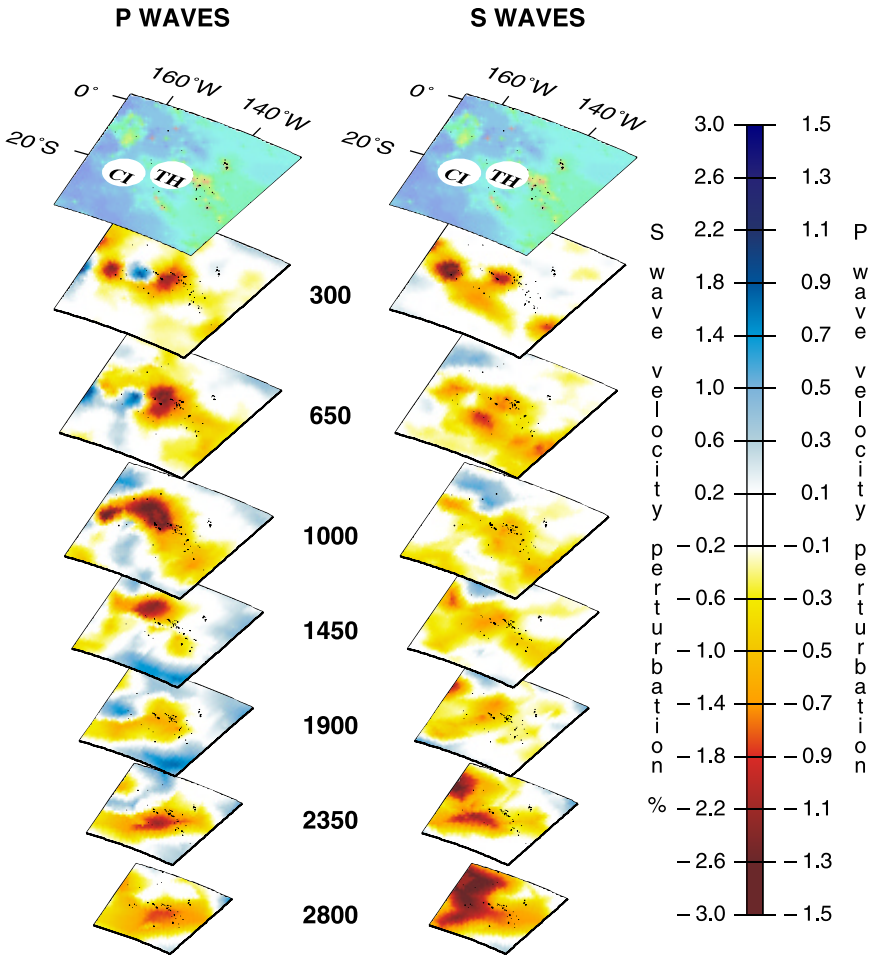

Figure 22. Three-dimensional view of the plumes beneath Cook Island and Tahiti in both the (left) *P*-model and (right) *S*-model. Plotting format as in Figure 12a.

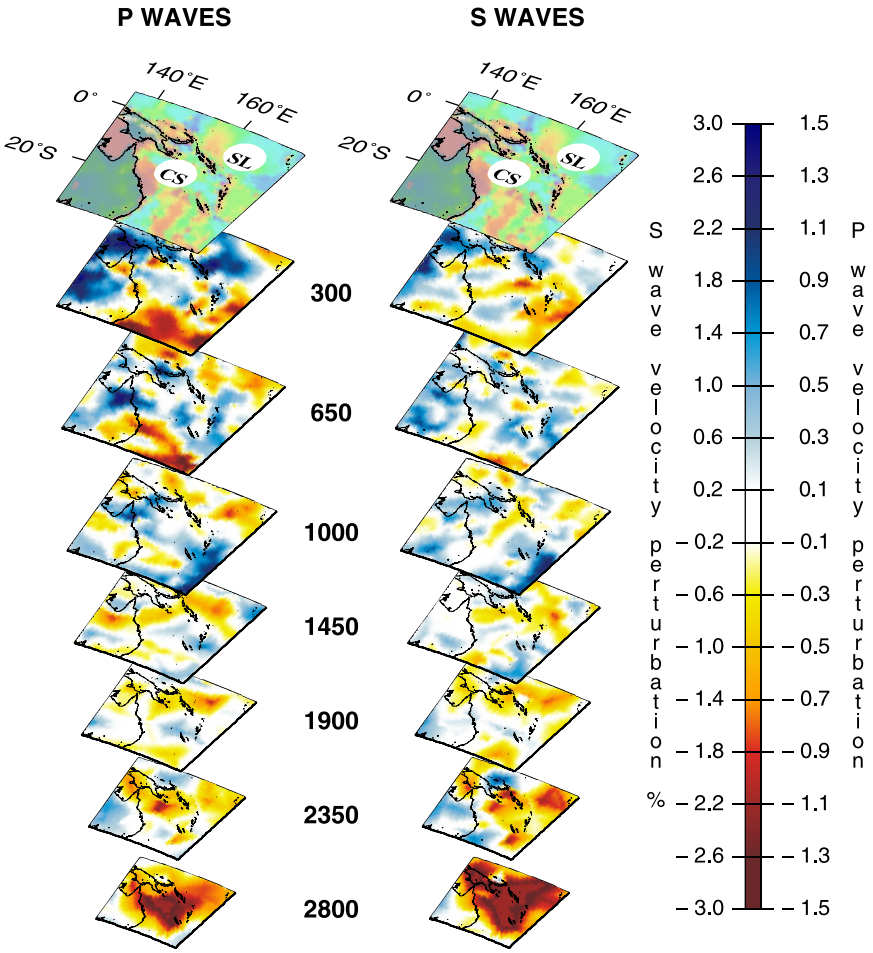

Figure 23. Three-dimensional view of the plumes beneath the Coral Sea and East of Solomon in both the (left) *P*-model and (right) *S*-model. Plotting format as in Figure 12a.

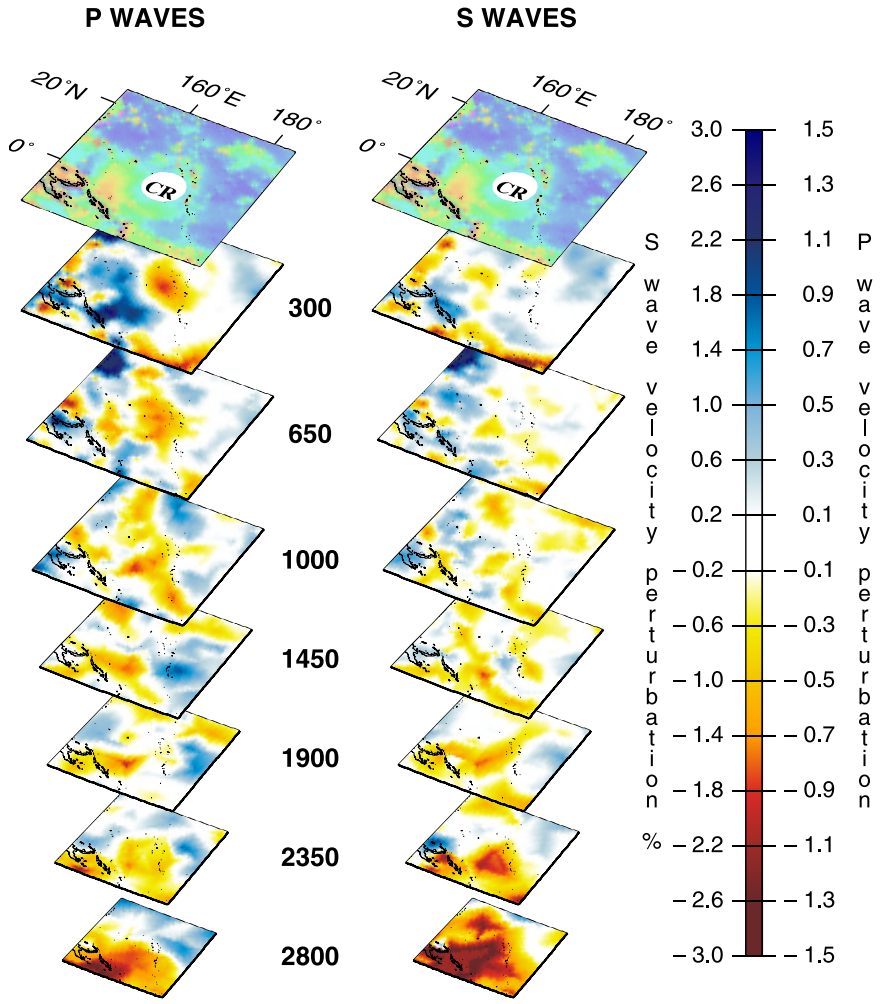

Figure 24. Three-dimensional view of the plumes beneath the Caroline Islands in both the (left) *P*-model and (right) *S*-model. Plotting format as in Figure 12a.

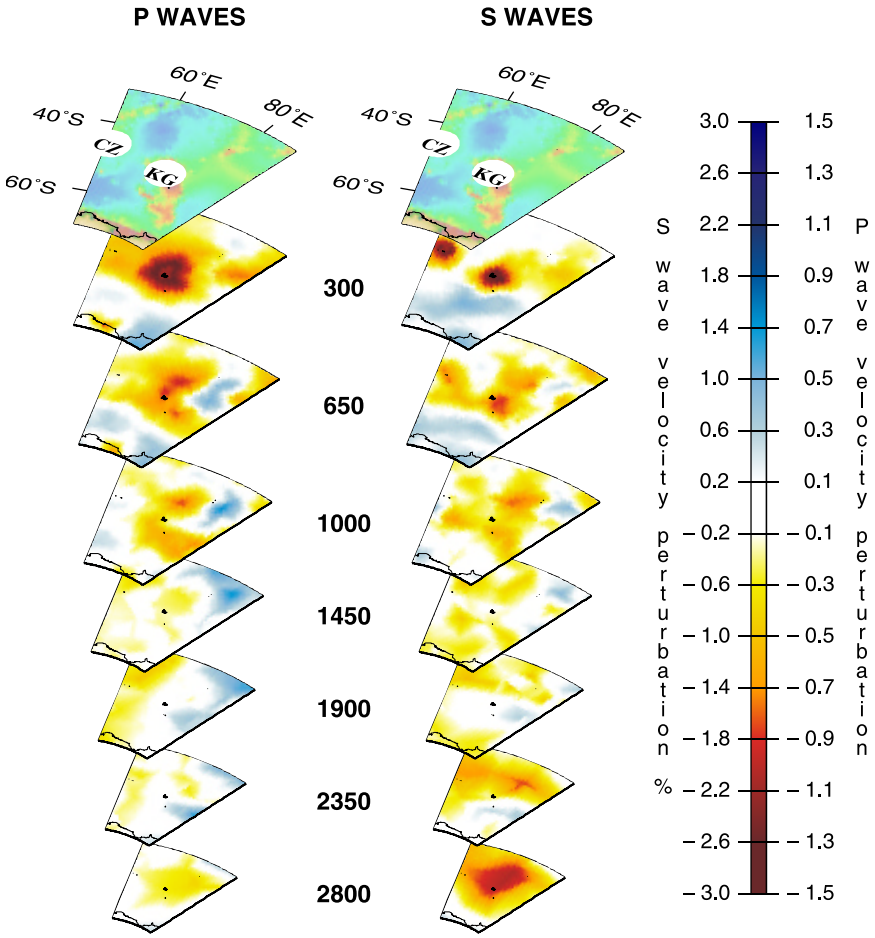

Figure 25. Three-dimensional view of the plumes beneath Crozet and Kerguelen. Plotting format as in Figure 12a.

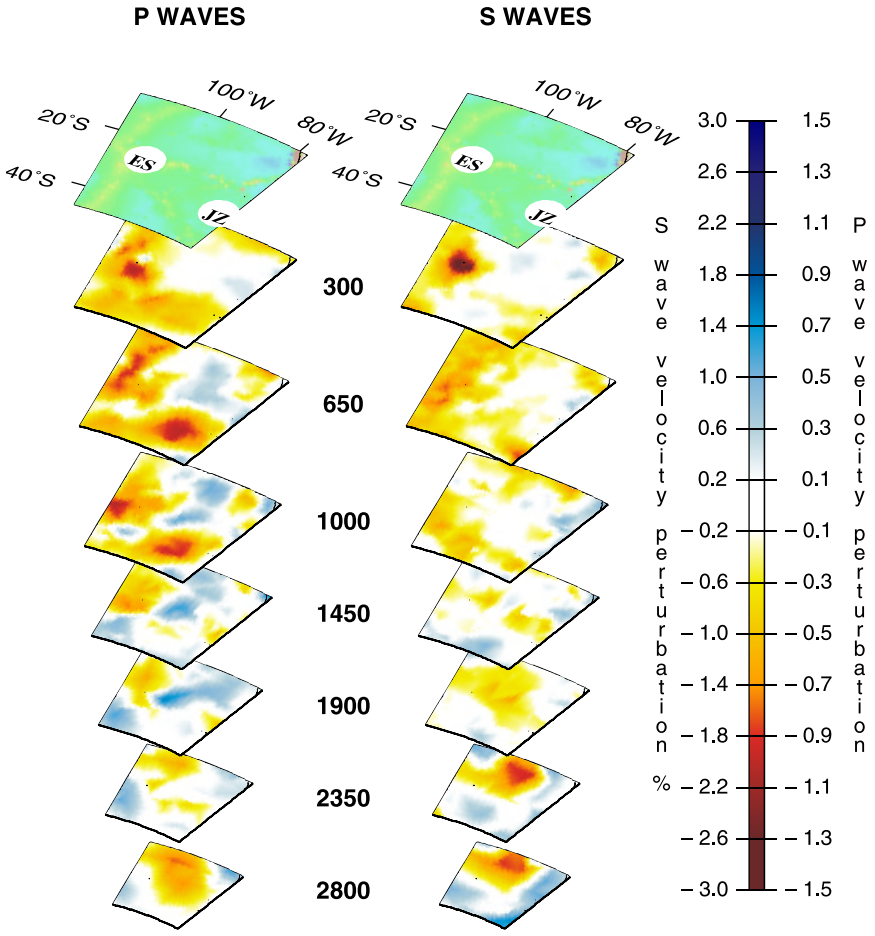

Figure 26. Three-dimensional view of the plumes beneath Easter and Juan Fernandez. Plotting format as in Figure 12a.

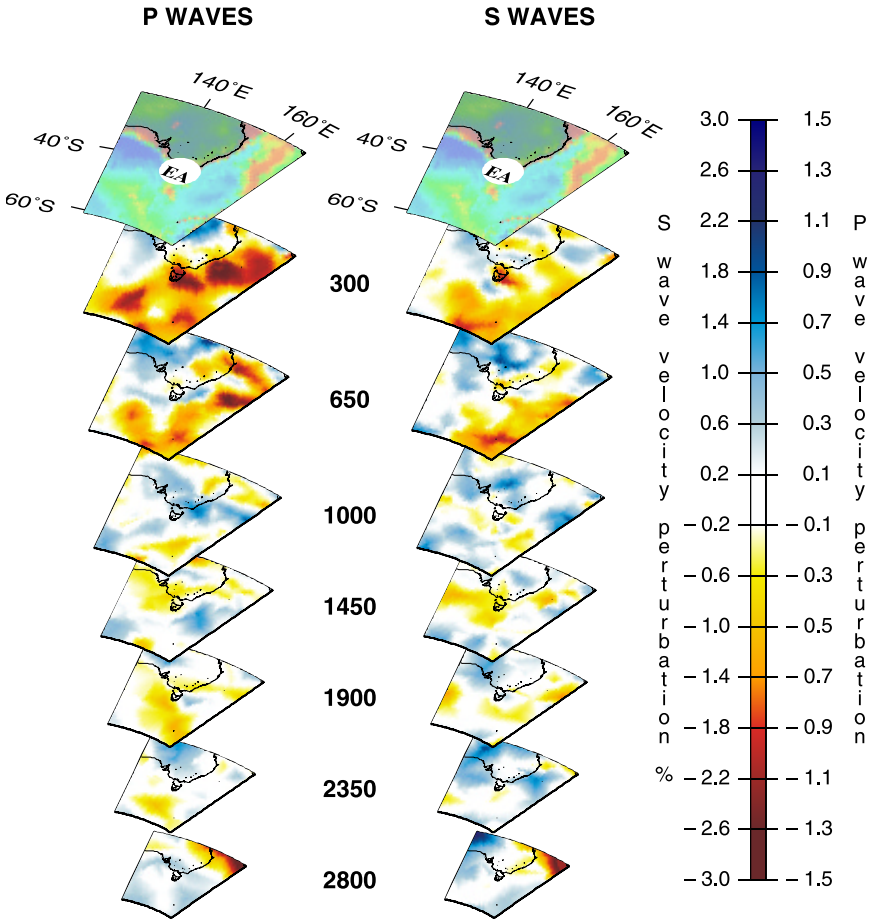

Figure 27. Three-dimensional view of the plumes beneath Eastern Australia. Plotting format as in Figure 12a.

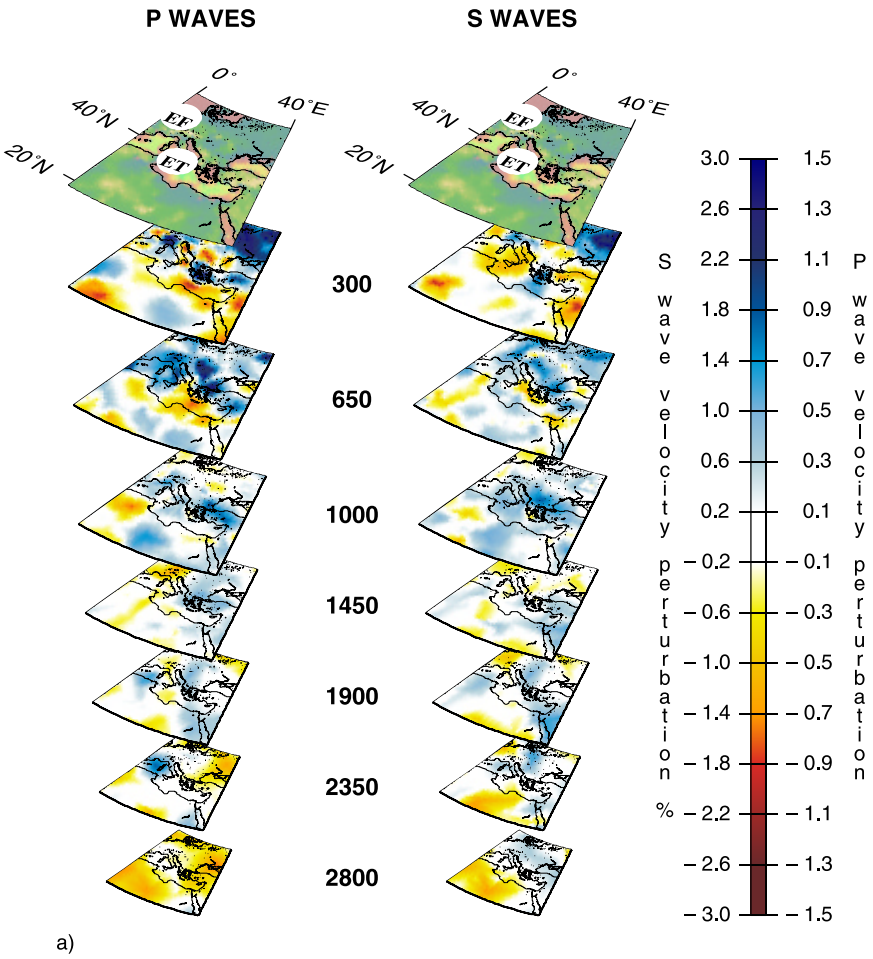

Figure 28. (a) Three-dimensional view of the plumes beneath EF (Eifel) and ET (Etna) in both the (left) *P*-model and (right) *S*-model. Plotting format as in Figure 12a. (b) Same cross sections of the *S*-wave velocity model of Figure 28a (right) on a horizontal plane. (c) Reconstructed synthetic plume confined in the upper mantle (Figure 11a). (d) Reconstructed synthetic plumes extending down to 2800 km depth (Figure 11b) for a resolution test beneath Eifel and Etna.

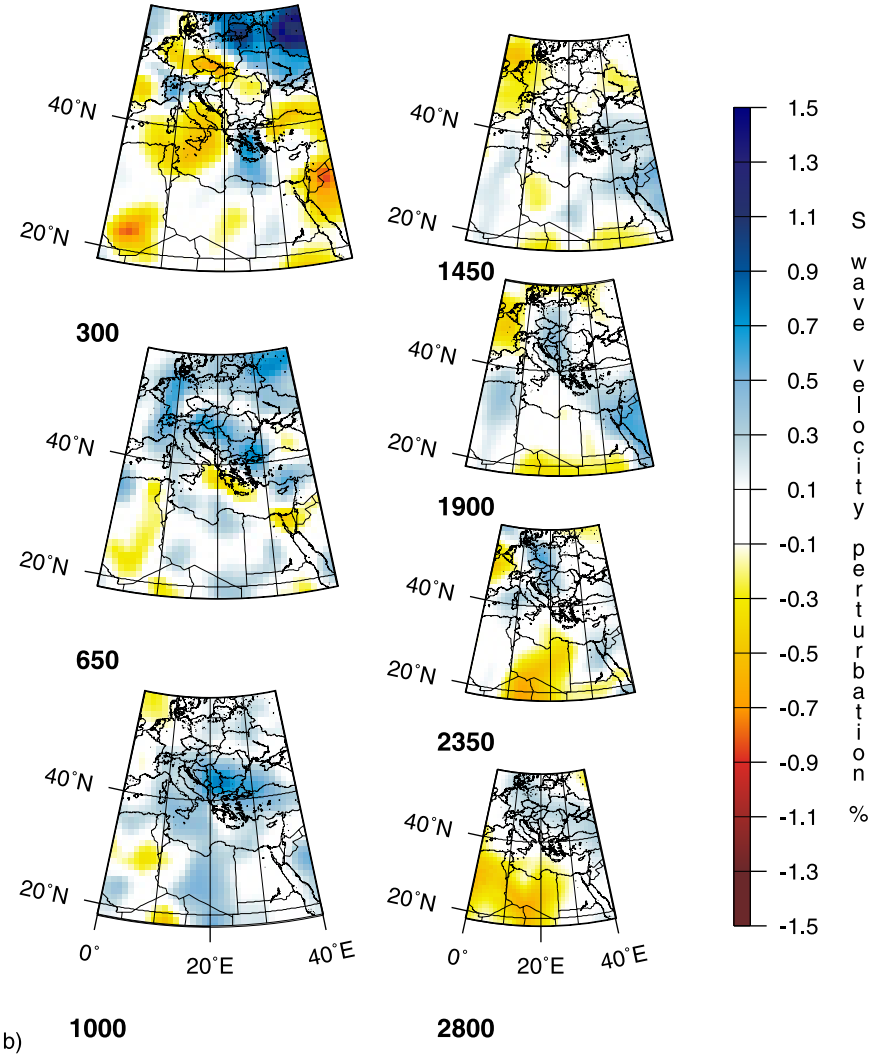

Figure 28. (continued)

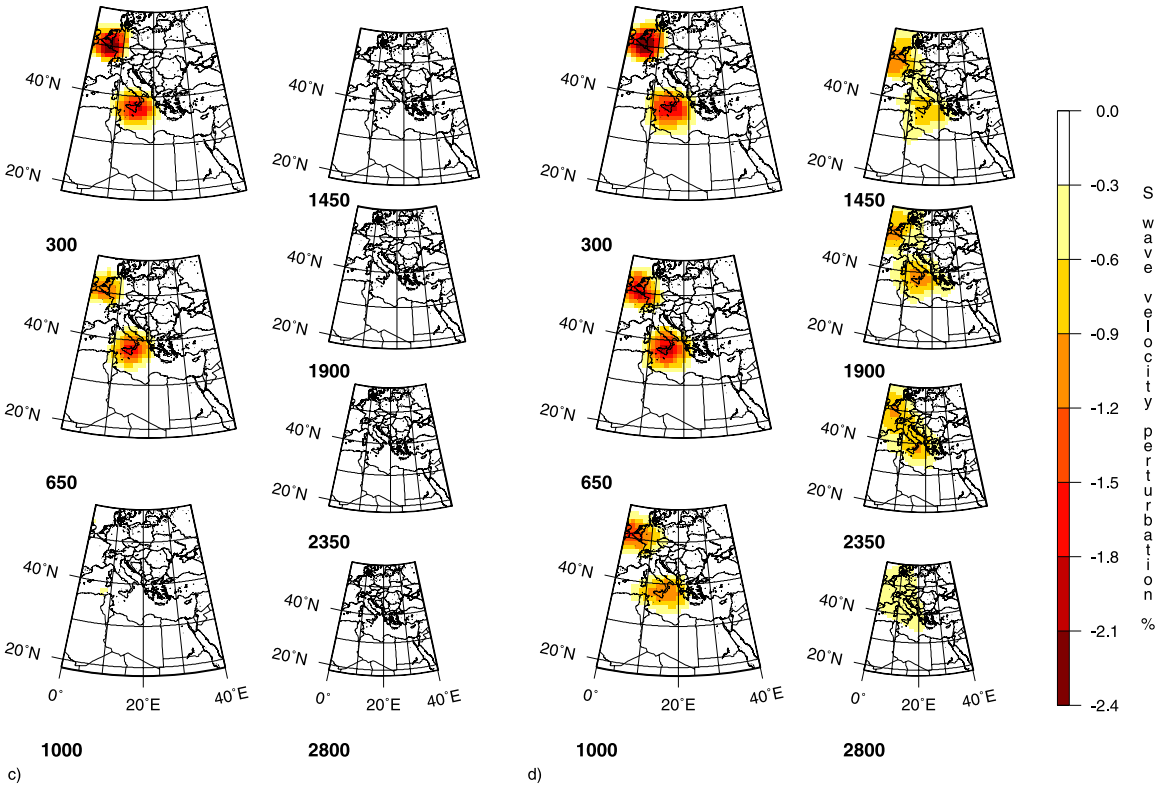

Figure 28. (continued)

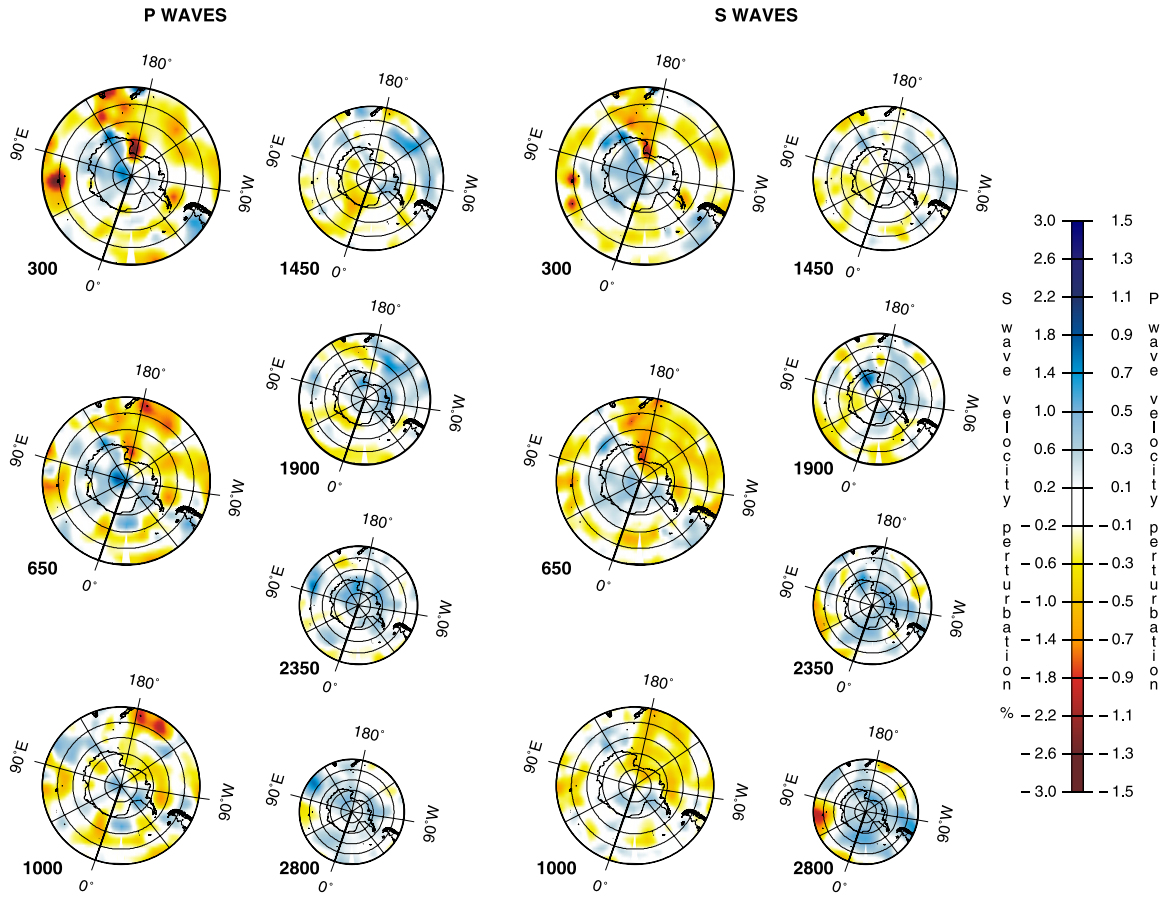

Figure 29. Three-dimensional view of the plumes beneath Erebus in both the (left) *P*-model and (right) *S*-model.

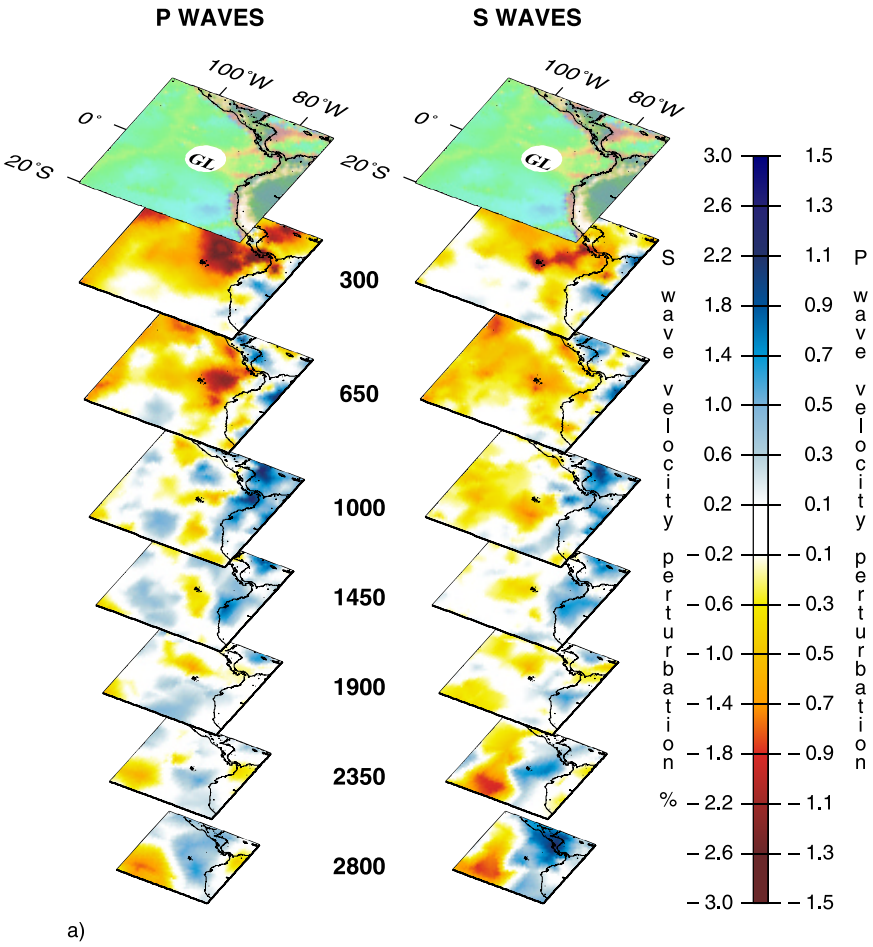

Figure 30. (a) Three-dimensional view of the plumes beneath Galapagos in both the (left) *P*-model and (right) *S*-model. Plotting format as in Figure 12a. (b) Same cross sections of the *S*-wave velocity model of Figure 30a (right) on a horizontal plane. (c) Reconstructed synthetic plume confined in the upper mantle (Figure 11a). (d) Reconstructed synthetic plumes extending down to 2800 km depth (Figure 11b) for a resolution test beneath Galapagos.

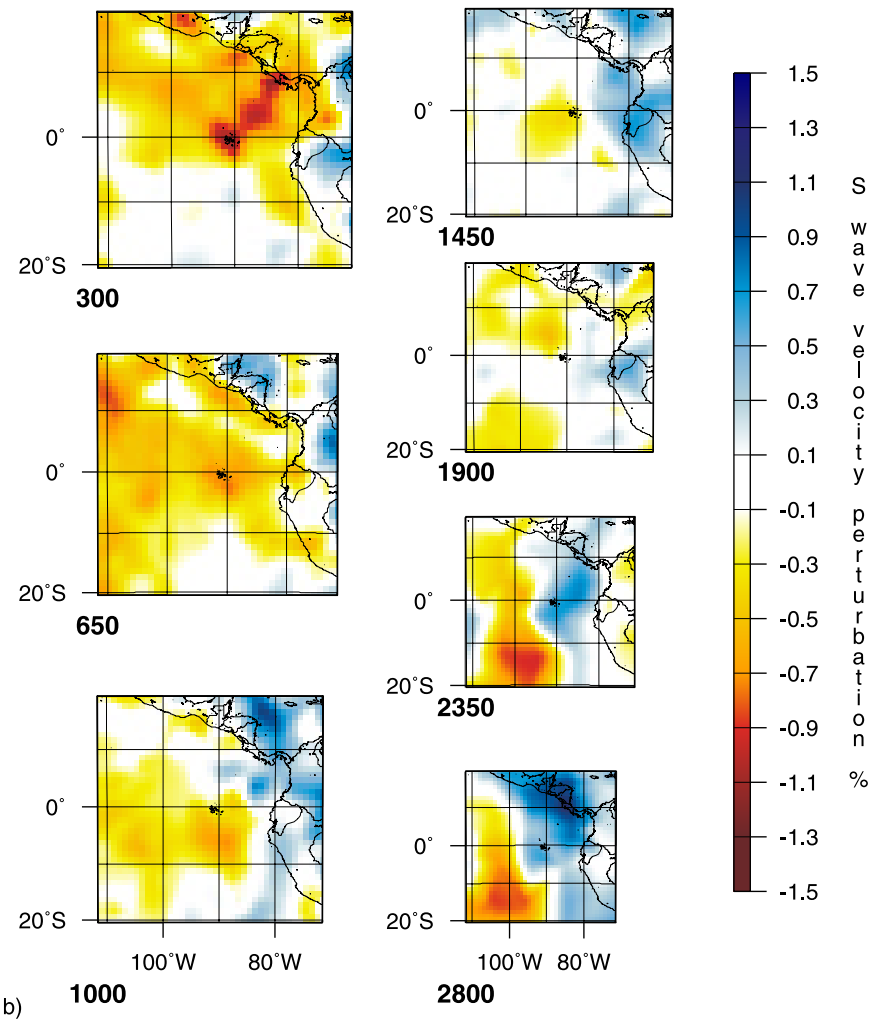

Figure 30. (continued)

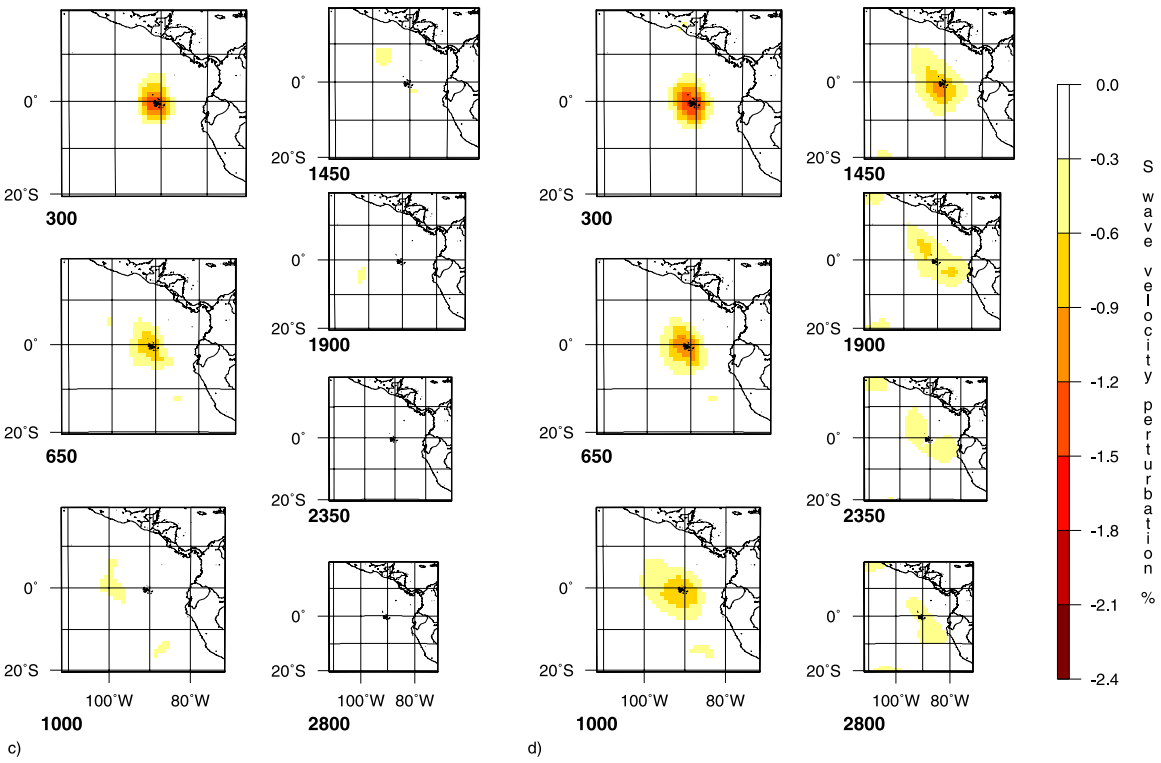

Figure 30. (continued)

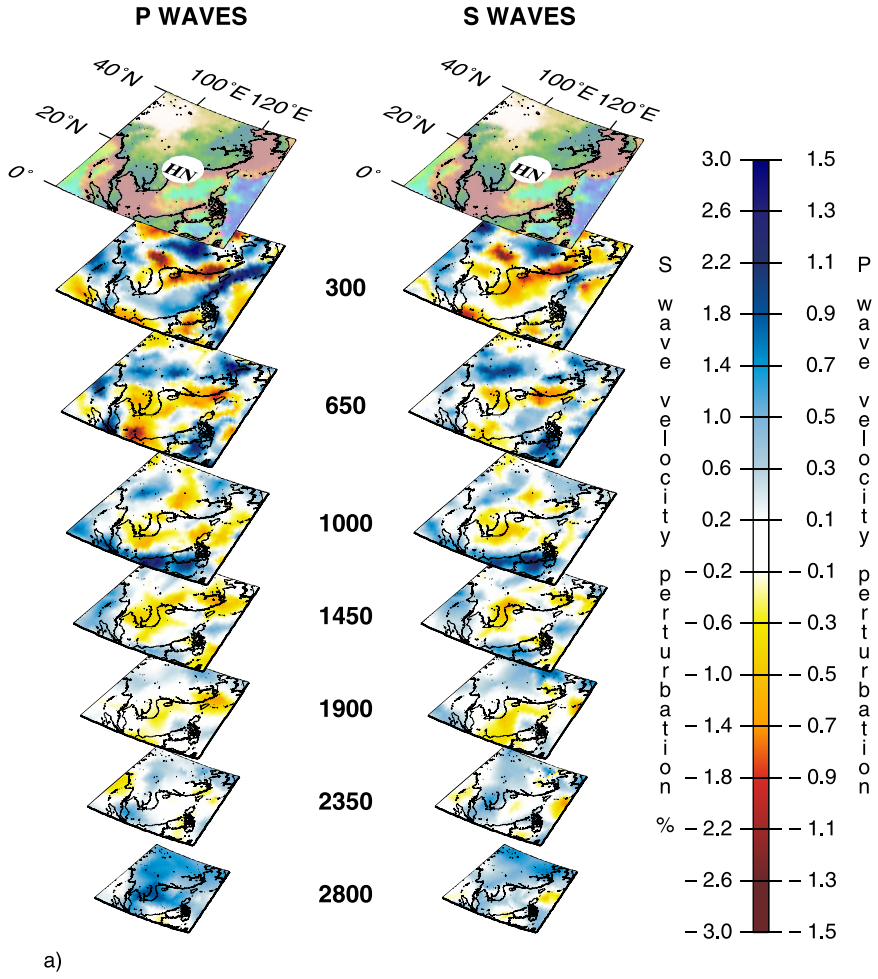

Figure 31. (a) Three-dimensional view of the plumes beneath Hainan in both the (left) *P*-model and (right) *S*-model. Plotting format as in Figure 12. (b) Same cross sections of the *S*-wave velocity model of Figure 31a (right) on a horizontal plane. (c) Reconstructed synthetic plume confined in the upper mantle (Figure 11a). (d) Reconstructed synthetic plumes extending down to 2800 km depth (Figure 11b) for a resolution test beneath Hainan.

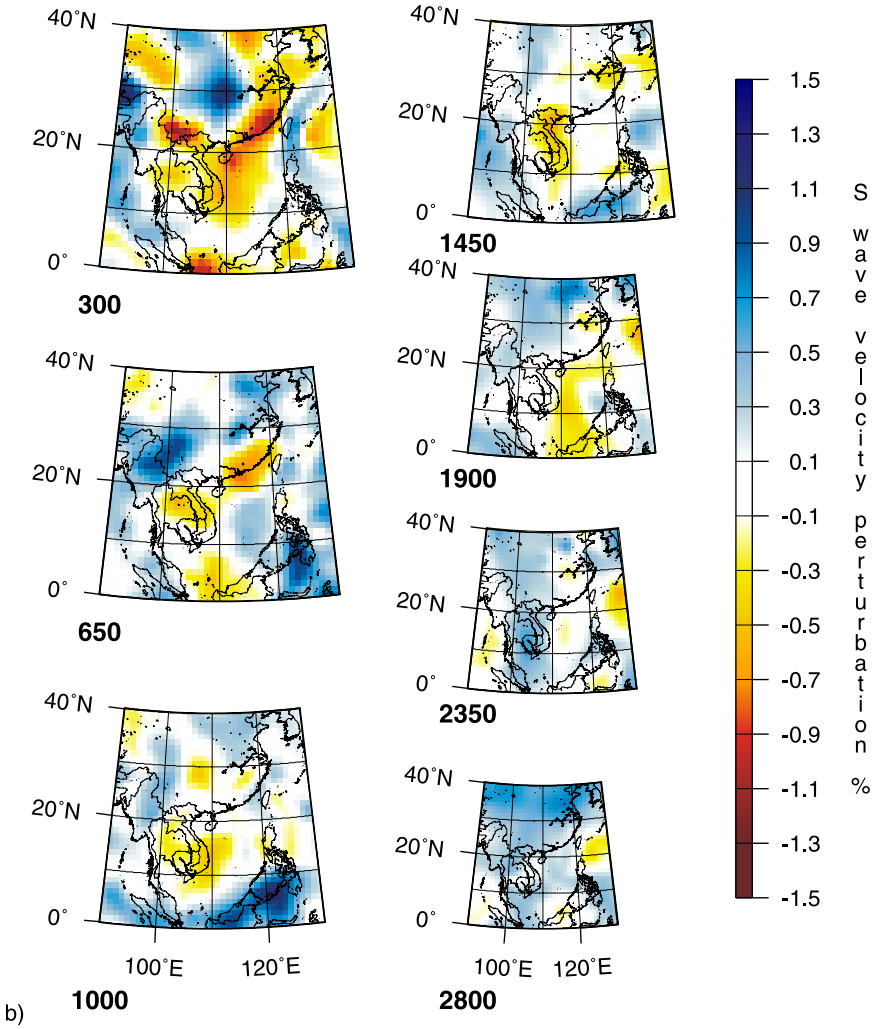

Figure 31. (continued)

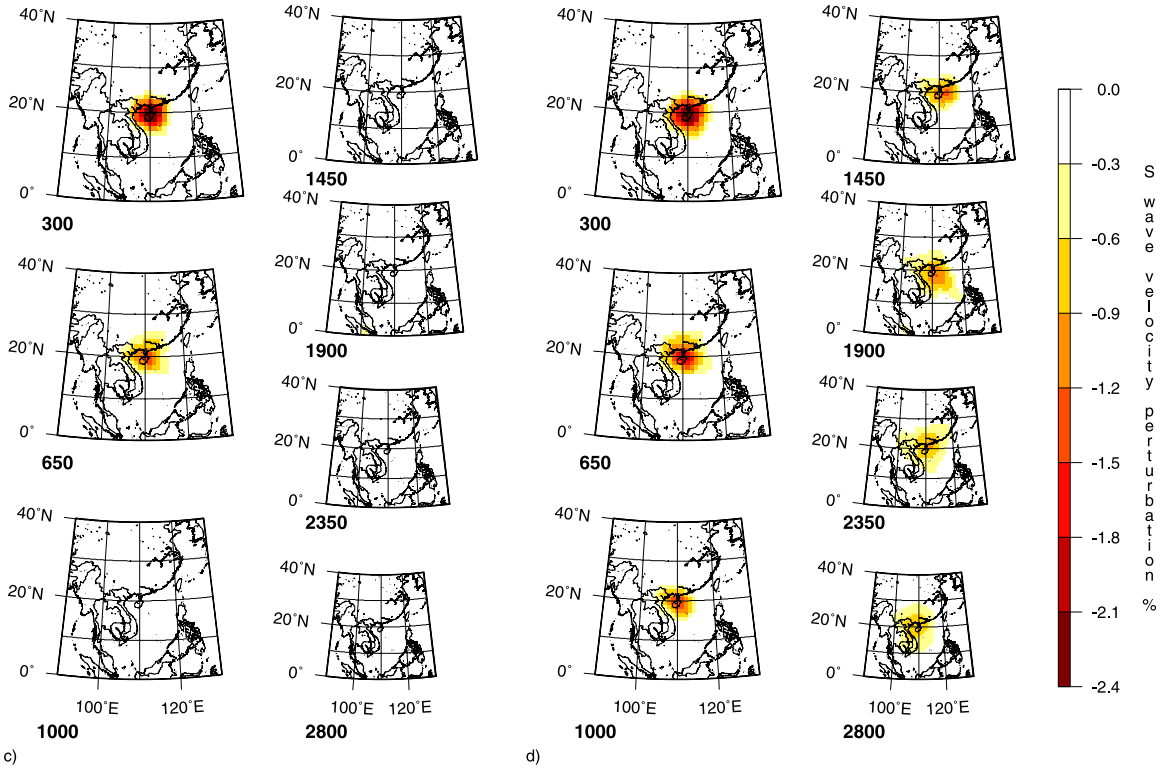

Figure 31. (continued)

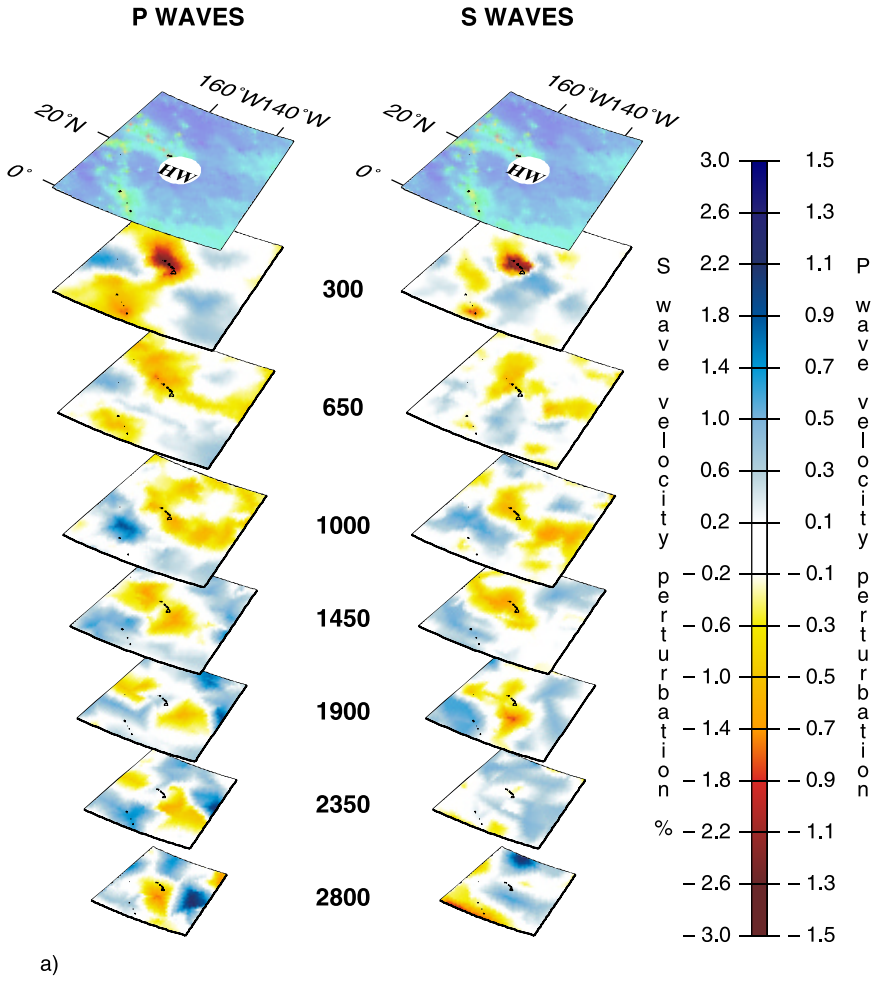

Figure 32. (a) Three-dimensional view of the plumes beneath Hawaii in both the (left) *P*-model and (right) *S*-model. Plotting format as in Figure 12a. (b) Same cross sections of the *S*-wave velocity model of Figure 32a (right) on a horizontal plane. (c) Reconstructed synthetic plume confined in the upper mantle (Figure 11a). (d) Reconstructed synthetic plumes extending down to 2800 km depth (Figure 11b) for a resolution test beneath Hawaii.

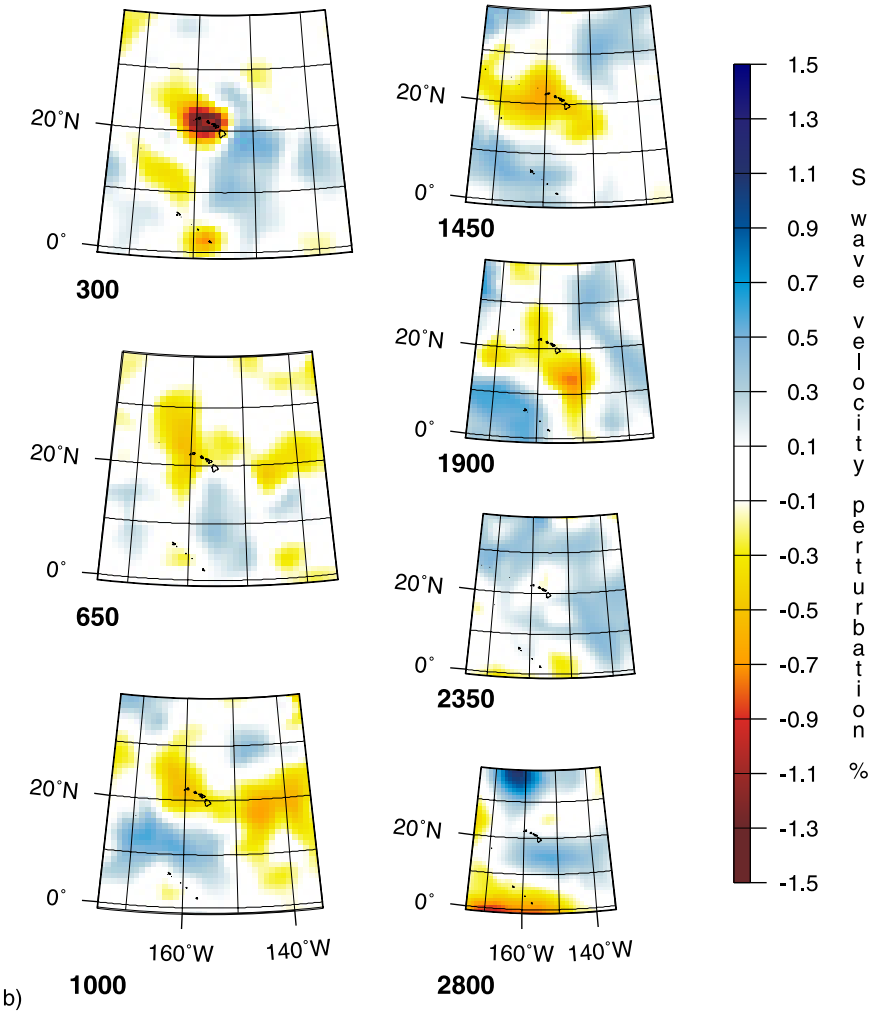

Figure 32. (continued)

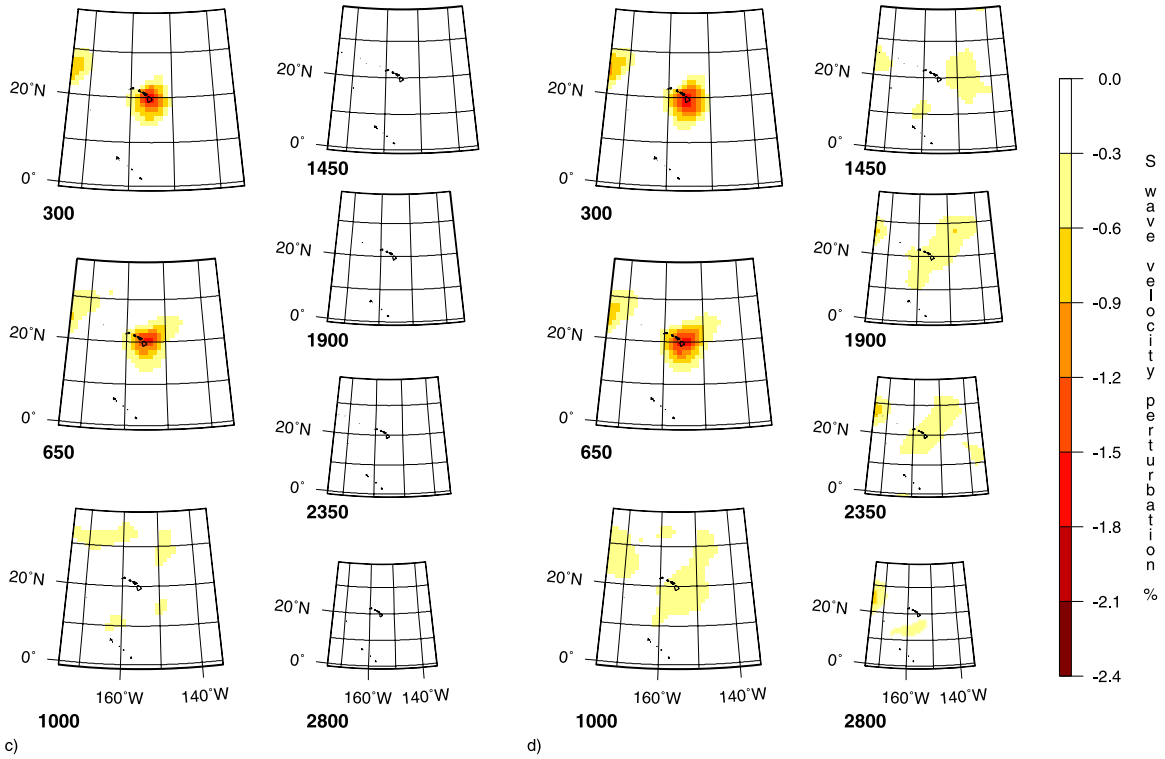

Figure 32. (continued)

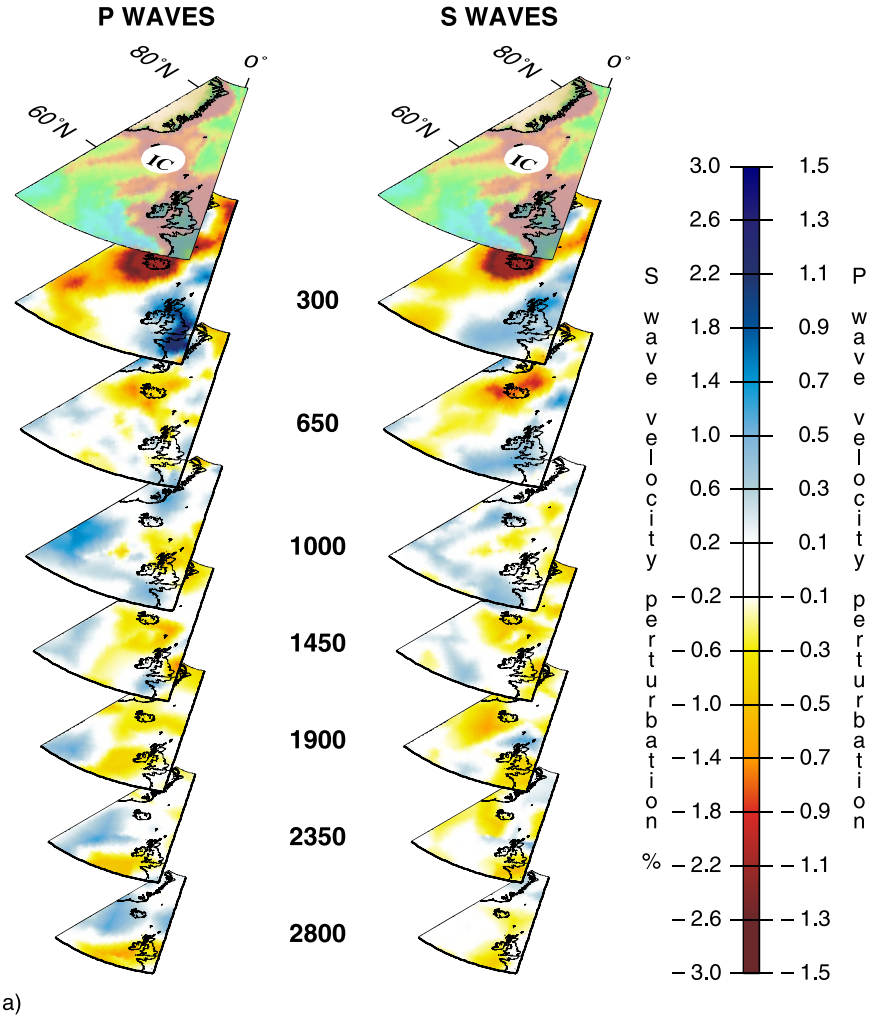

Figure 33. (a) Three-dimensional view of the plumes beneath Iceland in both the (left) *P*-model and (right) *S*-model. Plotting format as in Figure 12a. (b) Same cross sections of the *S*-wave velocity model of Figure 33a (right) on a horizontal plane. (c) Reconstructed synthetic plume confined in the upper mantle (Figure 11a). (d) Reconstructed synthetic plumes extending down to 2800 km depth (Figure 11b) for a resolution test beneath Iceland.

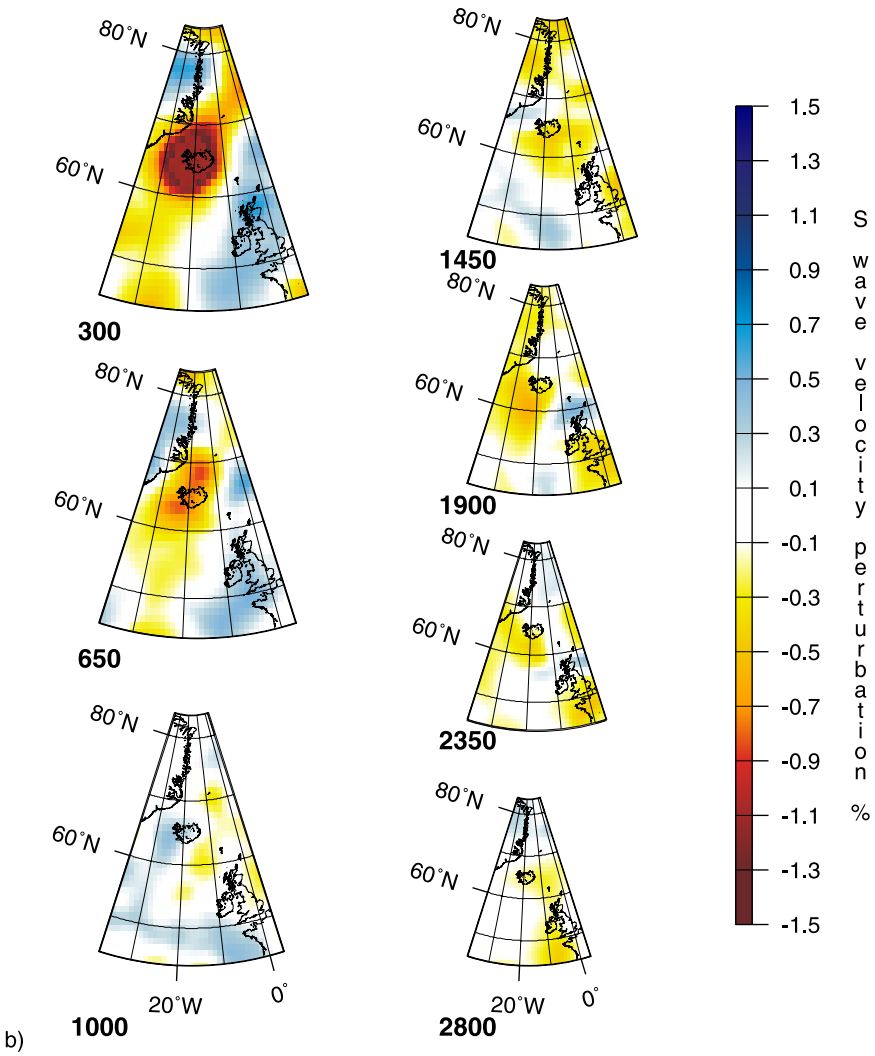

Figure 33. (continued)

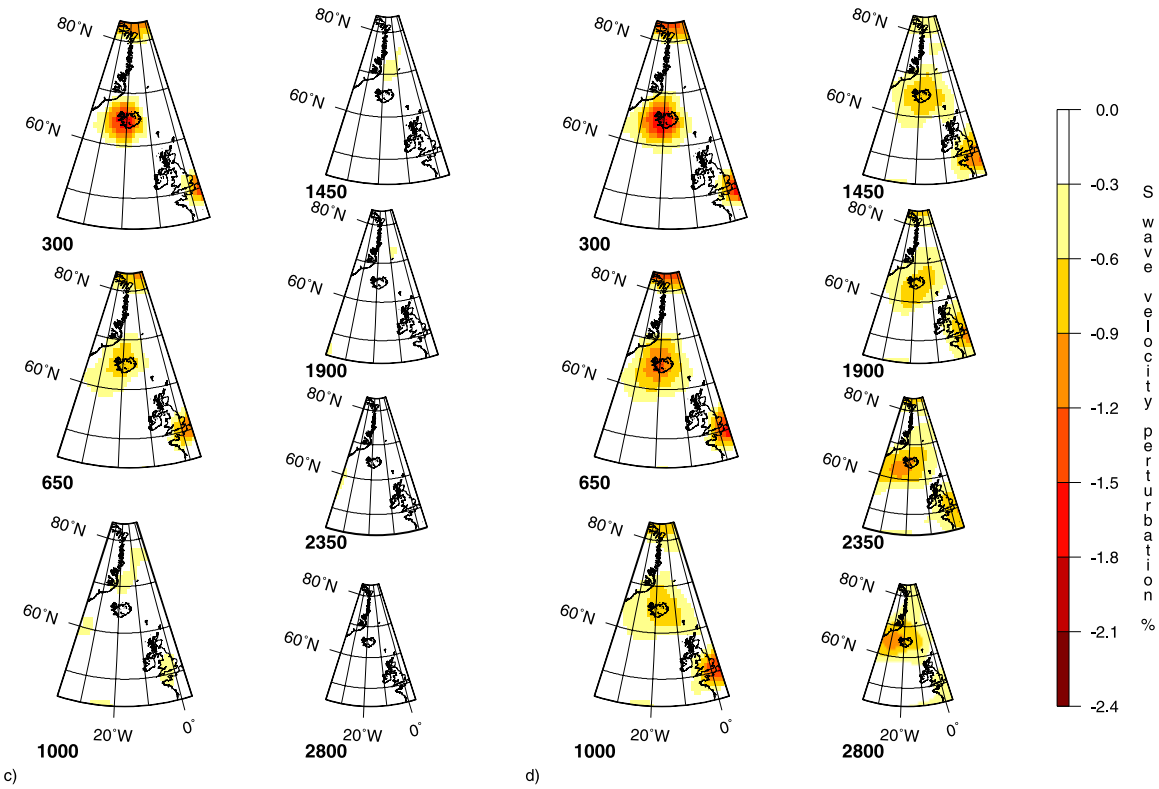

Figure 33. (continued)

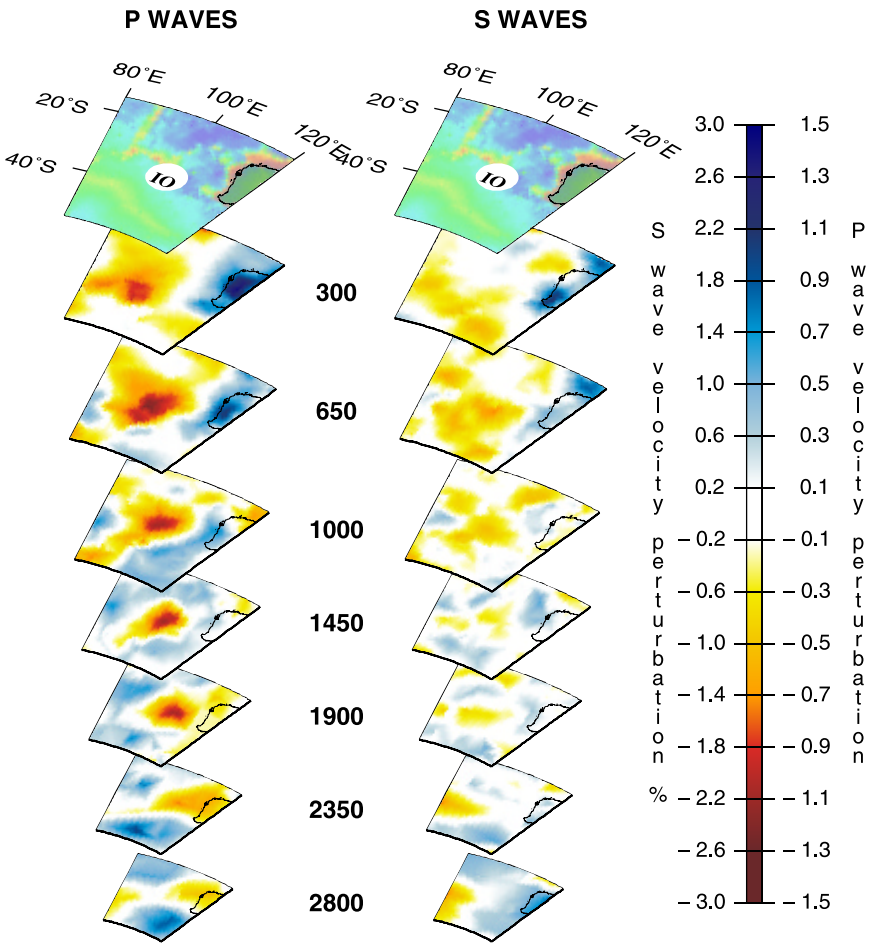

Figure 34. Three-dimensional view of the plumes beneath the Indian Ocean. Plotting format as in Figure 12a.

absence of clear plume heads is especially surprising for the starting plumes that have not yet reached the surface, observed beneath the Coral Sea, East of Solomon and South of Java (though each of these has resolution weaknesses, we consider it unlikely that these are all artifacts in both *PRI-P05* and *PRI-S05*). Because of the supposed size, heads should definitely show up in the tomography if the "tail" does, so we interpret this as an absence, at least at present, of clear plume head structures in the lower mantle (plume heads in the upper mantle would not be resolved in this study that lacks local phases and surface waves). From extensive resolution analysis, we conclude that most plumes in *PRI-P05* and *PRI-S05* would not be visible if their radii were smaller than about 300 km. Given this minimum width for the tails, the ratio of head to tail found in typical laboratory experiments and in numerical modeling would imply that heads with diameters of the order of 1000 km or more and be clearly detectable.

[55] More recent research has indicated that plume heads are not a necessary feature for all starting plumes, and the observed absence may have important geodynamical implications. Laboratory as well as numerical experiments have shown that plumes show a very large head followed by a very thin tail (balloon or cavity plumes) if the plume is much less viscous than the ambient fluid [*Whitehead and Luther*, 1975; *Olson and Singer*, 1985; *Griffiths*, 1986; *Griffiths and Campbell*, 1990; *Kellogg and King*, 1997]. Diapir-shaped plumes are possible when the plume viscosity is approximately equal to the ambient-fluid viscosity [*Olson and Singer*, 1985; *Kellogg and King*, 1997] or significantly larger [*Olson and Singer*, 1985; *Davaille et al.*, 2003; *Korenaga*, 2005]. Spouts are possible in an incompressible fluid whose viscosity is either constant or only weakly dependent upon temperature [*Kellogg and King*, 1997]. Diapiric plumes have a more cylindrical shape than cavity plumes. As they grow, they may develop a mushroom-shaped cap at

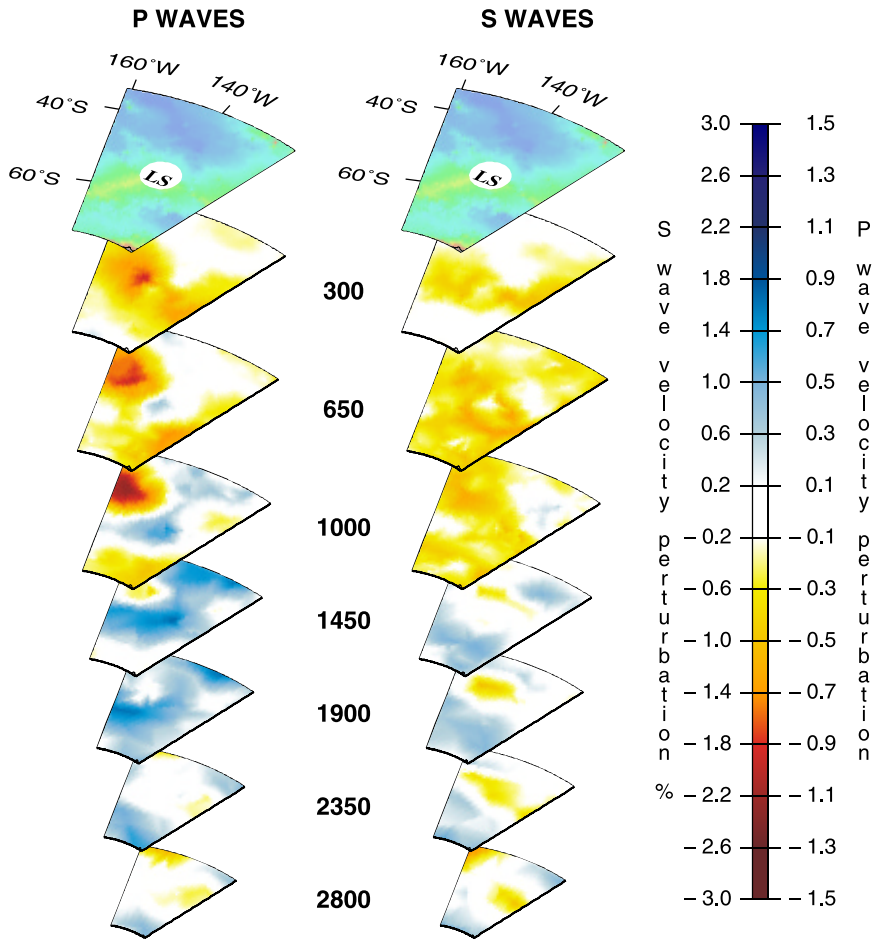

Figure 35. Three-dimensional view of the plumes beneath Louisville. Plotting format as in Figure 12a.

their end whose size is relatively small with respect to their tail [*Griffiths*, 1986; *Kellogg and King*, 1997]. An alternative explanation would be that diapiric plumes develop a head at a much later stage in their life, well above the source boundary layer [*Olson and Singer*, 1985; *Davaille et al.*, 2003]. Broad, completely headless plumes have also been observed in recent numerical models incorporating either pressure-dependent expansivity [*Thomson and Tackley*, 1998] or compositional buoyancy variations [*Farnetani and Samuel*, 2005]. Plume heads are commonly considered to be responsible for the formation of flood basalts (although alternative explanations for their formation have been also suggested [*King and Anderson*, 1995]), whereas the tails are considered to be responsible for the characteristic linear chain of volcanoes associated with hot spots. *Nolet et al.* [2006b] attempt to explain the occurrence of flood basalts in the absence of plume heads by an increased rise velocity of starting plumes, which may be chemically more buoyant since they tap into the top, less dense, layer of an iron-rich source layer.

[56] The large observed radii of the plumes have important consequence for geodynamics. It shows that the plumes play an important role in the mass exchange between upper and lower mantle. Even small upward flow velocities of such large-radius plumes give rise to a substantial advective heat flux. In fact, in order to produce reasonable mass and heat fluxes, the rise of the plumes must be slowed down by a high viscosity or by a chemical anomaly involving a heavy element such as iron, or possibly both [*Nolet et al.*, 2006a]. A high viscosity is in agreement with the observation that plume heads do not develop.

[57] Thus the tomographic images indicate that plumes rise as dome-like structures, slowly work their way to the surface and bend under the effect of the "mantle wind," as seen for instance for the plumes beneath Azores, Canary and Cape Verde, which bend westward from a common core-mantle

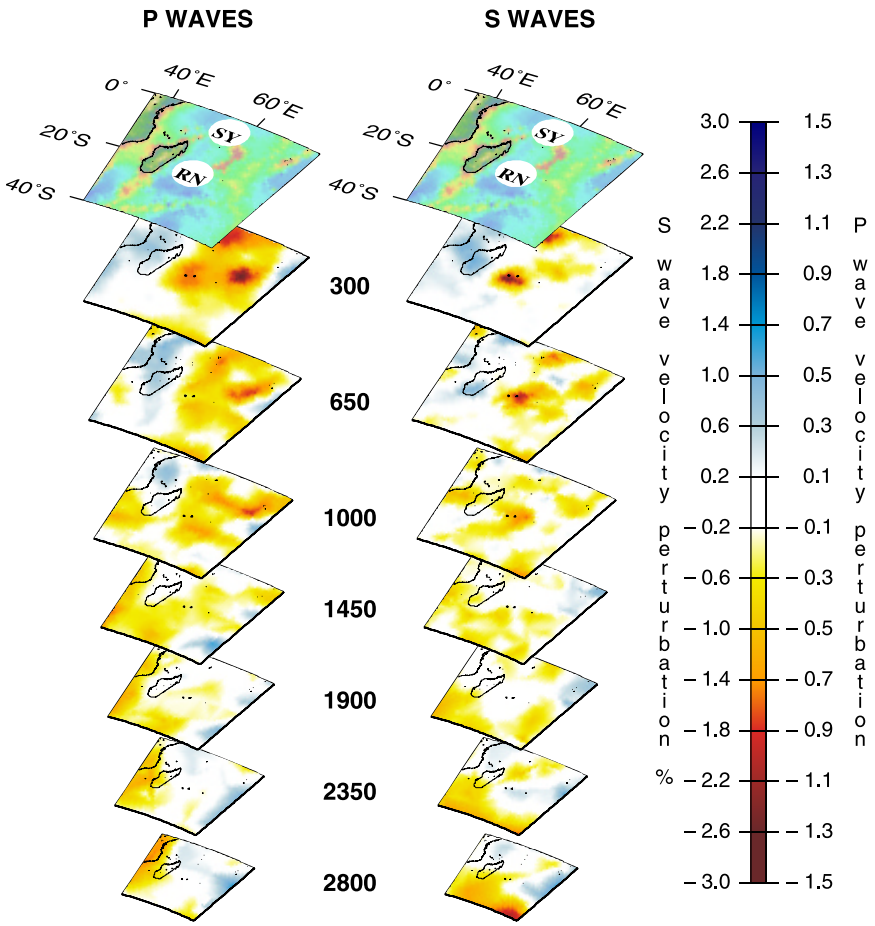

Figure 36. Three-dimensional view of the plumes beneath Reunion/Seychelles. Plotting format as in Figure 12a.

boundary source region at about 20°N, a behavior consistent with mantle wind predictions *O'Neill et al.* [2005]. Plumes finally begin to die by losing their tails at depth, as observed for example beneath Hainan.

6. Discussion and Conclusions

[58] Comparison of *PRI-S05* with other global shear-wave mantle models shows that models overall agree, but that the finite-frequency interpretation allows us to push resolution to smaller scale-length anomalies, and in general produces images of plumes with more vertical resolution. With only a few exceptions, plumes in *PRI-S05* and *PRI-P05* show excellent agreement. Well-resolved deep mantle plumes are present beneath Ascension, Azores, Canary, Cape Verde, Cook Island, Crozet, Easter, Kerguelen, Hawaii, Samoa and Tahiti. Resolution is still lacking in the lowermost mantle beneath several hot spots (Afar, Atlantic Ridge, Bouvet(Shona), Cocos/Keeling, Louisville and Reunion) though it is clear that these are not confined to the upper mantle. Mid-mantle plumes are present beneath Bowie, Hainan, Eastern Australia and Juan Fernandez. Unless these plumes are actually deep plumes with very thin tails originating from the D″ region, they do not spawn from a known thermal boundary layer. Eifel, Seychelles, and possibly Etna and Yellowstone cap plumes strictly confined to the upper mantle. Finally, developing plumes are present beneath East of Solomon, the Coral Sea and perhaps South of Java in both *PRI-S05* and *PRI-P05*.

[59] The imaged plumes are wide in the lower mantle, with radii of at least 300–400 km, and do not show the typical head-tail shape associated to plumes. Such broad, headless plumes suggest that the viscosity in the mantle is only weakly dependent upon temperature, and/or that compositional variations act to slow the rise of the plume.

[60] The number of lower mantle plumes visible in the tomographic images is consistent with theoretical considerations and numerical modeling at Rayleigh numbers close to that proposed for the

Earth (10^7). *Zhong* [2005, 2006], for example, expects "tens of plumes" which are considerably wider in the lower mantle than the upper mantle, on the basis of a large number of computational experiments both for a layered and an isochemical Earth.

[61] Several years ago, the plume hypothesis came under significant attack [e.g., *Anderson*, 2000], partly because most of the evidence for plumes was indirect and unambiguous tomographic evidence was lacking. In our view, the tomographic images presented here show that a large number of plumes rise up from the deep mantle. However, the debate concerning plumes has a contentious nature, and doubts about results as presented in this paper and by *Montelli et al.* [2004a] continue to be raised. It should be clear from the resolution analyses presented in the (electronic) appendix of *Montelli et al.* [2004a] and in this paper (and summarized in Table 1) that the evidence is strong despite the lack of good resolution in many regions in the mantle. Nevertheless, we wish to address briefly some commonly raised issues (see *Nolet et al.* [2006a] for more extensive discussion):

[62] (1) The presence of island stations is necessary to image low-velocity anomalies below the island itself unless there is a fortuitously high density of surface reflection points for *PP* or *SS* waves within perhaps 1000 km of the island (though finite-frequency kernels extend well beyond this distance, the area of sensitivity becomes too thin at large distance). The finite-frequency kernels are still narrow at shallow depth and their ability to sense the width of the plume in the uppermost mantle is limited. Thus, even a "blob" of low velocity might smear out over some depth range. The resolution tests show this effect to be limited to a few hundred km. In the lower mantle the sensitivity is too spread out to lead to a narrow plume-like artifact. *Montelli et al.* [2006] show that neglect of finite-frequency effects in crustal corrections may lead to artificial low-velocity anomalies in the upper mantle of the order of -0.3% in v_P for very small islands (20 km diameter), which is not enough to explain the observed plume signals.

[63] (2) One reviewer of this paper questioned the use of a spherically symmetric background model. Indeed, in ray-theoretical inversions, the bending of raypaths has been shown to be of influence on the amplitude (but not the shape) of velocity anomalies [*Bijwaard and Spakman*, 2000]. Because of computational limitations, it would be enormously difficult to test the equivalent effect on finite-frequency inversions, but we expect it to be much smaller since the width of finite-frequency kernels is much larger than the excursions a ray makes due to lateral heterogeneity, making the delay much less sensitive to the exact location of the raypath. In any case, it is difficult to see how ray bending could create plume-like artifacts.

[64] (3) As with every tomography problem, we need to regularize the inversion, i.e., where there is no resolution we bias the model toward a mathematically definable "preferred" solution. We prefer the "smoothest" solution that agrees with the data. Since the smoothing operator is isotropic, there is no directional bias in anomalies, thus no bias toward vertical, "plume-like" anomalies.

[65] (4) Our model has an adaptive grid, with spacing increasing with depth to adapt to the lower resolution. In this way we make the tomographic image less dependent on the regularization, but we limit the theoretically available resolution. This could in principle cause plumes narrower than 600 km in diameter to show up as plumes with the minimum visible radius of 300 km. However, most of the plumes that we imaged would however not be visible if smaller than that (see Table 1; note that the resolution calculations incorporate the effects of coarseness in parameterization). In other words, we see the plumes because they are massive; if they were not, they would not show up.

Appendix A: Differences Between *PRI-P04* and *PRI-P05*

[66] In this appendix we briefly describe the procedure for making crustal corrections and other improvements that led us to update the *P*-wave model of *Montelli et al.* [2004a]. New and old models are designated by *PRI-P05* and *PRI-P04*, respectively.

[67] *Montelli et al.* [2004b] used a reference model close to *iasp91*, slightly modified in the transition zone to remove a bias in the average *PP-P* travel times. In this paper we compute all the delay times with respect to the original *iasp91* reference model [*Kennett and Engdahl*, 1991]. For the long-period data, *iasp91* predicts a bias of +4 s for *P*, +0.16 s for *PP-P* and +0.14 s for *pP-P*. We apply a constant correction to all *P* traveltimes such that the average $\langle \delta T_P \rangle = 0$, but accept the bias in *PP-P* and *pP-P*. The bias in the arrival times for *P* is due to a bias in the NEIC origin times, which reflect onset of short-period precursive energy rather than the onset of

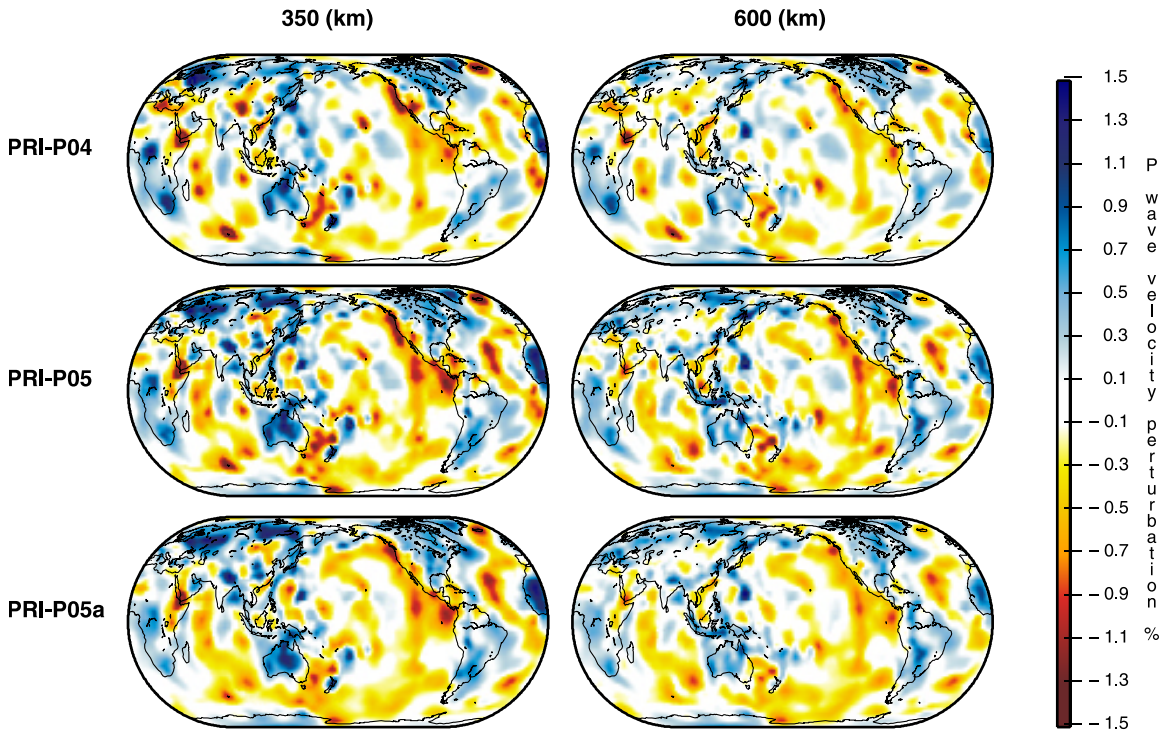

Figure A1. Horizontal cross sections at 350 and 650 km depth in the upper mantle of *PRI-P04*, *PRI-P05*, and *PRI-P05a*. Plotting format and color scale are the same as in the velocity plot in Figures 4–7.

the main rupture with long-period energy. Such bias does not exist for differential travel times *PP-P* and *pP-P*. The bias in these phases is small and the adoption of *iasp91* allows for improved consistency with other (and future) tomographic studies.

[68] Estimates for standard errors in the ISC data were first published by *Morelli and Dziewonski* [1987], who gave a standard deviation $\sigma_P = 1.4$ s for P delays. A more sophisticated analysis by *Gudmundsson et al.* [1990] gave $\sigma_P = 1.0$ s for the distance range we utilize. For *PRI-P04* we lowered this conservatively to $\sigma_P = 0.9$ s in view of the fact that we used only a subset of the data (those listed with two-decimal precision) from the winnowed and relocated set of *Engdahl et al.* [1998]. Motivated by an observed difference in anomaly amplitudes predicted by the ISC data and by the long-period data for the same value of reduced chi-squared, we reconsidered the standard deviations assigned to these data and lowered σ_P for the short-period P further from 0.9 s to 0.7 s. On the other hand, the rather large misfit to the ISC pP data led us to increase the σ for the pP from 1.1 to 1.4 s.

[69] The scaling of the data in the two frequency bands, which are very different in size, is determined by the condition that the reduced chi-squared is equal to one for each frequency: $\chi^2_{LP}/N_{LP} = \chi^2_{ISC}/N_{ISC} \approx 1$, where N_{LP} is the number of long-period data and N_{ISC} the number of short-period data. The least-square system we are minimizing is thus

$$\sum_i \left(\frac{\sum_j A_{ij} x_j - b_i}{\sigma_i} \right)^2_{LP} + \frac{1}{f^2} \sum_i \left(\frac{\sum_j A_{ij} x_j - b_i}{\sigma_i} \right)^2_{ISC} + \epsilon_c \| \boldsymbol{x}_c \|^2 + \epsilon_h \| \boldsymbol{x}_h \|^2 + \epsilon_S \| \boldsymbol{S} \boldsymbol{x}_c \|^2 = \text{minimum}, \tag{A1}$$

where A is the matrix of the tomographic inversion, and $\boldsymbol{x}$ is a vector with model values $\boldsymbol{x}_c$ and origin time and hypocentral corrections $\boldsymbol{x}_h$. The scaling factor $f = N_{ISC}/N_{LP}$ where N_{ISC} is the total number of short-period data and N_{LP} is the total number of long-period data. The quantity ϵ_c is the damping factor for the model norm, ϵ_h is the damping factor for the hypocentral parameters, and ϵ_S and S are the smoothing factor and smoothing operator as used by *Montelli et al.* [2004a]. In the work by *Montelli et al.* [2004a], 118 short-period pP without corresponding P delays were merely contributing extra unknowns, and were removed in the current inversion. For the remaining pP data, we let the depth of the hypocenter freely move by setting the corresponding damping factor $\epsilon_h = 0$.

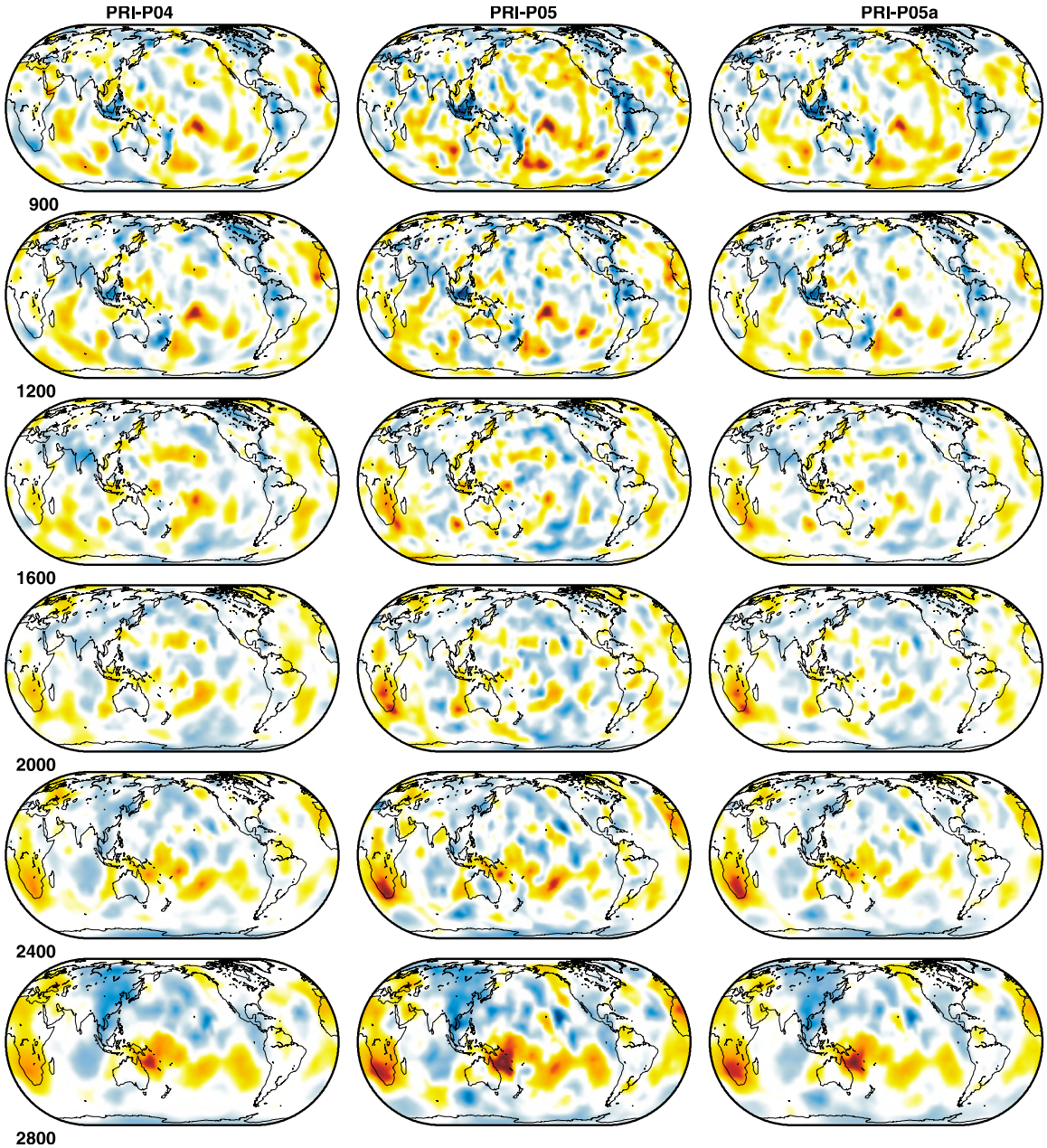

Figure A2. Horizontal cross sections at 900, 1200, 1600, 2000, 2400, and 2800 km depths in the lower mantle of *PRI-P04*, *PRI-P05*, and *PRI-P05a*. Plotting format and color scale are the same as in the velocity plot in Figures 4–7.

[70] The theoretical times are corrected for ellipticity and for the effect of the crust. Crustal corrections are computed using the 2° × 2° global crustal model CRUST2.0 (model available through the Rem Web site: http://mahi.ucsd.edu/Gabi/rem.html) as follows:

$$\delta T_{crust} = T_{CRUST2.0} - T_{iasp91} = \left(\sum_j \frac{h_j * \cos\theta_j}{c_j}\right)_{CRUST2.0} - \left(\sum_k \frac{h_k * \cos\theta_k}{c_k}\right)_{iasp91}, \quad \text{(A2)}$$

where θ is the incident angle, h_j the thickness of the j-th crustal layer, and c_j is the velocity within the j-th crustal layer. For station and bounce point corrections, we sum from the top layer down to the Moho depth defined either by CRUST2.0 or *iasp91*, whichever is deeper. The 2° × 2° average elevation of the CRUST2.0 at the station is lifted above sealevel and this is subtracted from the station elevation. In the case that the Moho in CRUST2.0 is above the *iasp91* Moho, we correct for the fact that part of the crust in *iasp91* actually mantle in CRUST2.0. For the *pP* source correction we sum from the top layer down to the source depth. For every other source correction we sum from the Moho depth up to the source depth. The traveltime delays are then computed as follows:

$$\delta T = \left(T^{obs} - T^{iasp91}\right) - \delta T_{ellip} - \delta T^{STA}_{crust} - \delta T^{STA}_{elev} - \delta T^{SRC}_{crust} - \delta T^{BP}_{crust} \quad \text{(A3)}$$

where *STA* denotes the station correction, *SRC* is the source correction and *BP* is the bounce point correction, if present. With the exception of *pP*, the source correction is only applied in the case that the source is located within the CRUST2.0 or within the *iasp91* crust, whichever extends deeper. We assume that the ray traversing the crust is fully within the 2° × 2° cell of CRUST2.0 in which the station or the source or the bounce point is located. This might lead to small inaccuracies for stations, sources or bounce points located at the edge of the cell and for which incoming and/or outgoing rays are mainly crossing the neighboring CRUST2.0 cell. For differential traveltimes, such as *PP-P*, we correct both phases for the crustal contribution at the source and the station before computing the difference in the computed time. By doing this we account for the slight difference in the incident angle of the two phases.

[71] We have expanded on our crustal correction procedure not only because it is a complicated algorithm, but also because it was not quite correctly implemented for *PRI-P04*, which has caused some differences between *PRI-P04* and *PRI-P05*, understandably mostly at shallow depth but occasionally in ill-resolved areas of the model. Figures A1 and A2 show a comparison of *PRI-P04* [*Montelli et al.*, 2004a], with two new *P*-wave models. *PRI-P05*, the model discussed in this paper, was obtained by inverting only for the correction with respect to *PRI-P04*, using (3) and adjusted error estimates. For comparison, we also inverted the data from scratch to obtain *PRI-P05a*. The difference between the two models is caused by the difference in regularization: we damp toward *PRI-P04* and toward zero, respectively. Both *PRI-P05* models fit the data equally well with reduced $\chi^2 = 1$ for each frequency band. A comparison among the three models gives a good impression both of the influence of the crustal corrections and of the choice of regularization. Visually we can see that there is not a significant difference between the three models. Differences are mainly in the details of upper-mantle anomalies (Figure A1). Etna does not cap a plume in the corrected *P*-wave model. The most significant change in the lower mantle is found for Hawaii, which is now clearly visible all the way to the core-mantle-boundary (Figure A2).

Appendix B: Comparison of *PRI-S05* and Other *S*-Wave Tomographic Models in the Spherical Harmonic Domain

[72] To analyze the correlation as a function of scale we decomposed the velocity maps in Figures 4–7 in spherical harmonics [*Dahlen and Tromp*, 1998, sections B.4 and B.8]. The correlation coefficient between velocity maps and the spectral power of the velocity perturbations are plotted versus the spherical harmonic degree l in Figures B1 and B2; to explore a possible difference between positive and negative anomalies, we show correlations and power spectra for the positive anomalies only in Figures B3 and B4, and for the negative anomalies only in Figures B5 and B6. Maps are truncated at the respective harmonic degree expansions: *S362D1*, $l = 18$; *S20RTS*, $l = 20$; and *SAW24B16*, $l = 24$. Models *SB4L18* is originally parameterized by a 4° × 4° grid, *S&G* by a 1° × 1° degree so we investigate these up to degree $l = 30$. Numbers 1 to 8 in the maps correspond to the depth layers in Figures 4–7,

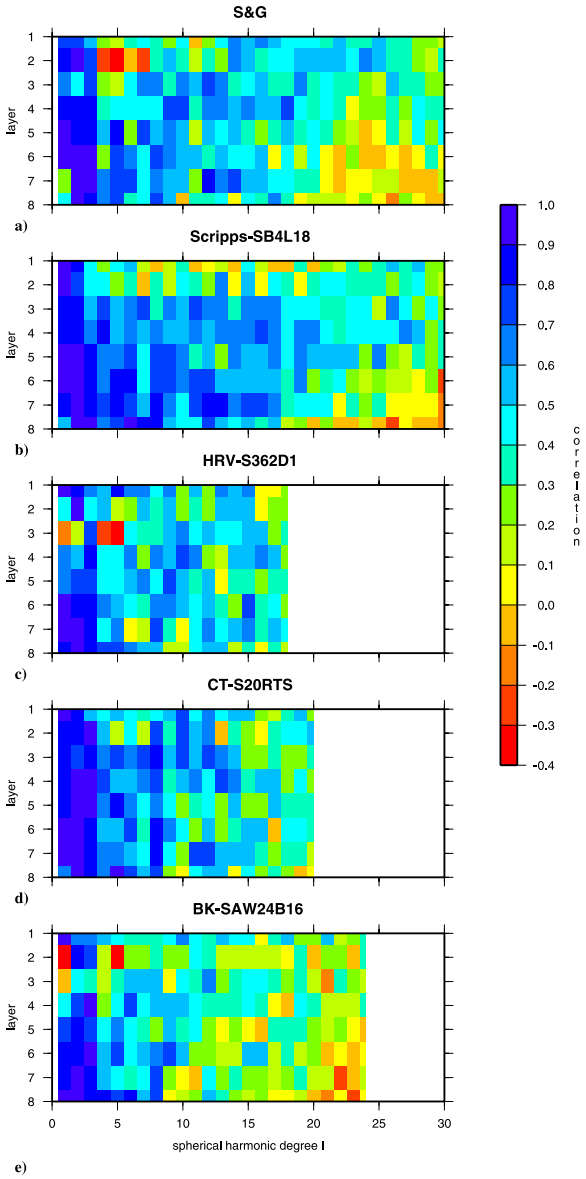

Figure B1. Correlation coefficient of each model with respect to *PRI-S05* model decomposed in spherical harmonics.

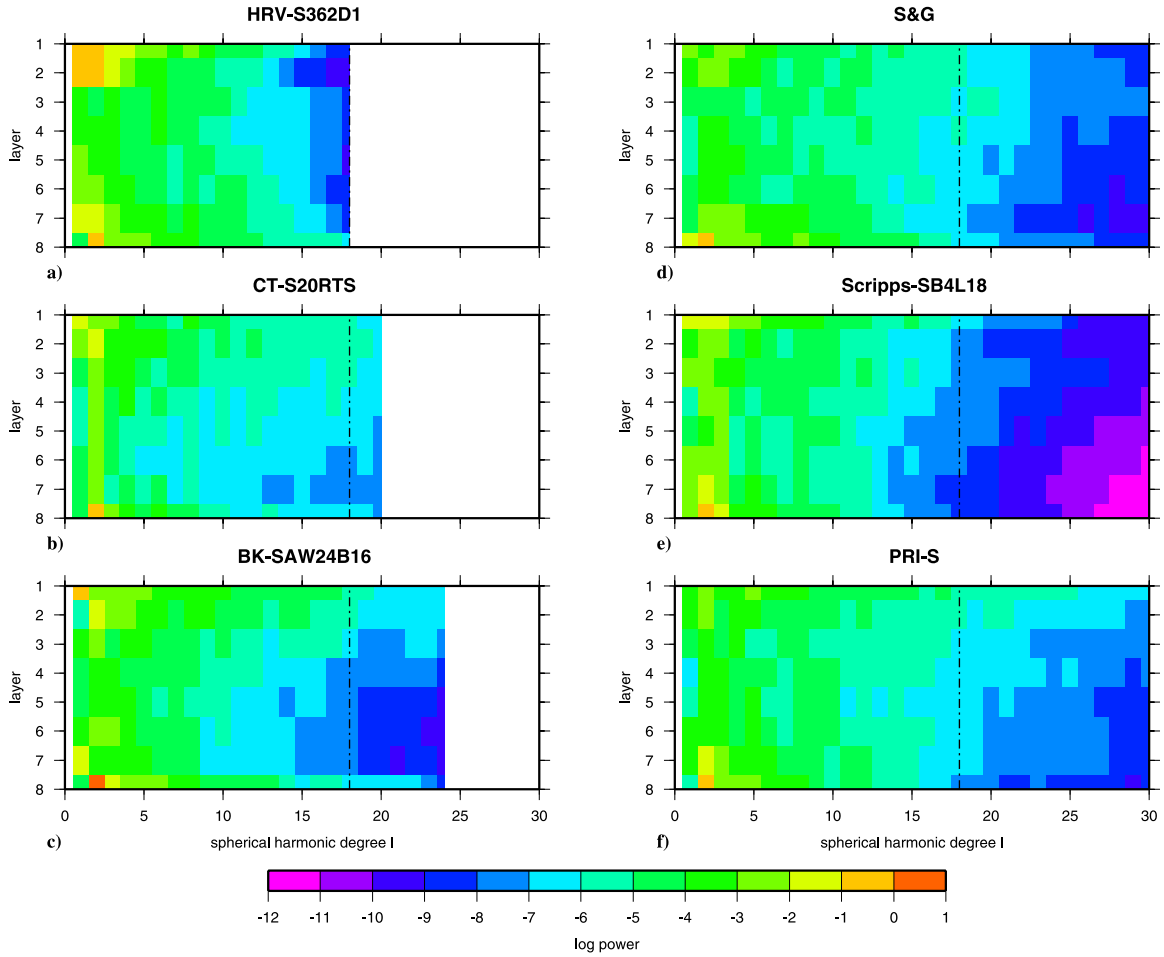

Figure B2. Power spectrum of each of the shear-wave velocity models used in the comparison described in the text.

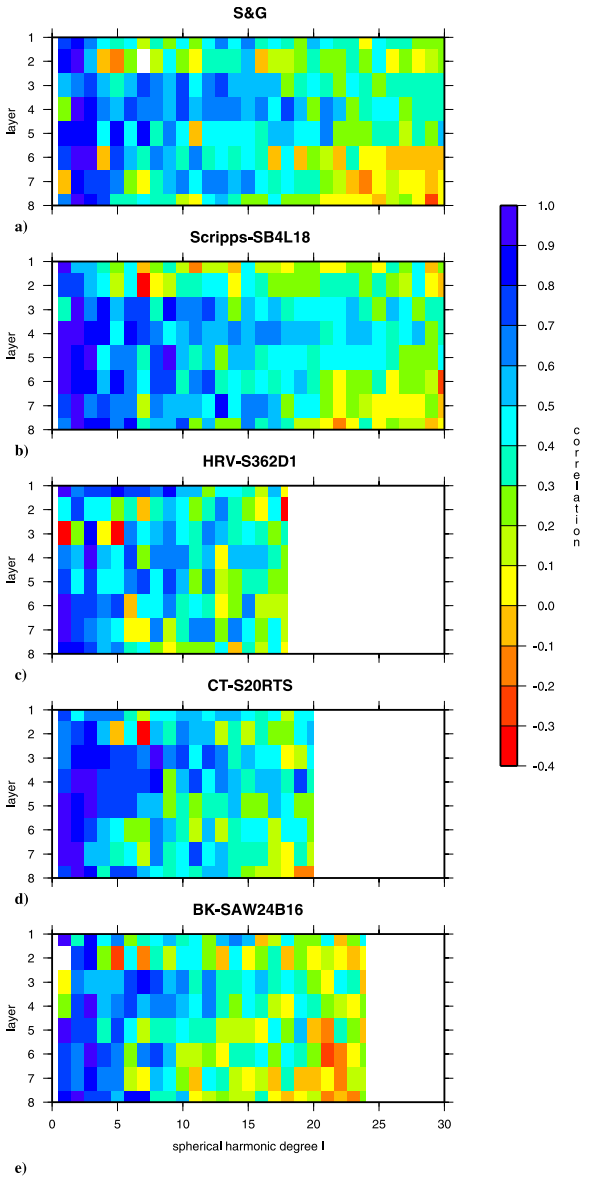

Figure B3. Correlation coefficient of only the positive anomalies of each model with respect to *PRI-S05* model decomposed in spherical harmonics.

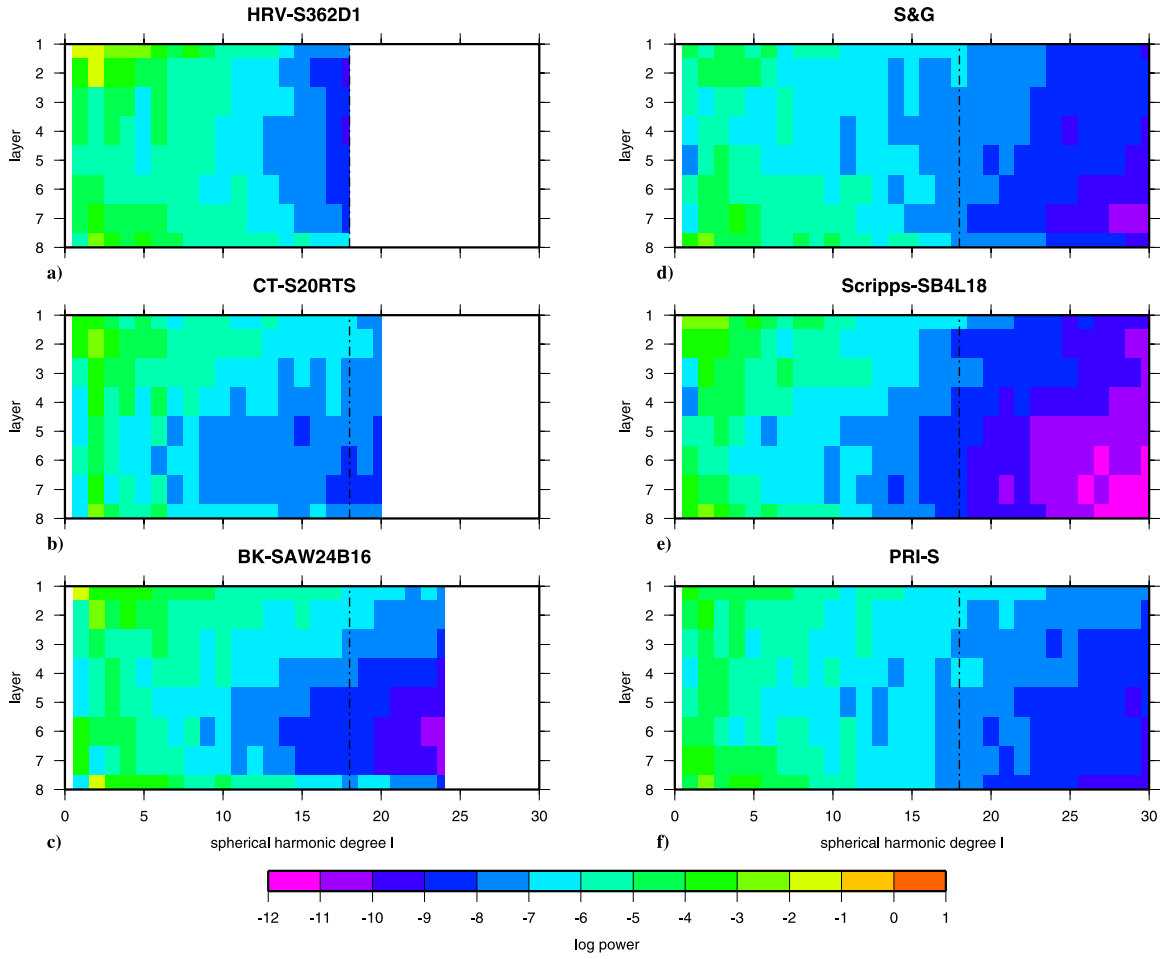

Figure B4. Power spectrum of only the positive anomalies of each of the shear-wave velocity models used in the comparison described in the text.

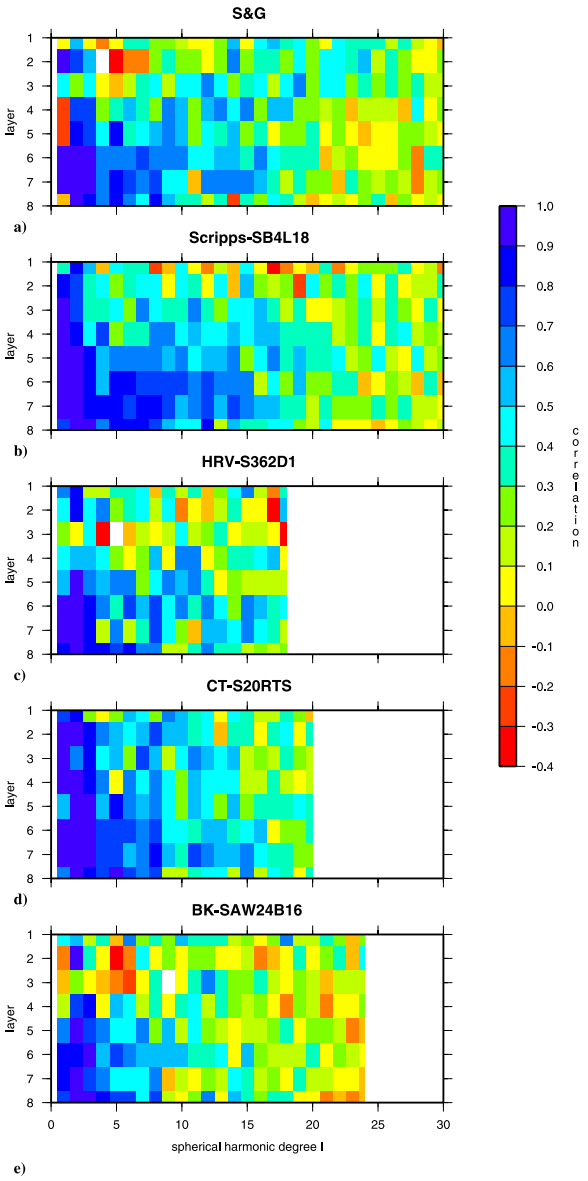

Figure B5. Correlation coefficient of only the negative anomalies of each model with respect to *PRI-S05* model decomposed in spherical harmonics.

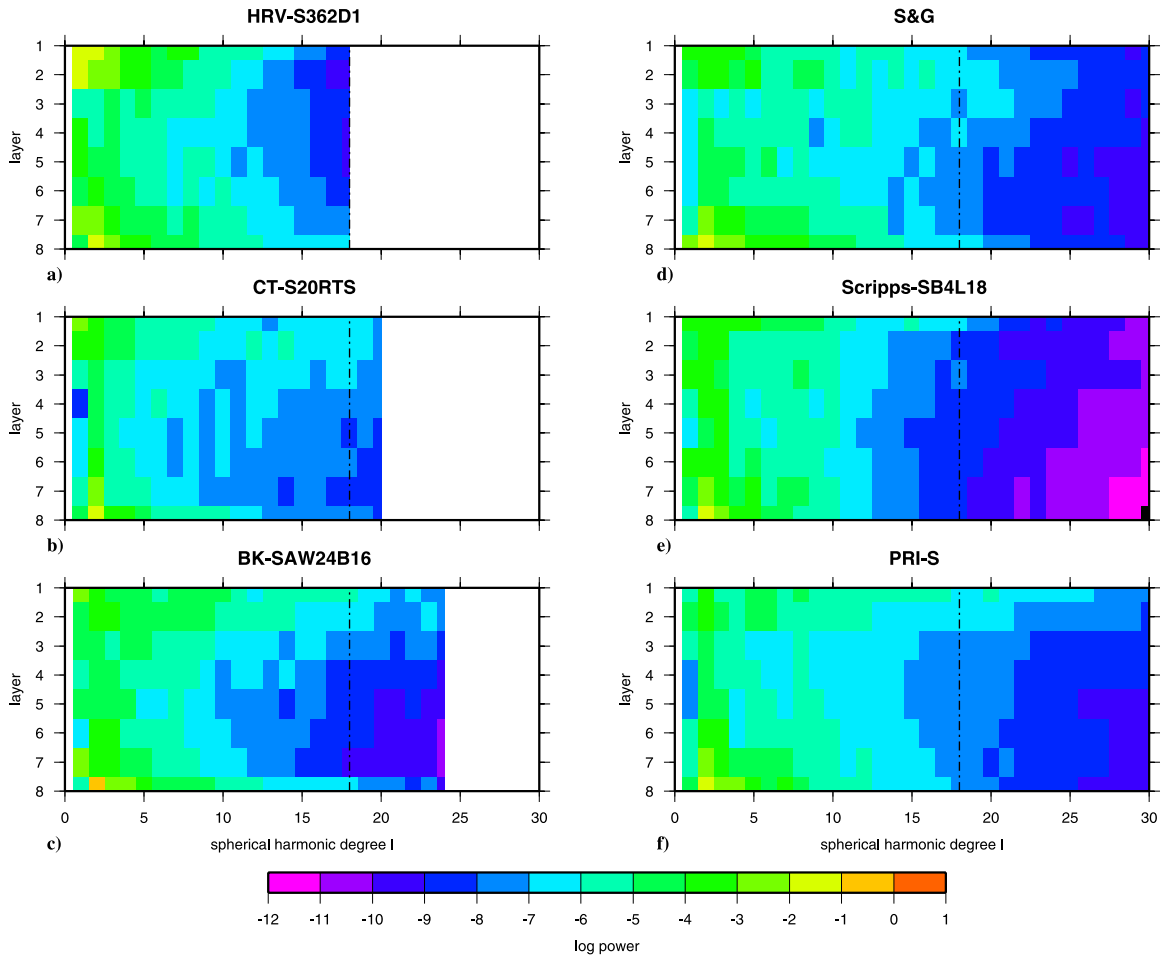

Figure B6. Power spectrum of only the negative anomalies of each of the shear-wave velocity models used in the comparison described in the text.

where 1 corresponds to 350 km and 8 to 2800 km depth, respectively.

[73] The correlation plots confirm that the correlation is highest with respect to model *SB4L18*. With the exception of the shallow layers (1 and 2) where models do not correlate very well, at deeper levels the correlation is above 0.7, even for structures with $l > 10$. When looking at the positive and negative anomaly perturbations separately, *SB4L18* and *PRI-S05* correlate well in the lower mantle up to degree 30, whereas for the slow anomalies the correlation decreases above degree 15. Correlation is also reasonably good with respect to *S20RTS* and, with the exception of the upper mantle, with *S&G*, particularly for the slow anomalies. Correlation is overall poor with respect to *S362D1* and *SAW24B16*, with the higher correlation confined to the lower mantle and to the small orders ($l < 10$). The power spectrum plots (Figure B2) show that models *PRI-S05*, *SB4L18* and *S&G* are dominated by stronger velocity anomalies for small-scale structures with $l > 15$; Figures B4 and B6 show that this is true for both positive and negative anomalies.

Acknowledgments

[74] We thank Rob Van der Hilst for his critical analysis of *PRI-P04* at shallow depth, which led us to discover and remedy a problem with the crustal corrections. We are also indebted to Anne Davaille for her very helpful extensive review of an earlier version of this paper and to Cinzia Farnetani, Vincent Courtillot, Jeroen Ritsema, Norm Sleep, and Bob Smith for their helpful comments and for the many productive discussions. This research was made possible through financial support from the National Science Foundation under grants EAR-0309298 and EAR-0105387.

References

Allen, R. M., et al. (2002), Imaging the mantle beneath Iceland using integrated seismological techniques, *J. Geophys. Res.*, *107*(B12), 2325, doi:10.1029/2001JB000595.

Anderson, D. L. (2000), The thermal state of the upper mantle: No role for mantle plumes, *Geophys. Res. Lett.*, *27*, 3623–3626.

Bastow, I. D., G. W. Stuart, J.-M. Kendall, and C. J. Ebinger (2005), Upper-mantle seismic structure in a region of incipient continental breakup: Northern Ethiopian rift, *Geophys. J. Int.*, *162*, 479–493.

Behrendt, J. C., D. D. Blankenship, C. A. Finn, R. E. Bell, R. E. Sweeney, S. M. Hodge, and J. M. Brozena (1994), CASERTZ aeromagnetic data reveal late Cenozoic flood basalts in the west Antarctic rift system, *Geology*, *22*, 527–530.

Benoit, M. H., A. A. Nyblade, J. C. VanDecar, and H. Gurrola (2003), Upper mantle P wave velocity structure and transition zone thickness beneath the Arabian Shield, *Geophys. Res. Lett.*, *30*(10), 1531, doi:10.1029/2002GL016436.

Benoit, M. H., A. A. Nyblade, and J. C. VanDecar (2006), Upper mantle P wave speed variations beneath Ethiopia and the origin of the Afar Hotspot, *Geology*, *34*, 329–332.

Bijwaard, H., and W. Spakman (1999), Tomographic evidence for a narrow whole mantle plume below Iceland, *Earth Planet. Sci. Lett.*, *166*, 121–126.

Bijwaard, H., and W. Spakman (2000), Non-linear global *P*-wave tomography by iterated linearized inversion, *Geophys. J. Int.*, *141*, 71–82.

Bolton, H., and G. Masters (2001), Travel times of P and S from global digital seismic networks: Implication for the relative variation of P and S velocity in the mantle, *J. Geophys. Res.*, *106*, 13,527–13,540.

Bunge, H.-P., M. A. Richards, and J. R. Baumgardner (1997), A sensitivity study of the three-dimensional spherical mantle convection at 10^8 Rayleigh number: Effects of depth-dependent viscosity, heating mode, and an endothermic phase change, *J. Geophys. Res.*, *102*, 11,991–12,007.

Campbell, I. H., and R. W. Griffiths (1990), Implications of mantle plumes structure for the evolution of flood basalts, *Earth Planet. Sci. Lett.*, *99*, 79–93.

Christensen, U. (1998), Fixed hotspots gone with the wind, *Nature*, *391*, 739–740.

Clocchiatti, R., M. Condomines, N. Guénot, and J.-C. Tanguy (2004), Magma changes at Mount Etna: The 2001 and 2002–2003 eruptions, *Earth Planet. Sci. Lett.*, *227*, 397–414.

Courtillot, V., A. Davaille, J. Besse, and J. Stock (2003), Three distinct types of hotspots in the Earth's mantle, *Earth Planet. Sci. Lett.*, *205*, 295–308.

Cserepes, L., and D. A. Yuen (2000), On the possibility of a second kind of mantle plume, *Earth Planet. Sci. Lett.*, *183*, 61–71.

Dahlen, F. A., and J. Tromp (1998), *Theoretical Global Seismology*, 1025 pp., Princeton Univ. Press, Princeton, N. J.

Dahlen, F. A., S.-H. Hung, and G. Nolet (2000), Fréchet kernels for finite-frequency traveltimes — I. Theory, *Geophys. J. Int.*, *141*, 157–174.

Daradich, A., J. X. Mitrovica, R. N. Pysklywec, S. D. Willett, and A. M. Forte (2003), Mantle flow, dynamic topography, and rift-flank uplift of Arabia, *Geology*, *31*, 901–904.

Davaille, A. (1999), Simultaneous generation of hot spots and superswells by convection in a heterogeneous planetary mantle, *Nature*, *402*, 756–760.

Davaille, A., M. L. Bars, and C. Carbonne (2003), Thermal convection in a heterogeneous mantle, *C. R. Geosci.*, *355*, 141–156.

Debayle, E., J.-J. Lévêque, and M. Cara (2001), Seismic evidence for a deeply rooted low-velocity anomaly in the upper mantle beneath the northeastern Afro/Arabian continent, *Earth Planet. Sci. Lett.*, *193*, 423–436.

Doucelance, R., S. Escrig, M. Moreira, C. Gariepy, and M. D. Kurz (2003), Pb-Sr-He isotope and trace element geochemistry of the Cape Verde Archipelago, *Geochim. Cosmochim. Acta*, *67*, 3717–3733.

Engdahl, E., R. van der Hilst, and R. Buland (1998), Global teleseismic earthquake relocation with improved travel times and procedures for depth determination, *Bull. Seismol. Soc. Am.*, *88*, 722–743.

Farnetani, C. G. (1997), Excess temperature of mantle plumes: The role of chemical stratification across D″, *Geophys. Res. Lett.*, *24*, 1583–1586.

Farnetani, C. G., and H. Samuel (2005), Beyond the thermal plume paradigm, *Geophys. Res. Lett.*, *32*, L07311, doi:10.1029/2005GL022360.

Foulger, G. R. (2003), Plumes, or plate tectonic processes?, *Astron. Geophys.*, *43*, 6.19–6.23.
Foulger, G. R., et al. (2001), Seismic tomography shows that upwelling beneath Iceland is confined to the upper mantle, *Geophys. J. Int.*, *146*, 504–530.
Goes, S., W. Spakman, and H. Bijwaard (1999), A lower mantle source for central European volcanism, *Science*, *286*, 1928–1931.
Grand, S. P. (2002), Mantle shear-wave tomography and the fate of subducted slabs, *Philos. Trans. R. Soc. London, Ser. A*, *360*, 2475–2491.
Grand, S. P., R. D. Van der Hilst, and S. Widiyantoro (1997), Global seismic tomography: A snapshot of convection in the Earth, *GSA Today*, *7*, 1–3.
Griffiths, R. W. (1986), Thermals in extremely viscous fluids, including the effects of temperature-dependent viscosity, *J. Fluid Mech.*, *186*, 115–138.
Griffiths, R. W., and I. H. Campbell (1990), Stirring and structure in mantle starting plumes, *Earth Planet. Sci. Lett.*, *99*, 66–78.
Gu, Y. J., A. M. Dziewonski, W. Su, and G. Ekström (2001), Models of the mantle shear velocity and discontinuities in the pattern of lateral heterogeneities, *J. Geophys. Res.*, *106*, 11,169–11,199.
Gudmundsson, O., J. Davies, and R. Clayton (1990), Stochastic analysis of global travel time data: Mantle heterogeneity and random errors in the ISC data, *Geophys. J. Int.*, *102*, 25–44.
Gvirtzman, Z., and A. Nur (1999), The formation of Mount Etna as the consequence of slab rollback, *Nature*, *401*, 782–785.
Helmberger, D. V., L. Wen, and X. Ding (1998), Seismic evidence that the source of the Iceland hotspot lies at the core-mantle boundary, *Nature*, *396*, 251–255.
Humphreys, E. D., K. G. Dueker, D. L. Schutt, and R. B. Smith (2000), Beneath Yellowstone: Evaluating plume and nonplume models using teleseismic images of the upper mantle, *GSA Today*, *10*, 1–7.
Hung, S.-H., Y. Shen, and L.-Y. Chiao (2004), Imaging seismic velocity structure beneath the Iceland hot spot: A finite frequency approach, *J. Geophys. Res.*, *109*, B08305, doi:10.1029/2003JB002889.
Ishii, M., and J. Tromp (2004), Constraining large-scale mantle heterogeneity using mantle and inner-core sensitive normal modes, *Phys. Earth Planet. Inter.*, *146*, 113–124.
Ito, G. (2001), Reykjanes 'V'-shaped ridges originating from a pulsating and dehydrating mantle plume, *Nature*, *411*, 681–684.
Jellinek, A., and M. Manga (2002), The influence of a chemical boundary layer on the fixity and lifetime of mantle plumes, *Nature*, *418*, 760–763.
Jolivet, L., and C. Faccenna (2000), Mediterranean extension and the Africa-Eurasia collision, *Tectonics*, *19*(6), 1095–1106.
Karato, S.-I. (1993), Importance of anelasticity in the interpretation of seismic tomography, *Geophys. Res. Lett.*, *20*, 1623–1626.
Kellogg, L. H., and S. D. King (1997), The effect of temperature dependent viscosity on the structure of new plumes in the mantle: Results of a finite element model in a spherical, axisymmetric shell, *Earth Planet. Sci. Lett.*, *148*, 13–26.
Kennett, B. L. N., and E. R. Engdahl (1991), Traveltimes for global earthquake location and phase identification, *Geophys. J. Int.*, *105*, 429–465.
King, S. D., and D. L. Anderson (1995), An alternative mechanism of flood basalt formation, *Earth Planet. Sci. Lett.*, *136*, 269–279.
Knox, R. P., A. A. Nyblade, and C. A. Langston (1998), Upper mantle S velocities beneath Afar and western Saudi Arabia from Rayleigh wave dispersion, *Geophys. Res. Lett.*, *25*, 4233–4236.
Korenaga, J. (2005), First mantle plumes and the nature of the core-mantle boundary region, *Earth Planet. Sci. Lett.*, *232*, 29–37.
Lebedev, S. (2000), The upper mantle beneath the western Pacific and southern Asia, Ph.D. thesis, Princeton Univ., Princeton, N. J.
Li, X., R. Kind, and X. Yuan (2001), Upper mantle structure and transition zone thickness beneath ocean islands from receiver function study, *Eos Trans. AGU*, *82*(47), Fall Meet. Suppl., Abstract S42B-0633.
Marone, F., S. van der Lee, and D. Giardini (2004), Three-dimensional upper-mantle S-velocity model for the Eurasia-Africa plate boundary region, *Geophys. J. Int.*, *158*, 109–130.
Masters, G., G. Laske, H. Bolton, and A. Dziewonski (2000), The relative behavior of shear velocity, bulk sound speed, and compressional velocity in the mantle: Implications for chemical and thermal structure, in *Earth's Deep Interior*: *Mineral Physics and Tomography From the Atomic to the Global Scale*, *Geophys. Monogr. Ser.*, vol. 117, edited by S. Karato et al., pp. 63–87, AGU, Washington, D. C.
Mégnin, C., and B. Romanowicz (2000), The three-dimensional shear velocity structure of the mantle from the inversion of body, surface and higher-mode waveforms, *Geophys. J. Int.*, *143*, 709–728.
Montelli, R., G. Nolet, F. A. Dahlen, G. Masters, E. R. Engdahl, and S.-H. Hung (2004a), Finite-frequency tomography reveals a variety of plumes in the mantle, *Science*, *303*, 338–343.
Montelli, R., G. Nolet, G. Masters, F. A. Dahlen, and S.-H. Hung (2004b), Global P and PP traveltime tomography: Rays versus waves, *Geophys. J. Int.*, *158*, 637–654.
Montelli, R., G. Nolet, F. A. Dahlen, and G. Masters (2006), Comment on 'banana-doughnut kernels and mantle tomography' by van der Hilst and de hoop, *Geophys. J. Int.*, in press.
Morelli, A., and A. M. Dziewonski (1987), Topography of the core-mantle boundary and lateral homogeneity of the liquid core, *Nature*, *325*, 678–683.
Morgan, W. J. (1971), Convection plumes in the lower mantle, *Nature*, *230*, 42–43.
Nataf, H.-C., and J. VanDecar (1993), Seismological detection of a mantle plume?, *Nature*, *364*, 115–120.
Nolet, G., R. Allen, and D. Zhao (2006a), Mantle plume tomography, *Chem. Geol.*, in press.
Nolet, G., S.-I. Karato, and R. Montelli (2006b), Plume fluxes from seismic tomography, *Earth Planet. Sci. Lett.*, *248*, 685–699.
Nyblade, A. A., R. P. Knox, and H. Gurrola (2000a), Mantle transition zone thickness beneath Afar: Implications for the origin of the Afar hotspot, *Geophys. J. Int.*, *142*, 615–619.
Nyblade, A. A., T. J. Owens, H. Gurrola, J. Ritsema, and C. A. Langston (2000b), Seismic evidence for a deep upper mantle thermal anomaly beneath east Africa, *Geology*, *28*, 599–602.
O'Connor, J. M., P. Stoffers, J. R. Wijbrans, P. M. Shannon, and T. Morrissey (2000), Evidence from episodic seamount volcanism for pulsing of the Iceland plume in the past 70 Myr, *Nature*, *408*, 954–958.
Olson, P. (1990), Hot spots, swells and mantle plumes, in *Magma Transport and Storage*, edited by M. P. Ryan, pp. 33–54, John Wiley, Hoboken, N. J.
Olson, P., and H. Singer (1985), Creeping plumes, *J. Fluid Mech.*, *158*, 511–531.

O'Neill, C., D. Mller, and B. Steinberger (2005), On the uncertainties in hot spot reconstructions and the significance of moving hot spot reference frames, *Geochem. Geophys. Geosyst.*, *6*, Q04003, doi:10.1029/2004GC000784.

Pilidou, S., K. Priestley, E. Debayle, and O. Gudmundsson (2005), Rayleigh wave tomography in the North Atlantic: High-resolution images of the Iceland, Azores and Eifel mantle plumes, *Lithos*, *79*, 453–474.

Rhodes, M., and J. H. Davies (2001), Tomographic images of multiple mantle plumes in the uppermost lower mantle, *Geophys. J. Int.*, *147*, 88–92.

Ritsema, J., and H. J. van Heijst (2000), Seismic imaging of structural heterogeneity in Earth's mantle: Evidence for large-scale mantle flow, *Sci. Prog.*, *83*, 243–259.

Ritsema, J., H. J. Van Heijst, and J. H. Woodhouse (1999), Complex shear wave velocity structure imaged beneath Africa and Iceland, *Science*, *286*, 1925–1928.

Ritter, J. R. R., M. Jordan, U. R. Christensen, and U. Achauer (2001), A mantle plume below the Eifel volcanic fields, Germany, *Earth Planet. Sci. Lett.*, *186*, 7–14.

Rocchi, S., P. Armienti, and G. D. Vincenzo (2005), No plume, no rift magmatism in the West Antartic rift, in *Plate, Plumes and Paradigms*, edited by G. R. Foulger et al., pp. 435–447, Geol. Soc. of Am., Boulder, Colo.

Saltzer, R., and E. Humphreys (1997), Upper mantle P wave velocity structure of the eastern Snake River Plain and its relationship to geodynamic models of the region, *J. Geophys. Res.*, *102*, 11,829–11,842.

Schefer, B. F., S. Turner, I. Parkinson, N. Rogers, and C. Hawkensworth (2002), Evidence for recycled Archaean oceanic mantle lithosphere in the Azores plume, *Nature*, *420*, 304–307.

Schiano, P., R. Clocchiatti, L. Ottolini, and T. Busà (2001), Transation of Mount Etna lavas from a mantle-plume to an island-arc magmatic source, *Nature*, *412*, 900–904.

Segev, A. (2002), Flood basalts, continental breakup and the dispersal of Gondwana: Evidence for periodic migration of upwelling mantle flows (plumes), in *From Continental Extension to Collision: Africa-Europe Interaction, the Dead Sea and Analogue Natural Laboratories*, *EGU Stephan Mueller Spec. Publ. Ser.*, vol. 2, pp. 171–191, Eur. Geophys. Union, Strasbourg, France.

Shen, Y., S. Solomon, I. T. Bjarnason, and G. M. Purdy (1996), Hot mantle transition zone beneath Iceland and the adjacent Mid-Atlantic Ridge inferred from P-to-S conversions at the 410- and 660-km discontinuities, *Geophys. Res. Lett.*, *23*, 3527–3530.

Shen, Y., S. Solomon, I. T. Bjarnason, and C. J. Wolfe (1998), Seismic evidence for a lower-mantle origin of the Iceland plume, *Nature*, *395*, 62–65.

Silveira, G., and E. Stutzmann (2002), Anisotropic tomography of the Atlantic Ocean, *Phys. Earth Planet. Inter.*, *132*, 237–248.

Silveira, G., E. Stutzmann, A. Davaille, J.-P. Montagner, and L. Mendes-Victor (2006), Azores hotspot signature in the upper mantle, *J. Volcanol. Geotherm. Res.*, *156*, 23–34.

Simmons, N. A., A. M. Forte, and S. P. Grand (2006), Constraining mantle flow with seismic and geodynamic data: a joint approach, *Earth Planet. Sci. Lett.*, *246*, 109–124.

Sleep, N. H. (1990), Hotspots and mantle plumes: Some phenomenology, *J. Geophys. Res.*, *95*, 6715–6736.

Sleep, N. H. (2002), Ridge-crossing mantle plumes and gaps in tracks, *Geochem. Geophys. Geosyst.*, *3*(12), 8505, doi:10.1029/2001GC000290.

Steinberger, B., and R. J. O'Connell (1998), Advection of plumes in mantle flow: Implications for hotspot motion, mantle viscosity and plume distribution, *Geophys. J. Int.*, *132*, 412–434.

Storey, B. C., P. T. Leat, S. D. Weaver, R. J. Pankhurst, J. D. Bradshaw, and S. Kelley (1999), Mantle plumes and Antarctica — New Zealand rifting: Evidence from mid-Cretaceous mafic dykes, *J. Geol. Soc. London*, *156*, 659–671.

Tanguy, J.-C., M. Condomines, and G. Kieffer (1997), Evolution of the Mount Etna magma: Constraints on the present feeding system and eruptive mechanism, *J. Volcanol. Geotherm. Res.*, *75*, 221–250.

Thomson, P. F., and P. J. Tackley (1998), Generation of megaplumes from the core-mantle boundary in a compressible mantle with temperature-dependent viscosity, *Geophys. Res. Lett.*, *25*, 1999–2002.

Todal, A., and O. Edholm (1998), Continental margin off Western India and Deccan Large Igneous Province, *Mar. Geophys. Res.*, *20*, 273–291.

van der Hilst, R., and H. Kárason (1999), Compositional heterogeneity in the bottom 1000 km of the Earth's mantle: Toward a hybrid convection model, *Science*, *283*, 1885–1888.

van der Voo, R., W. Spakman, and H. Bijwaard (1999), Mesozoic subducted slabs under Siberia, *Nature*, *397*, 246–249.

Waite, G. P. (2004), Upper mantle structure of the Yellowstone hotspot from teleseismic body-wave velocity tomography and shear-wave anisotropy, Ph.D. thesis, Univ. of Utah, Salt Lake City.

Waite, G. P., R. B. Smith, and R. M. Allen (2006), V_P and V_S structure of the Yellowstone hot spot from teleseismic tomography: Evidence for an upper mantle plume, *J. Geophys. Res.*, *111*, B04303, doi:10.1029/2005JB003867.

Weeraratne, D. S., D. W. Forsyth, K. M. Fischer, and A. A. Nyblade (2003), Evidence for an upper mantle plume beneath the Tanzanian craton from Rayleigh wave tomography, *J. Geophys. Res.*, *108*(B9), 2427, doi:10.1029/2002JB002273.

White, N., and B. Lovell (1997), Measuring the pulse of a plume with the sedimentary record, *Nature*, *387*, 888–891.

Whitehead, J. A., and D. S. Luther (1975), Dynamics of laboratory diapir and plume models, *J. Geophys. Res.*, *80*, 705–717.

Wolfe, C. J., I. T. Bjarnason, J. C. VanDecar, and S. C. Solomon (1997), Seismic structure of the Iceland mantle plume, *Nature*, *385*, 245–247.

Zhao, D. (2001), Seismic structure and origin of hotspots and mantle plumes, *Earth Planet. Sci. Lett.*, *192*, 251–265.

Zhao, D. (2004), Global tomographic images of mantle plumes and subducting slabs: Insight into deep Earth dynamics, *Earth Planet. Sci. Lett.*, *146*, 3–34.

Zhong, S. (2005), Dynamics of thermal plumes in three-dimensional isoviscous thermal convection, *Geophys. J. Int.*, *162*, 289–300.

Zhong, S. (2006), Constraints on thermochemical convection of the mantle from plume heat flux, plume excess temperature, and upper mantle temperature, *J. Geophys. Res.*, *111*, B04409, doi:10.1029/2005JB003972.

Zhong, S., M. T. Zuber, L. Moresi, and M. Gurnis (2000), Role of temperature-dependent viscosity and surface plates in spherical shell models of mantle convection, *J. Geophys. Res.*, *105*, 11,063–11,082.